Texture Evolution in Cold Rolled Low Carbon Steel Sheet and the Development of Some Corresponding Anisotropic Yield Functions

TEXTURE EVOLUTION IN COLD ROLLED LOW CARBON STEEL SHEET AND THE DEVELOPMENT OF SOME CORRESPONDING ANISOTROPIC YIELD FUNCTIONS

BY

DAVY CHI KEUNG TSOI, B. ENG.

A Thesis

Submitted to the School of Graduate Studies

in Partial Fulfilment of the Requirements

for the Degree of Master of Engineering

McMaster University

MASTER OF ENGINEERING (2001) McMASTER UNIVERSITY
(Mechanical Engineering) Hamilton, Ontario

TITLE: Texture Evolution in Cold Rolled Low Carbon Steel and the Development of Some Corresponding Anisotropic Yield Functions.

AUTHOR: Davy Chi Keung Tsoi, B. Eng.

(McMaster University, Hamilton, Ontario)

SUPERVISOR: Professor R. Sowerby

NUMBER OF PAGES: xv, 154

Abstract

One of the goals of this thesis was to establish how the texture i.e. the preferred orientation of the grains, evolved during the cold rolling of a low carbon steel. The material was reduced in a commercial cold rolling mill, located at the Dofasco steel company in Hamilton. The original intention was to vary the reduction at each roll stand and to alter the front and back tension of the sheet between each stand, to see what effect this would have on the resulting texture. However, this proved to be too ambitious since the company did not want a commercial piece of equipment to be out of service for long periods of time. Consequently only one mill setting was investigated, using a 5-stand, 4-high mill. Nonetheless this provided a rare opportunity to measure mechanical and metallurgical properties after each roll stand – information which is usually not available in the open literature. The mill was stopped during production and samples were cut from the sheet between each roll stand for subsequent analysis.

The texture after each roll stand was revealed by a metallurgical examination through the use of pole figures. The texture that ensued was typical of a cold rolled steel, as observed by previous workers, and did not change much after passing through the first stand. The dominant crystallographic orientation was (100) and (110) planes lying in the plane of the rolled sheet.

Texture measurements were performed at the Los Alamos National Laboratories in New Mexico, who had also developed software to *predict* the texture evolution. However, it was decided to keep the experimental measurements and the theoretical

predictions separate, and researchers at Queen's University agreed to handle the analysis using a software package developed by Van Houtte. As described in the text, the approach invoked the use of Crystallite Orientation Distribution Functions (CODFs) analysis based on the following, *a)* Some measured pole figures for the as-received material only, *b)* an assumed deformation mode in each roll stand, *c)* an assumed crystallographic slip system and *d)* some mechanical property data. It turned out that the measured and predicted pole figures showed very good agreement, and so established the predictive capabilities of the software package for the cold rolling process. In addition to predicting the texture, CODF analysis can predict the corresponding plane stress crystallographic yield loci along with the variation in the normalized yield stress and the r-value at any orientation θ to the rolling direction.

A great deal of time was devoted to establishing a reliable anisotropic yield function that could be used in the modelling of deformation processes. The work due to Barlat and his co-workers seemed very promising, although many of the details required to independently develop these models were not given in the original publications. The necessary algorithms were developed as part of this work. Under normal circumstances various coefficients in the analytical yield function would be determined from mechanical property data e.g. r_0, r_{45}, σ_0, σ_b etc., as explained in the text. In the present study this information was not available and instead theoretical values from the CODF analysis performed at Queen's University were used. These data are referred to in the text as pseudo-experimental.

It turned out that Barlat's yield model can duplicate with good accuracy the crystallographic yield loci predicted at Queen's University, and therefore some confidence can be placed in the predictive capabilities of the model. As a further check on the accuracy of Barlat's model a number of other anisotropic yield functions were compared. Some of these plane stress yield functions could accommodate an applied shear stress while others could not. Barlat's model was the most effective in predicting not only the shape of the crystallographic yield loci, but also the variation in the normalized yield stress and the r-value in the plane of the rolled sheet with the angle θ to the rolling direction.

Results arising from the use of the SEM showed little evidence of macroscopic shear banding which is often observed in heavily cold rolled material. However, coarse slip bands were present and these increased with increasing deformation. The tensile ductility of the material was exhausted i.e. the yield stress and the ultimate stress were the same, after passing through the first stand. As would be expected both the yield stress and the hardness of the material increase with increasing reduction and these values are examined in the text.

Acknowledgements

I wish to express my sincere appreciation to my supervisor Dr. R. Sowerby for his invaluable assistance, guidance, support and consideration throughout the preparation of this thesis. I am also indebted to Dr. J. D. Embury for commenting on the thesis and for arranging the texture work performed at Los Alamos and the metallographic examination, performed at McMaster, to assess the shear banding. Financial support for this work arranged through NSERC is gratefully acknowledged.

Many thanks to the Dofasco steel company for donating the material and to Mr. Ken Shaw who made this donation possible. Special thanks to Dr. F. Barlat (Aluminum Company of America) who spent time with me discussing aspects of his anisotropic yield functions which had not appeared in print. I would also like to thank Dr. R. Zheng (University of Science and Technology, Beijing) for his contribution to the micro-hardness testing. My appreciation also goes to Dr. S. Saimoto and his former graduate student, Jian Li, (Queen's University) for performing the theoretical texture analysis, and to Dr. Carl Necker (Los Alamos National Laboratories) for measuring the experimental texture of the rolled steel sheet.

The assistance of the technicians, Mr. D. Schick, J. Verhaeghe, R. Lodewyks and J. McLaren with some of the experimental work is much appreciated. I am also grateful to, Theresa Castillo, who performed the metallographic examination of the shear banding in the cold rolled structure and prepared the micrographs.

The author would also like to thank his friends, Alice Chan, Gary Lin, Ben Yang, Yang's family, Joe and Sherry, and Steven Choi for their long support and caring. I am in debt to my sisters and brother, for taking care of the family during my absence. Finally I acknowledge with deep gratitude, the encouragement, consideration and financial assistance of my parents.

Table of Contents

	Page
ABSTRACT	iii
ACKNOWLEDGEMENTS	vi
LIST OF FIGURES	xi
LIST OF TABLES	xiv
CHAPTER 1 AN INTRODUCTION	1
1.1 Introduction	1
1.2 Contents	5
CHAPTER 2 LITERATURE REVIEW	6
2.1 Introduction	6
2.2 Miller Indices	6
2.3 Texture Measurement and Analysis	8
2.3.1 Plastic Deformation in Metals: Crystallographic Approach	8
2.3.2 Determination of Pole Figures	10
2.3.3 Crystalline Orientation Distribution Functions(CODFs)	11
2.4 Anisotropic Yield Functions	19
2.4.1 A Brief Review of Non-Quadratic, AnisotropicYield Functions	20
CHAPTER 3 A THEORETICAL AND NUMERICAL ANALYSIS OF BARLAT'S 94 YIELD CRITERION	25
3.1 Introduction	25
3.2 Calculation of the Yield Function	26
3.2.1 The Numerical Method when No Shear Stresses Act	26
3.2.1.1 Determination of the c Coefficients	29
3.2.2 A Numerical Method Appropriate for the Case when Shear Stresses Act	35
3.2.2.1 Evaluating and Plotting the Yield Locus for a Case of Plane Stress	38
3.3 An illustration of how the α Coefficients and the Exponent m can influence the shape of the Yield Locus and the variation in the r-value	40

Page

CHAPTER 4 EXPERIMENTS AND RESULTS 49

4.1 Material 49
4.2 Tensile Tests 50
4.3 r-value Tests 56
4.4 Microhardness Tests 56
4.5 A Preliminary Study of Inhomogeneous Deformation during Cold Rolling 58

CHAPTER 5 COMPARISON OF POLE FIGURES AND THEIR CORRESPONDING YIELD LOCI 70

5.1 Introduction 70
5.2 Texture Measurement for and A Comparison of Pole Figures 72
5.2.1 Introduction 72
5.2.2 Texture Measurement and the Resulting Pole Figure 72
5.2.2.1 Textures Measured at Los Alamos 72
5.2.2.2 Texture (Pole Figure) Simulation Performed at Queen's University 74
5.2.2.3 Comparison of Pole Figures 77
5.3 A Comparison of the Selected Yield Loci 80
5.3.1 Introduction 80
5.3.2 A Comparison of the Selected Yield Loci 80

CHAPTER 6 A COMPARISON OF SOME ANALYTICAL YIELD CRITERIA 85

6.1 Introduction 85
6.2 A Comparison of Some Analytical Yield Criteria 86
6.2.1 Yield Strengths and r-values 90
6.2.1.1 Yield Criteria without a Shear Stress Term 90
6.2.1.2 Yield Criteria with a Shear Stress Term 91
6.2.2 Exponent m 92
6.2.3 Material Coefficients 97
6.3 Comparison of Normalized Yield Loci 99
6.3.1 Yield Criteria without a Shear Stress Term 99
6.3.2 Yield Criteria with a Shear Stress Term 99
6.4 Variation in the Normalized Yield Stress and r-value with Orientation 100
6.4.1 Results of the Variation in the Yield Stress and r-value with Orientation 100

CHAPTER 7 CONCLUSIONS AND RECOMMENDATIONS 115

		Page
APPENDIX A	Plotting a Plane Stress Yield Locus with and without the Presence of the Shear Stress σ_{xy}	119
APPENDIX B	Confirmation of the Value $(\sigma_{xy})_Y$	125
APPENDIX C	A General Program Written in MATLAB for Evaluating Barlat's 94 Yield Criterion	128
APPENDIX D	A Program Written in MATLAB for Plotting the Contours of the Yield Loci,with the Presence of a Shear Stress Term	136
APPENDIX E	A Program Written in MATLAB for Plotting the Contours of the Yield Loci, without the Presence of a Shear Stress Term	141
APPENDIX F	A Program Written in MATLAB for Evaluating the Yield Stress and r-value at Any Orientation to the Rolling Direction	143
REFERENCES		148

List of Figures

		Page
Figure 2.1	Slip under a Uniaxial Tension F	8
Figure 2.2	Process of Pole Figure Creation	12
Figure 2.3	A (200) Pole Figure for Rolled Molybdenum	13
Figure 2.4	Sequential Rotation of Roe's Notation	13
Figure 2.5	The Representation of CODF of A Recrystallized Iron	15
Figure 2.6	Sectional View of CODF for A Cold Rolled Copper after 95% Reduction	15
Figure 2.7	A Comparison of Normalized Planar Yield Surfaces from Experiments, TBH Polycrystal, Barlat's 91 and 94 Yield Criteria	17
Figure 3.1	A Flow Chart of Yield Criterion with and without Shear Stress $(\sigma_{xy})_Y$	32
Figure 3.2	A General Point on the Normalized Yield Locus	33
Figure 3.3	A General Plane Stress State on the Normalized Yield Locus	39
Figure 3.4	A Projection of the Shear Contours in a 2-D View	41
Figure 3.5	A Projection of the Shear Contours in a 3-D View	41
Figure 3.6	Influence of α_z on the Shape of the Yield Locus	42
Figure 3.7	Influence of α_x, α_y and α_z on the Shape of the Yield Locus	42
Figure 3.8	Influence of m on the Shape of the Yield Locus	43
Figure 3.9	Influence of α_x on the Variation in the r-value	43
Figure 3.10	Influence of α_y on the Variation in the r-value	44
Figure 3.11	Influence of α_z on the Variation in the r-value	44

		Page
Figure 4.1	An ASTM Standard E10 Strip Tensile Specimen	51
Figure 4.2	The True Stress-Strain Curve for the Material at Entry	52
Figure 4.3	The True Stress-Strain Curve for the Stage One Sample	52
Figure 4.4	The True Stress-Strain Curve for the Stage Two Sample	53
Figure 4.5	The True Stress-Strain Curve for the Stage Three Sample	53
Figure 4.6	The True Stress-Strain Curve for the Stage Four Sample	54
Figure 4.7	The True Stress-Strain Curve for the Material at Exit	54
Figure 4.8	Experimental and Predicted True Stress-Strain Curve	55
Figure 4.9	A Mounted Specimen for Microhardness Tests	58
Figure 4.10	The Stage Five Sample after Indentation	59
Figure 4.11	The Hardness-Distance from Surface Curves for All Stages	61
Figure 4.12	Average Hardness in Each Stage	62
Figure 4.13	The Experimental and Empirical Hardness-Thickness Curves	62
Figure 4.14	The Microstructures of the Cold Rolled Steel at Different Temperatures	63
Figure 4.15	The Hardness-Temperature Curve for the Cold Rolled Steel	64
Figure 4.16	Shear Bands during Rolling	64
Figure 4.17	Coarse Slip Bands (CSB) and Macroscopic Slip Band	66
Figure 4.18	The Stage Zero Sample with the Equi-cored Grains in the Longitudinal Plane	66
Figure 4.19	An Al_2O_3 Inclusion in the Longitudinal Plane	67
Figure 4.20	A TiN Inclusion in the Longitudinal Plane	67
Figure 4.21	Voids in the Transverse Plane, Stage 5 Sample	68

		Page
Figure 4.22	Slip Bands in the Through-Thickness Plane of the Stage 1 Sample	68
Figure 4.23	Slip Bands in the Through-Thickness Plane of the Stage 3 Sample	69
Figure 4.24	Slip Bands in the Through-Thickness Plane of the Stage 5 Sample	69
Figure 5.1	A Scintag Five Axis Pole Figure Goniometer	73
Figure 5.2	(100) and (110) Pole Figures Re-calculated by Los Alamos	75
Figure 5.3	(100) and (110) Pole Figures Simulated by Queen's University	78
Figure 5.4	The Change in the Shape of the Yield Loci with Reduction	82
Figure 5.5	Barlat's 94 Yield Loci after each Roll Pass	83
Figure 5.6	A Comparison between the Loci Predicted by Queen's University and Barlat's 94 after each Roll Pass	84
Figure 6.1	Influence of m on the Normalized Yield Stress and r-value due to Montheillet et al [61] SCHEME S	94
Figure 6.2	Influence of m on the Normalized Yield Stress and r-value due to Montheillet et al [61] SCHEME R	95
Figure 6.3	Influence of m on the Normalized Yield Loci at Stage 0, predicted by Montheillet et al	96
Figure 6.4	Comparison of the Normalized Yield Loci without a Shear Stress Term	102
Figure 6.5	Comparison of the Normalized Yield Loci with a Shear Stress Term	105
Figure 6.6	Variation in the Normalized Yield Stress with θ, for Different Yield Criteria	108
Figure 6.7	Variation in the r-value with θ, for Different Yield Criteria	110

List of Tables

		Page
Table 3.1	Experimental Data and Variables used in Figs 3.6 to 3.11	45
Table 3.2	Influence of α_z without Shear Stresses	46
Table 3.3	Influence of α_x, α_y and α_z	46
Table 3.4	Influence of m	47
Table 3.5	Influence of α_x	48
Table 3.6	Influence of α_y	48
Table 3.7	Influence of α_z	48
Table 4.1	The Chemical Composition of the Ultra-low Carbon Steel	49
Table 4.2	Sample Thickness, and the Reduction and the Rolling Strain after each Roll Pass	50
Table 4.3	Mechanical Properties of the Ultra-low Carbon Steel at Rolling Direction	55
Table 4.4	Hardness for Ultra-low Carbon Steel at Different Stages	60
Table 4.5	Thickness and Hardness for All Stages	61
Table 6.1	Basic Requirements for the Yield Criteria	89
Table 6.2	Experimental Normalized Yield Stresses at Various Stages	90
Table 6.3	Experimental r-values at Various Stages	91
Table 6.4	Normalized Pseudo-experimental and Theoretical Yield Stresses	92
Table 6.5	Exponent m at All Stages for the Four Yield Criteria	97
Table 6.6	Material Coefficients for All Yield Criteria at All Stages	97

		Page
Table 6.7	The Experimental and Theoretical Yield Stresses of All Stages	113
Table 6.8	The Experimental and Theoretical r-values of All Stages	114

Chapter 1

An Introduction

1.1 Introduction

This thesis deals with texture evolution in cold rolled steel sheet. The term texture is used to describe the orientation of the crystal structure. The texture can be *random*, which would be typical of an annealed material. Alternatively the crystals can assume a preferred orientation i.e. a significant number out of the total population of crystals are aligned, which is usually the case when a metal has been cold worked e.g. cold rolled.

Plastic deformation in metals takes place by slip (dislocation motion) on certain crystallographic planes and in a particular direction(s) on those planes. All metals have preferred slip planes and slip directions, and these depend upon the crystal structure. Slip will commence when a certain critical shear stress is reached. Crystallographic planes and slip directions are identified by Miller indices, of which a brief account is given in Chapter 2. Many common engineering metals e.g. steel, copper and aluminum, have a cubic crystal structure and in this case Miller indices are essentially direction cosines but scaled to integer values. A crystallographic plane is described by the orientation of its normal and thus a normal direction and a slip direction are analogous to a unit vector in a Cartesian coordinate system. Hence a unit vector with direction cosines $(1/3,1/3,1/3)$, in

terms of Miller indices this could represent either a (1 1 1) plane or a [1 1 1] slip direction.

The orientation of the crystal structure can exert a strong influence on the properties of a metal, particularly the magnetic and mechanical properties. For example, consider performing a tensile test on specimens cut at different orientations from a metal block. If the crystal structure were random the yield strength of each test piece would be the same i.e. the material is said to be *isotropic*. However, with a strongly textured metal the yield strength would vary with the orientation of the test piece and the material is referred to as being *anisotropic*. With sheet metals it is difficult to obtain material properties in the through thickness (or normal) direction; however, test pieces can be prepared from the plane of the sheet at different orientations to the rolling direction. Thus any variation of the yield strength within the plane of the sheet can be determined. It is possible (but rare) that there is no variation of the yield strength within the plane of the sheet, but this would not indicate whether the material was truly isotropic since the through thickness properties have not been determined. For this reason it has become customary to measure the *plastic strain ratio* in a tensile test rather than the yield stress. The plastic strain ratio (or *r-value*) is the ratio of the width strain to thickness strain of the test piece measured at a specified axial elongation. The r-value can be greater than, less than or equal to unity. The material is isotropic when the r-value is unity.

As mentioned earlier cold working will invariably promote preferred orientation of the crystal structure, and this is certainly the case when a metal is cold rolled. The process variables in a cold rolling mill include, the number of roll stands, the reduction

incurred in each stand and the sheet tension between each stand. In the present study the sheet was commercially produced in the cold mill at the *Dofasco* steel company. There are five stands in the Dofasco cold mill, and the process variables are set through a computer simulation of the rolling process (the program was developed by Dofasco personnel). Initially it was thought that some of the process variables might be changed in order to see how the resulting texture would be affected, but this proved to be impracticable. However, the cold mill was stopped during production and material was cut from the sheet between each roll stand. The subsequent tests performed on these samples are described in Chapter 4.

The reduction in the first stand of the mill is usually sufficient to exhaust the ductility of the material; at least as measured in a tensile test i.e. it is not possible to induce any measurable plastic deformation in the test piece before fracture. Consequently r-value measurements cannot be performed on the rolled samples. However, it is possible to assess the texture (degree of anisotropy) by metallurgical means. This is accomplished through the determination of *Pole Figures*, which can be produced automatically from a small sample of the rolled sheet. Pole figures display the orientation of certain crystallographic planes with respect to the rolling and transverse directions of the rolled sheet. More will be said about pole figures in Chapter 2. Mathematical manipulation (outside the scope of this thesis and the knowledge of its author) of pole figure data can provide a more complete description of the orientation of a crystal in three dimensions i.e. with respect to the rolling, transverse and normal directions of the sheet. This representation is known as the *Crystallite Orientation*

Distribution Function (CODF). Then the information of CODF can further be used for the calculation of yield loci through a Taylor-Bishop-Hill or TBH model. This computation is also outside the scope of this thesis and the knowledge of the present author. More details of CODF and TBH model are provided in Chapter 2. Note that the orthogonal axes aligned with the rolling, transverse and normal direction of the sheet are regarded as axes of symmetry as regards the texture i.e. the texture has orthotropic symmetry.

With the knowledge of a CODF some important predictions can be made regarding material properties. Firstly, if the straining path of a sheet metal specimen is known it is possible to predict the evolution of the texture at discrete intervals along the straining path. Use was made of this capability in the present study. The texture was measured (via pole figures) from the available specimens before and after reduction in each stand in the cold mill. The measured texture was then compared with predictions from the CODF analysis. Secondly, it is possible to predict a yield locus (or surface) for the rolled sheet through a TBH model once the CODF is known. In addition, the variation in the yield stress and the r-value in the plane of a rolled sheet can also be predicted. It is difficult to determine experimentally a yield locus for a sheet metal since specialized equipment is required. Therefore the ability to predict a yield locus becomes very significant, particularly if this can be done with any degree of accuracy. Once the shape of a yield locus is known the next step is to establish an analytical description i.e. an anisotropic yield function, which can be used in a numerical model (usually a finite element model) of any sheet forming process e.g. the simulation of the forming of auto-

body panels. As is well known the shape of the yield locus dictates the strain response to the applied deformation loads (stresses), and therefore it follows that knowledge of the yield function is a prerequisite for accurate modelling. The choice of a suitable anisotropic yield function was addressed in this thesis and the details can be found in Chapter 3.

1.2 Contents

Chapter 2 presents a selected literature review of topics related to this thesis. In Chapter 3 the author has presented in some detail an anisotropic yield function with the necessary flexibility to reproduce with sufficient accuracy any experimentally determined or theoretically constructed yield locus. A variety of mechanical and metallurgical tests were conducted on the steel samples cut from the rolled sheet. As already mentioned it was possible to stop the mill during the production of commercially cold rolled steel sheet, and samples were cut from the sheet between each roll stand. The details of the experiments performed are described in Chapter 4. Chapter 5 presents and discusses the measured and predicted results from texture measurement. A discussion of the results for selected yield functions is provided in Chapter 6. The conclusions and recommendations for future work are given in Chapter 7. A number of appendices are also included in the thesis and these deal mainly with listings of computer programs for generating and plotting the anisotropic yield functions discussed in Chapter 3.

Chapter 2

Literature Review

2.1 Introduction

As already mentioned the principal goals of this study were to measure (and to predict) the texture evolution in a commercially cold rolled ultra-low carbon steel and to assess some of the more widely adopted yield functions for anisotropic metals.

In this chapter some of the published work on texture measurement and analysis is reviewed along with a review and discussion of anisotropic yield criteria. Inherent in texture analysis is the identification of crystallographic planes and the slip direction along such planes. It is universally accepted that crystallographic planes and directions are identified with the use of Miller Indices and a brief explanation of these indices is given in the next section.

2.2 Miller Indices

Attention is restricted to cubic lattice structures only, a more detailed discussion on the topic can be found in the book by Barrett and Massalski [1]. Directions in a cubic lattice are completely analogous to direction cosines in a Cartesian coordinate system, the difference being is that the direction cosines are converted to their lowest integer values to reveal the Miller indices. For example, the direction cosines 1/3, 1/3, 1/3 revert to Miller indices 1, 1, 1. It is convention to surround the indices with a square bracket to identify a direction, thus [1 1 1]. Now consider the direction cosines 1/2, -1/2, 0; the

corresponding Miller indices for the direction are expressed as [1 $\bar{1}$ 0]. Note that the bar over the second integer value signifies a negative direction.

Crystallographic planes are also identified by sets of integers and these are obtained from the intercepts a plane makes with the coordinate axes. Consider a plane which intercepts the x, y, and z axes at 1, 3 and 2 unit-cell distances respectively. The Miller indices are proportional to the reciprocal of the intercepts i.e. 1/1, 1/3 and 1/2, and, by definition, the Miller indices are the smallest integer values having the same ratio as the reciprocals. The desired integers are, therefore, 6, 2, 3. The Miller indices of a plane are enclosed in parentheses, for example (6 2 3), instead of square brackets, thus making it possible to differentiate between planes and directions. It is useful to note that for the cubic lattice the Miller indices of a plane are also the Miller indices for the direction of the normal to that plane.

Often it is necessary to specify planes of a crystallographic type, for example, all the faces of the unit cell (the so-called cube faces). Thus the class of all cube faces is denoted by {1 0 0}, which includes the (1 0 0), (1 0 0), (0 1 0), (0 1 0), (0 0 1) and (0 0 1) planes. Similarly to specify the equivalent set of directions normal to these planes i.e. [1 0 0], [0 1 0] etc., it is customary to designate them as <100>.

To specify a particular direction, say [110], on a particular crystallographic plane, say (001), the two sets of indices are combined as follows (001)[110]. The general designation is often expressed as (hkl)[uvw]. To refer to an equivalent set of directions on like crystallographic planes, the designation {hkl}<uvw> is used.

2.3 Texture Measurement and Analysis

2.3.1 Plastic Deformation in Metals: Crystallographic Approach

In single crystals of many metals it is well known that the main mechanism of plastic deformation, on a microscopic scale, is a simple shear parallel to certain crystallographic planes and in a particular direction. According to Schmid's Law for yielding in a single crystal, slip will first occur on that system which first attains the critical value of resolved shear stress, τ^*. In a rod shaped crystal under uniaxial tension σ, by stress transformation

$$\tau = \sigma \cos \phi \cos \lambda, \tag{2.1}$$

where ϕ and λ are the angles made by the slip plane normal and slip direction to the rod axis respectively, see Fig. 2.1. Hence σ has to be increased (until some yield value σ_y) until the critical stress, τ^*, is achieved on the active system.

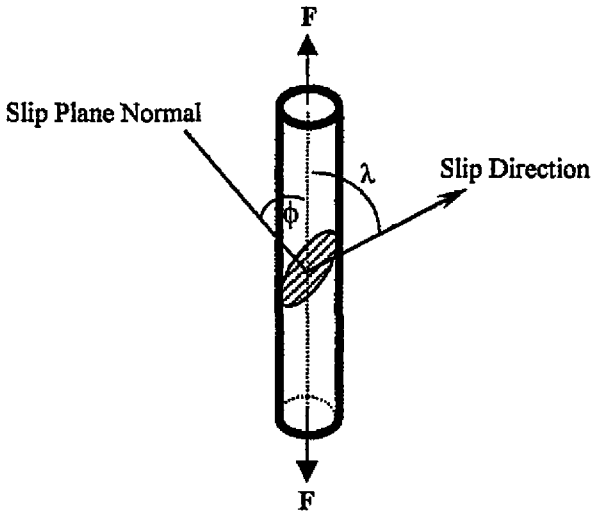

Figure 2.1 Slip under a Uniaxial Tension F

It is not difficult, at least in principle, to envisage how strengthening can be obtained through preferred orientation; useful strengthening being achieved when the orientation of the crystal structure makes slip and hence yielding more difficult under the applied stress system. Similar remarks on texture hardening apply when considering polycrystalline metals, although complicating features can arise through the presence of grain boundaries and the constraints imposed on the flow of an individual grain by its neighbours.

Much of the work on the yield strength of plastically constrained crystals stems from the study by Taylor [2, 3] on face centred cubic (f.c.c.) metals. Taylor assumed that plastic deformation of the aggregate was effected by slip on the {111}<110> system only*, and each grain within the aggregate undergoes the same strain. For incompressible flow an arbitrary imposed shape change requires, in general, the operation of five dependent shears from all possible operative slip systems. Many choices are available, but Taylor hypothesized that the actual set of active glide shears is that in which their absolute sum is a minimum. Subsequent analyses by Bishop and Hill [4, 5], based on the principle of maximum work, verified the minimum shear hypothesis of Taylor and demonstrated that the yield stress is reached on the active set without being exceeded elsewhere.

* The equivalent system in body centred-cubic (b.c.c.) metals is {110}<111>. However, there is also evidence that {112} and {123} are slip planes with slip occurring in the <111> directions.

The Taylor analysis, as extended by Bishop and Hill is often referred to as the TBH model, and Hosford and Backofen [6] applied the model to cubic metals having preferred orientation. These authors predicted the most probable r-value (see Chapter 4) arising from ideal sheet textures and they indicated how the analysis could be applied to predict the behaviour of textured sheets with several textural components.

The Schmid law, given by eqn. (2.1) for the case of uniaxial tension, can be generalized to account for more complex stress states, furthermore the most likely slip systems on which the critical shear stress is attained e.g. {111}<110> in f.c.c. crystals, can be specified. The generalized law was employed by Piehler and Backofen [7] to determine polycrystalline yield loci for sheet material possessing ideal textures, subjected to combined principal stresses applied in the rolling and transverse directions. See also the book by Backofen [8].

The TBH model is applicable to polycrystalline metals and is used in the texture analysis of real metals as described in section 2.3.3.

2.3.2 Determination of Pole Figures

Diffraction techniques are now well established for measuring textures in polycrystalline metals. The main methods involve either X-rays [9-13], neutrons [14-15] and electrons [16-17]. The use of X-rays is the oldest method and the determination of pole figures through X-ray goniometry is one of the most widely applied techniques. A coupon of material is placed on a holder in the machine (goniometer) which moves the specimen with respect to an incident X-ray beam and the intensity of the reflected beam

is monitored by a Geiger counter. The machine is set up to determine the orientation of a particular crystallographic plane, say the {111} or {110} planes. The pole figure is a stereographic projection of the plane normal (or pole) and shows the variation in density with orientation. The orientation is measured with respect to a set of coordinate axes defined for the specimen. For a rolled sheet the specimen axes are the rolling, transverse and normal (through thickness) directions, since these are regarded as the principal axes of anisotropy. Figure 2.2 is an idealized portrayal of the creation of a pole figure; the clustering of the {100} poles for the fictitious polycrystal is so dense the pole figure closely resembles that of a single crystal. Note that the intensity of the contour lines are plotted as a multiple of the intensity of a random sample. An actual pole figure is shown in Fig 2.3, taken from Ref [18].

2.3.3 Crystalline Orientation Distribution Functions (CODFs)

The mathematical development of CODFs from pole figure data is beyond the knowledge of the author. Some pertinent references are provided below for the interested reader but no discussion of the details is provided.

One disadvantage of pole figures is that they provide information about the distribution of plane normals and do not contain information about the rotation around these normals. Three angles are required to describe fully the orientation of a crystallite with respect to a physical reference frame. Again consider the rolling (RD), transverse (TD) and normal (ND) directions to be the reference axes for a rolled sheet. Initially the axes of the unit cell x, y, z i.e. [100], [010], [001], are assumed aligned with the reference

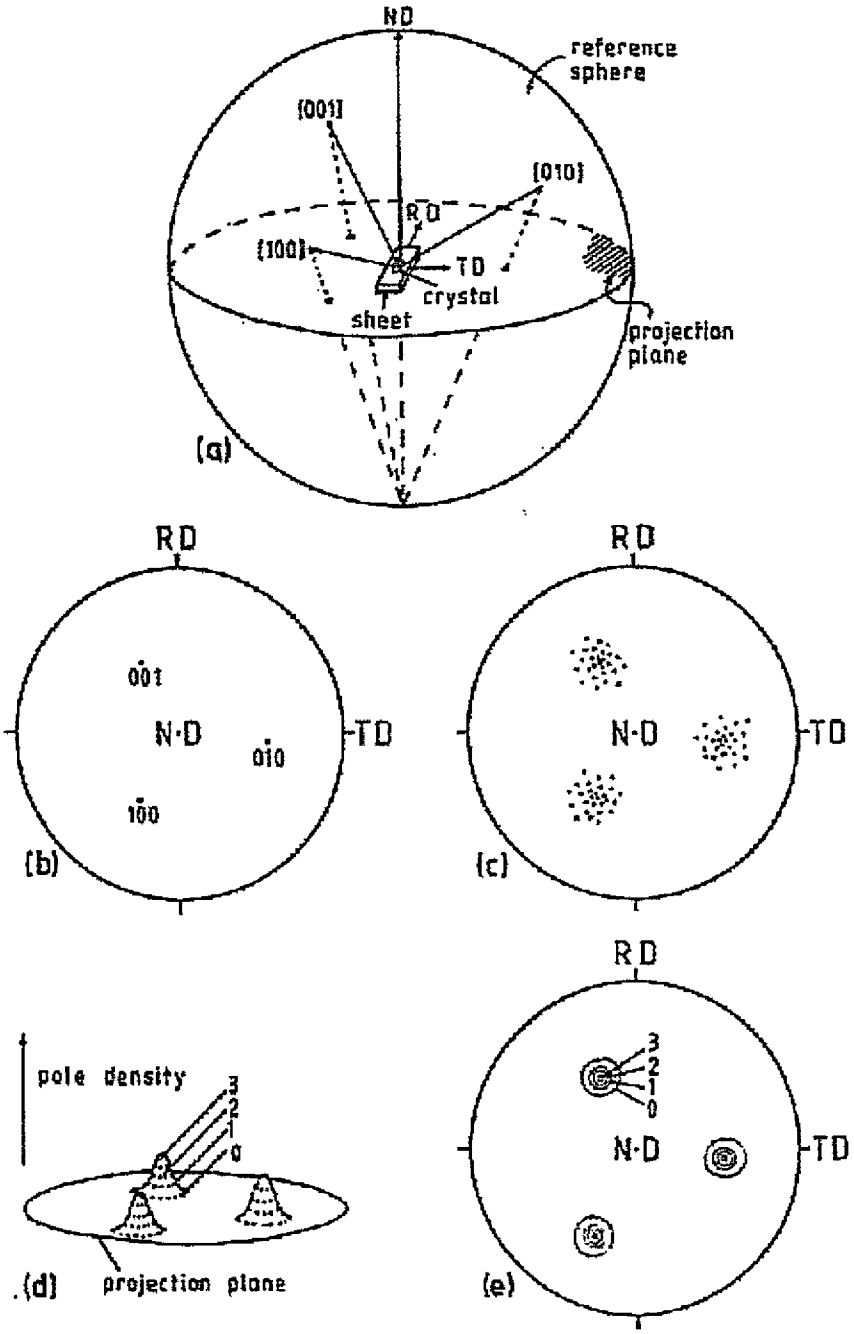

Figure 2.2 Process of Pole Figure Creation:
(a) Stereographic Projection
(b) A Single Crystallite
(c) Textured Crystallites
(d) Pole Density Distribution
(e) Contour Lines

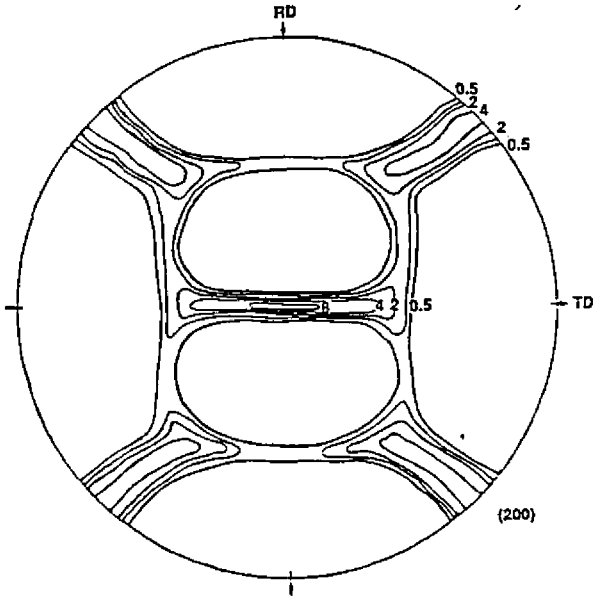

Figure 2.3 A (200) Pole Figure for Rolled Molybdenum

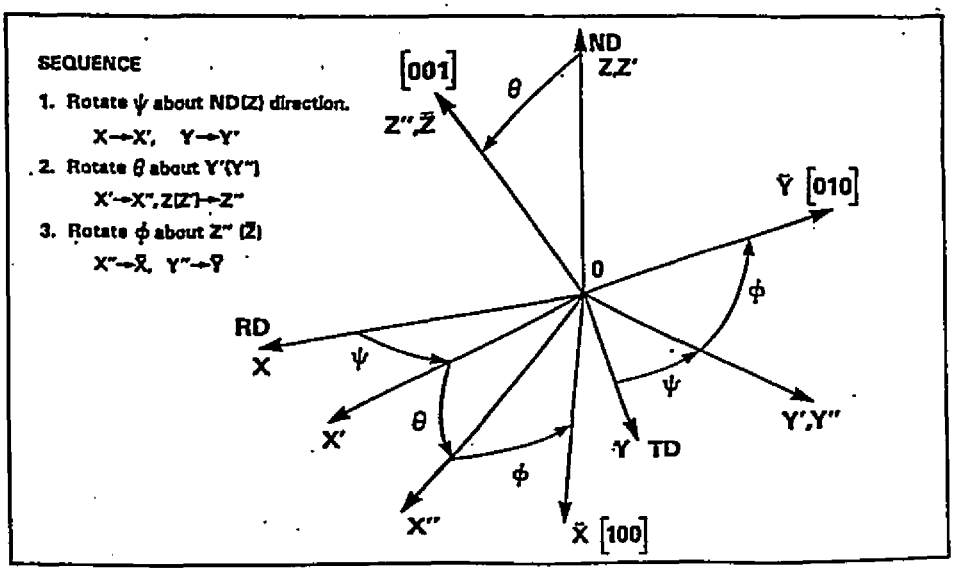

Figure 2.4 Sequential Rotation of Roe's Notation

axes. Now rotate the crystallite in the sequence shown in Fig 2.4, where the angles Ψ, Θ and Φ are known as the Euler angles. The sequence shown in Fig 2.4 is due to Roe [19], while Bunge [20] proposed a similar sequence but where the second rotation (defined as ϕ in Bunge's notation) is about the X' axes rather than the Y'. In Bunge's notation the Euler angles are φ_1, ϕ, φ_2, and according to Wenk et al [21] there is little difference in either method. For equivalence the sets of angles are related as follows [22],

$$\varphi_1 = \Psi + \pi/2,\ \phi = \Theta,\ \varphi_2 = \Phi - \pi/2;$$

See also Refs 23 and 24.

From a given set of Euler angles a specific ideal orientation (hkl)[uvw] can be determined, where (hkl) represents the normal to a plane lying in the plane of a rolled sheet and [uvw] are the Miller indices aligned with the rolling direction of the sheet. The method of evaluating the Miller indices from a set of Euler angles is described by Davies et al [25].

For the case of cubic crystals Roe [19] and Bunge [20] independently proposed a general analytical method for obtaining the CODF from a limited number of pole figure distributions. The CODF is given by a series of generalized spherical harmonics.

Figure 2.5, taken from Ref [26], shows a CODF plotted in Euler space based on Bunge's notation. Note the CODF represents the probability of a crystallite having a particular orientation. It is customary to present the results by taking constant sections of one of the Euler angles, either φ_1 or φ_2 in Bunge's notation. Figure 2.6 shows some results using constant φ_2 sections. Ideal orientations (hkl)[uvw] are represented as single points in each of these sections and can be used to facilitate the interpretation of the

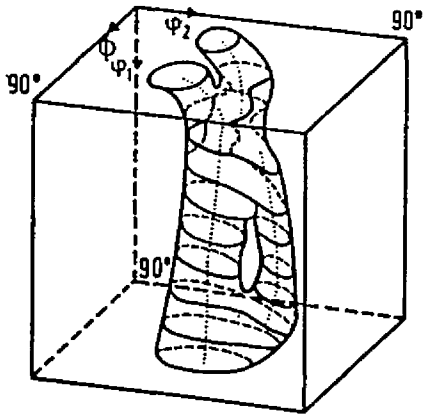

Figure 2.5 The Representation of CODF of A Recrystallized Iron

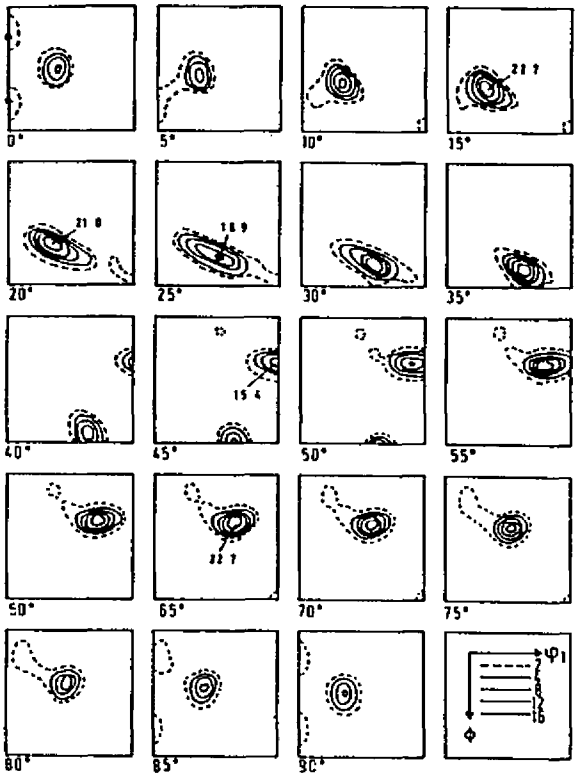

Figure 2.6 Sectional View of CODF for A Cold Rolled Copper after 95% Reduction

CODF as discussed in Ref [25]. Nevertheless, for the non-expert the interpretation of CODFs is generally more difficult than pole figures.

The utility of the CODF lies in its predictive capabilities since it permits a more rigorous means of correlation between texture and mechanical properties. It is now possible to predict the variation in both tensile yield strength and the r-value (see Chapter 5) with orientation in the plane of a rolled metal sheet, once having determined the CODF of the sheet. These analytical techniques are described in Refs. [27-31]. The predictions can be checked against experimental data by performing tensile tests on specimens cut from the plane of the sheet at different orientations to the rolling direction.

The CODF permits the prediction of plane-stress crystallographic yield loci based on either the generalized Schmid law or the TBH analysis. In Refs [32, 33] predictions for a number of sheet metals are given, see also [27, 34-37]. Figure 2.7, taken from Ref [38], shows a comparison of plane-stress crystallographic yield loci which have been determined experimentally, predicted from the CODF using the TBH technique and also from anisotropic yield models. Anisotropic yield models are a feature of this thesis and a detailed discussion will be found in Chapters 3 and 6.

The CODF in conjunction with a selected crystallographic slip system, e.g. {111}<110> in f.c.c. crystals, can be utilized to predict the change in texture under an imposed straining mode. The technique involves a discretization of the CODF by selecting a finite number of crystallites (say one or two thousand). An increment of strain is imposed and the rotation and deformation of the individual crystallites calculated. This is repeated over the entire strain path, at which stage the crystallites are re-assembled to

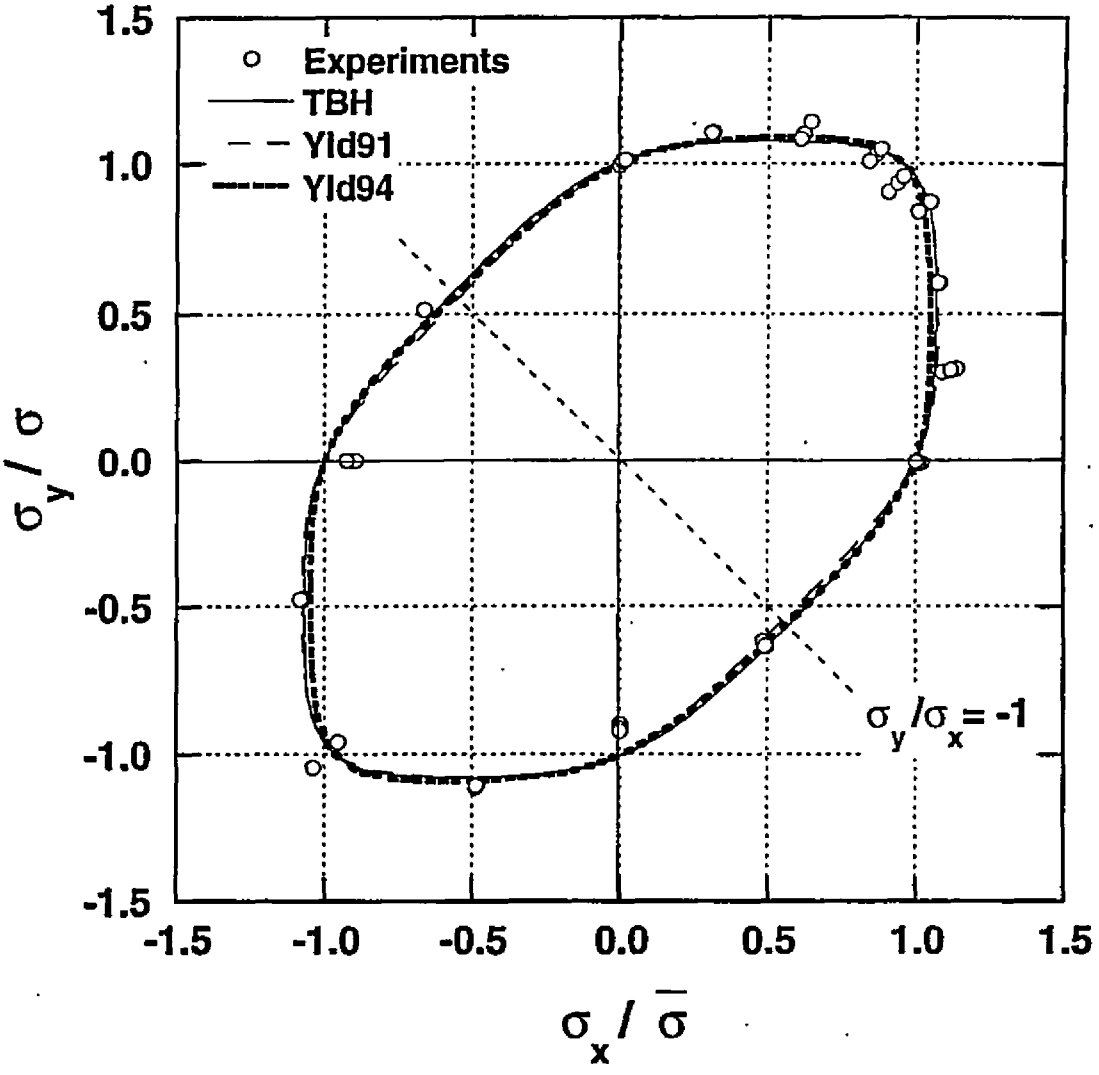

Figure 2.7 A Comparison of Normalized Planar Yield Surfaces from Experiments, TBH polycrystal, Barlat's 91 and 94 Yield Criteria

produce the deformed CODF. If required pole figures can also be determined from the resulting CODF. There is still some latitude on the choice of the active slip systems and Kallend and Davies [39] have discussed this point in their simulation of rolling textures in f.c.c. metals. Van Houtte [40] has also predicted rolling textures but has allowed for mechanical twinning. Calculations of texture simulation for other deformation modes are to be found in Refs [33, 40]. These and other predictions of textures and yield loci from the CODF have been reviewed in details in Refs [24, 66, 68-69, 83-84].

The foregoing has concentrated on the methods of Bunge [20] and Roe [19] for calculating the CODF from a limited number of pole figures based on a series of generalized spherical harmonics. However, other mathematical techniques are available to arrive at the CODF and some of these are described in Refs [41-44]. Refs [26, 82, 85-87] extensively review and compare all the mathematical methods for computing CODFs.

Texture analysis packages are now available around the world and are employed by industry, universities and government research laboratories. In the current work the author has made use of a CODF software package developed at Queen's University (Kingston, Ontario) in conjunction with the Aluminium Company of Canada. The program was used to simulate the cold rolling textures as described in Chapter 5. Texture measurements on the cold rolled samples were performed at the Los Alamos National Research Laboratories (New Mexico, USA) and served as a comparison for the predictions from the Queen's University software, the details are given in Chapter 5. A sophisticated CODF analysis package (named popLA) has been developed by the

researchers at Los Alamos, but since the texture measurements were made at Los Alamos it was decided to use an alternative software package to predict the texture evolution.

2.4 Anisotropic Yield Functions

In order to simulate any metalforming process with reasonable accuracy it is necessary that the numerical scheme embodies a realistic description of how the material yields. Considerable attention has been paid to developing mathematical models of the yielding behaviour. Such models describe the shape of the yield surface (usually in two dimensional stress space) in terms of various coefficients, which may or may not be physically based. The degree of anisotropy affects the shape of the yield locus, and since the shape dictates the resulting strain distribution in a deformed metal part it is desirable to account for the state of anisotropy.

One of the earliest, but still widely applied, anisotropic yield functions is due to Hill [45, 46]. In its simplest form it is a modification of the isotropic yield criterion proposed by von Mises, and under plane stress conditions plots as an ellipse in two dimensional, principal stress space i.e. with σ_{11} and σ_{22} as the co-ordinate axes. The aspect ratio of the ellipse is controlled through a single r-value (see Chapter 4 for a discussion on r-value), which defines the state of anisotropy of the material. Over the years Hill's model has been shown to have a number of limitations and many alternative anisotropic yield functions have appeared in the literature [38, 45-65, 88-89]. These yield criteria can be broadly classified as being either a quadratic [45-46, 53-54] or non-quadratic [38, 49-52, 55-65, 88-89] function of the stress. It is not the purpose of this

study to provide an in-depth review of the large number of yield criteria that have been published. In fact some excellent reviews are to be found in Refs. [65-70, 90].

After reading some of the published literature on the topic, the present author selected an anisotropic yield model which he believes is flexible enough to describe with good accuracy the shape of a wide range of anisotropic yield loci. The model is due to Barlat and his co-workers [38] and is described in some detail in Chapter 3 of this thesis. In particular, the manner in which the various coefficients etc in the yield function are calculated is described. It is to be noted that not all the calculations are presented in great details in either Ref [38] or in Barlat's earlier publications [47-48, 57-58]. It is not intended to dismiss all other proposed yield criteria as being inappropriate, and in this regard the author devoted a great deal of time in exploring the applicability (and limitations) of four additional anisotropic yield criteria [50, 61, 63, 65], which have all received considerable attention in the literature. The predictive capabilities of these criteria are compared with those of Ref [38] in Chapter 6.

In the next section a brief review of some non-quadratic anisotropic yield functions is provided.

2.4.1 A Brief Review of Non-Quadratic, Anisotropic Yield Functions

As mentioned above one of the earliest anisotropic yield functions is due to Hill [45]. This was proposed in 1948 and it has subsequently been shown to have a number of shortcomings. One of these was the so-called r-value anomaly i.e. if the r-value was greater than one the Hill model predicted that the biaxial yield stress would exceed the

uniaxial yield stress and vice-versa. Experiments performed by Woodthorpe and Pierce [71] on sheets of aluminum alloy showed that this was not true (bearing in mind that the material was not planar isotropic). This leads to proposals for using a non-quadratic yield function where the stresses are raised to some power in which is no longer equal to 2. Hill [62-63] was one of the first investigators to propose a non-quadratic yield function once the anomaly had been reported. Parmer and Mellor [72], following some correspondence with Hill, proposed a yield function which was a special case of one of the models in Ref [62] and overcame the r-value anomaly. Other non-quadratic function have been proposed by Gotoh [55, 56], Hosford [50-52], Barlat et al [38, 47-48, 57-58], Zhou [59, 60], Montheillet et al [61], Lin et al [64], Karafillis and Boyce [49], Maniatty et al [88] and Keum et al [89].

It should be noted that in order to facilitate the plotting of any yield locus, anisotropic or not, the applied stress system is invariably limited to the case of plane stress with components σ_{xx}, σ_{yy} and σ_{xy}. Quite often the shear stress term is omitted and a further restriction that is often imposed is that the stresses σ_{xx} and σ_{yy} are applied along the principal axes of anisotropy of the material, and the anisotropy is assumed to possess orthotropic symmetry. In a rolled metal sheet, the principal axes of anisotropy are taken to be the rolling and transverse directions of the sheet and the direction normal to the plane of the sheet.

Gotoh [55, 56] introduced a fourth order ($m = 4$) plane stress yield function with 10 independent coefficients. While the model can overcome the r-value anomaly, several mechanical tests (at least 4 tensile and one combined loading test) are required to

evaluate the various coefficients. However, it has been pointed out in Ref [66] the coefficients have no physical meaning. Hosford [50-52] suggested a yield function which is also a special case of one of the models proposed by Hill [62]. Based on some crystallographic calculations for b.c.c. and f.c.c metals, Hosford, op cit, selected m to be either 6 or 8. The model could predict plane stress loci (with σ_{11} and σ_{22} as coordinate axe) that were in agreement with some calculated crystallographic yield loci and also some experimentally determined yield loci. However, the model cannot explain the r-value anomaly and furthermore it is extremely difficult to introduce an applied shear stress into the formulation [73]. In Ref [63] Hill proposed a function which allowed for three applied stresses i.e. σ_{xx}, σ_{yy} and σ_{xy}, and where the coefficient m could be calculated from some experimentally determined mechanical properties. The yield function can account for the r-value anomaly. However, Lin et al [64] and Naruse et al [74] have noted that under certain circumstances Hill's model [63] can result in yield loci which are not convex outward over the entire surface. This is a serious shortcoming because there have been a vast number of experimental investigations conducted to determine the shape of yield loci and none of these have ever reported yield loci with re-entrant zones; they have always been convex outward. Zhou [59] introduced a two component stress function (σ_{xx} and σ_{yy}) which is a modification of one of the models developed by Hill [62]. Zhou's function can reduce to the non-quadratic function proposed by Hosford [50] and with m = 2 it transforms to the 1948 model of Hill [45]. Zhou, op cit, did not demonstrate whether the model could satisfy the r-value anomaly. However, the model appeared to be able to reproduce some experimentally determined

loci for both titanium and aluminum alloys. In a subsequent article Zhou [60] extended the model to include the shear stress term σ_{xy}. As already mentioned, Hill's 1990 model [63] embodies the three stress components σ_{xx}, σ_{yy} and σ_{xy}. The coefficient m can be determined explicitly providing certain mechanical properties of the material are known. In the context of rolled sheet (which is usually the material of choice when the applied stress system is plane stress) the required material data are the r-value and the uniaxial yield stress determined from tensile tests conducted at 45 degrees to the rolling direction. Other parameters in the yield function can be evaluated based on either the r-value at 45° i.e. r_{45} or the yield stress at 45° i.e. σ_{45}; see Chapter 6. Lin [64] modified Hill's 1990 model [63] by introducing two new parameters and discarding the shear stress term. As with Hill's function the coefficients in the model can be determined based on r_{45} or σ_{45}, and Lin suggested that σ_{45} is to be preferred since the criterion appears to be very sensitive to slight changes in the r-values. Montheillet et al [61] introduced a function somewhat different in form to that proposed by Hill [63]. It contains all three plane stress components and five independent coefficients, one of which is calculated based on either r_{45} or σ_{45}. It can account for the r-value anomaly. Recently Hill [65] has attempted a simpler criterion, where all the stress are raised to the power m = 2. However, the terms are so arranged that the resulting function is dimensionless in stress; there is no shear stress in the expression. The function can describe the situation where the uniaxial yield stress in the rolling and transverse directions are equal and the corresponding r-values are different and vice-versa. This is a situation that could arise in practice and yet the most of the functions presented in this section cannot account for this fact. The work of Barlat

and his co-workers [38, 47-48] is discussed in Chapter 3, which covers in detail the procedures for calculating the coefficients in the yield functions, particularly those which appear in Ref [38]. Its formulation depends on some of the work proposed by Karafillis and Boyce [49], and these details are also provided in Chapter 3. It is noted that all Barlat's yield functions mentioned above have been useful for describing the plastic anisotropy of aluminum alloys and Refs [89, 91-96] have demonstrated their predictive capabilities. More recently, Maniatty et al [88] proposed a function which is also based on the formulation developed by Karafillis and Boyce [49] to describe microstructural texture. The function is a more generalization of Hill's the earliest criterion [45, 46] but it can be only use on weakly textured materials. Keum et al [89] postulated a new approach to determine the anisotropic coefficients of Barlat's model. However, only the yield stresses predicted by the approach were significantly improved.

Some of the yield functions mentioned above have been paid much attention in areas, such as FEM simulation for deep drawing process [92-97, 101] and the prediction of forming limit digrams (FLDs) [98-101]. More recently, Xu et al [98] and Cao et al [99] applied the functions proposed by Hill [45-46, 62, 65], and Karafillis and Boyce [49] to predict FLDs. Among the functions used, Hill's 93 model predicted the best trend of forming limits strains for AA 6111-T4. Inal et al [92] and Yoon et al [93] simulated the earing profile for aluminum alloys during the circular cup drawing using Hill's [45-46] and Barlat's models [48, 58]. Yoon et al [94] suggested that for good earing predictions, the difference between the tensile and compressive yield stresses is taken into consideration. Kim [95] used Hill's [45-46] and Barlat's model [38] to predict wrinkling.

Chapter 3

A Theoretical and Numerical Analysis of Barlat's 94 Yield Criterion

3.1 Introduction

In Chapter 2, some of the more popular yield criteria for describing the behaviour of anisotropic metals were reviewed. The more flexible criteria, i.e. those capable of providing a more faithful reproduction of experimentally determined yield loci, usually involve non-quadratic stress functions. In addition, these criteria can deal with a six-component stress state, i.e. all the components of the Cauchy stress tensor, σ_{ij}, are being applied. In practice, it is too difficult to apply all six stress components simultaneously, and therefore, experimental yield loci are usually determined under a state of plane stress, i.e. the only stress components acting are σ_{xx}, σ_{yy} and σ_{xy}, and in many experiments one of these components is zero.

As mentioned in Chapter 2, an anisotropic yield criterion due to Barlat and his co-workers [38] has received considerable attention. It appears capable of reproducing yield loci determined from experiments on cold rolled sheet metals, and therefore is applicable to some of the experimental and theoretical work performed in this thesis. For these reasons, the yield criterion proposed by Barlat et al [38] is discussed in some detail in this Chapter. It turns out that considerable effort is involved in establishing the parameters in the theoretical yield function. A number of experiments have to be performed in order to characterize the anisotropy of the rolled sheet. The rolling (say x), transverse (y) and

through thickness (z) directions are usually regarded as the axes of orthotropic symmetry for the state of anisotropy of the sheet. Numerical iteration is then required to establish the magnitude of certain coefficients (which describe the state of anisotropy) in the yield function. Very few details of the numerical procedures are given in Barlat's published papers on the subject [38, 47-48]. However, the present author has met and corresponded with Dr. Barlat, and the exchange of information has proved extremely useful by enabling the author to perform the necessary calculations to establish the material coefficients embedded in the yield criterion. Detailed computer programs, written in MATLAB [75] are given in Appendices C, D, E and F. Appendix C lists the yield function program, Appendix F provides a program for finding r-values and yield stresses, while Appendices D and E provide the programs for plotting the yield loci with and without shear stress, respectively.

3.2 Calculation of the Yield Function

3.2.1 The Numerical Method when No Shear Stresses Act

Barlat et al [38] first proposed a yield function suitable for the case when the applied stress system does not contain any shear stress. The direct stresses are assumed to act along the x, y, z directions of the rolled sheet, i.e. the principal axes of anisotropy. The form of the yield function is

$$\phi = \alpha_x |s_{yy}-s_{zz}|^m + \alpha_y |s_{zz}-s_{xx}|^m + \alpha_z |s_{xx}-s_{yy}|^m = 2\bar{\sigma}^m, \qquad (3.1)$$

where m is a positive integer, $\bar{\sigma}$ is a measure of the strength of the material and the α's are used to describe, in part, the anisotropy of the material. The s_{xx} etc are normal

components of a stress tensor which is a modification of the applied stress components. The modification can be stated formally as (see Karafillis and Boyce [49])

$$\mathbf{s} = \mathbf{L}\,\sigma, \tag{3.2}$$

where $\mathbf{L}$ is a fourth order tensorial operator, which is used to describe anisotropy. The operator $\mathbf{L}$ can describe many kinds of material symmetry such as, triclinic, monoclinic, orthotropic etc. As shown in Ref [49], when orthotropic symmetry is considered only 6 components of $\mathbf{L}$ are not zero. The representation of this tensor by 6x6 matrix in the axes of orthotropic symmetry for the rolled sheet, is given below

$$\mathbf{L} = \begin{bmatrix} (c_3+c_2)/3 & -c_3/3 & -c_2/3 & 0 & 0 & 0 \\ -c_3/3 & (c_3+c_1)/3 & -c_1/3 & 0 & 0 & 0 \\ -c_2/3 & -c_1/3 & (c_2+c_1)/3 & 0 & 0 & 0 \\ 0 & 0 & 0 & c_4 & 0 & 0 \\ 0 & 0 & 0 & 0 & c_5 & 0 \\ 0 & 0 & 0 & 0 & 0 & c_6 \end{bmatrix} \tag{3.3}$$

In the above the c_i are material coefficients that described anisotropy. When no shear stresses exist, the following relationship ensues,

$$\begin{bmatrix} s_{xx} \\ s_{yy} \\ s_{zz} \end{bmatrix} = \begin{bmatrix} (c_3+c_2)/3 & -c_3/3 & -c_2/3 \\ -c_3/3 & (c_3+c_1)/3 & -c_1/3 \\ -c_2/3 & -c_1/3 & (c_2+c_1)/3 \end{bmatrix} \begin{bmatrix} \sigma_{xx} \\ \sigma_{yy} \\ \sigma_{zz} \end{bmatrix} \tag{3.4}$$

The values of s_{xx} etc determined from (3.4) are then inserted into (3.1)

For the isotropic case, when $c_1=c_2=c_3=1$, the components of $\mathbf{s}$ are the deviatoric stress components of σ. If these are substituted into (3.1), along with the isotropic condition $\alpha_x=\alpha_y=\alpha_z=1$, the isotropic yield function proposed by Hosford [50-52] is revealed. Hosford, op cit., showed that the exponent m can have a marked effect on the

shape of the locus. When $m \rightarrow \infty$, the Tresca yield function is revealed and when m=2, the function reduces to that of von-Mises.

As discussed in Ref [38] experiments have to be performed to obtain the coefficients c_1, c_2, c_3, α_x, α_y and α_z. It was suggested obtaining the yield stress in the x, y, z directions, the biaxial yield stress in the x-y plane and the r-values (the ratio of the width to thickness strain) in the x and y directions. However, the yield stress in compression in the z-direction is equal to the biaxial yield stress in the x-y plane. It should also be noted that (3.1) does not allow for differences in the yield stress in tension and compression along the axes of orthotropy.

As with the case of classical, isotropic, plasticity theory, the plastic strain increment (or rate) is normal to the yield surface at the loading point. The individual plastic strain increment components are obtained by partially differentiating (3.1) with respect to the corresponding applied stress components. The normality condition can be expressed as

$$\partial\phi/\partial\sigma = (\partial\phi/\partial s)\cdot(\partial s/\partial\sigma) = \mathbf{L}\,(\partial\phi/\partial s) \tag{3.5}$$

For example, the r-value in the rolling (x) direction is given by

$$r_x = d\varepsilon_{yy}/d\varepsilon_{zz} \tag{3.6}$$

Hence from (3.5)

$$r_x = \frac{\partial\phi/\partial\sigma_{yy}}{\partial\phi/\partial\sigma_{zz}} \tag{3.7}$$

which can be evaluated once the c_i and α_i coefficients have been determined.

3.2.1.1 Determination of the c Coefficients

Barlat et al [48] suggested that the quantity $\bar{\sigma}$ in (3.1) be identified with the biaxial yield stress, say σ_b. Now consider performing a uniaxial tensile test in the rolling (x) direction of the sheet. From (3.4) the components of **s** are

$$\left.\begin{aligned} s_{xx} &= \frac{c_3 + c_2}{3}\sigma_{xx} \\ s_{yy} &= \frac{-c_3}{3}\sigma_{xx} \\ s_{zz} &= \frac{-c_2}{3}\sigma_{xx} \end{aligned}\right\} \tag{3.8}$$

Substitute these components into (3.1) to obtain

$$\alpha_x |c_2+c_3|^m + \alpha_y |2c_2+c_3|^m + \alpha_z |2c_3+c_2|^m - 2\left(3\frac{\bar{\sigma}}{\sigma_{xx}}\right)^m = 0$$

where $\bar{\sigma}$ is equated with σ_b. Similar expressions to the above are obtained when performing uniaxial tests in the y and z directions. Adopting the notation given by Barlat and Chung [47], it follows that

$$g_x(c_1,c_2,c_3,\alpha_x,\alpha_y,\alpha_z) = \alpha_x |c_2+c_3|^m + \alpha_y |2c_2+c_3|^m + \alpha_z |2c_3+c_2|^m - 2\left(3\frac{\bar{\sigma}}{\sigma_{xx}}\right)^m = 0$$

with similar expressions for the y and z directions. There exists three equations from which to find the six values of c_i and α_i. As mentioned by Barlat et al [38], of the set of coefficients c_1, c_2, c_3, α_x, α_y and α_z only 5 are independent, therefore, we can set α_z to any convenient value, say unity. Hence another two equations are needed to calculate those anisotropic coefficients.

Again consider the case of a uniaxial tensile test in the rolling (x) direction. The experimental r-value in the rolling direction r_0 must be equal to the calculated r-value r_x using equation (3.7), i.e.

$$r_x = \frac{\partial\phi/\partial\sigma_{yy}}{\partial\phi/\partial\sigma_{zz}} = r_0 \tag{3.9}$$

Now adopting the notation as given above, it follows

$$g_{rx}(c_1,c_2,c_3,\alpha_x,\alpha_y,\alpha_z) = \frac{\partial\phi/\partial\sigma_{yy}}{\partial\phi/\partial\sigma_{zz}} - r_0 = 0$$

Similar expression to the above is also obtained for the r-value in the transverse (y) direction r_y. Thus these five equations are used to find all five unknown coefficients. Initially, all the c's and α's were set equal to unity and the system of equations solved numerically using a Newton-Raphson procedure. The following algorithm was suggested in Ref [47], and was adopted by the present author,

$$\mathbf{c}_{n+1} = \mathbf{c}_n - \mathbf{J}^{-1}(c_n)\mathbf{g}(c_n), \tag{3.10}$$

where $\mathbf{c}$ is a vector of the unknown anisotropic coefficients, $\mathbf{g}$ is a vector of the simultaneous nonlinear equations g_i and g_{ri}, and $\mathbf{J}$ is the Jacobian of the system of equations $\mathbf{g} = 0$, that is

$$\mathbf{c} = \begin{bmatrix} c_1 \\ c_2 \\ c_3 \\ \alpha_x \\ \alpha_y \end{bmatrix}, \qquad \mathbf{g} = \begin{bmatrix} g_x \\ g_y \\ g_z \\ g_{rx} \\ g_{ry} \end{bmatrix},$$

and

$$\mathbf{J} = \partial\mathbf{g}/\partial\mathbf{c}. \tag{3.11}$$

At each iteration determine the error from (3.10), i.e. $\mathbf{J}^{-1}\mathbf{g}$, until it falls within an accepted limit. In this present work, the error was set as $\pm\ 1x10^{-12}$.

A flow chart of the algorithm for calculation of the c and α coefficients is given in Fig. 3.1. A computer program for calculating the yield function is given in Appendix C. The routine for evaluating the coefficients is embedded in the main program.

Owing to insufficient rolled material, the author did not have the experimental measures of the r-values and yield stresses that are required to perform the calculations just described. The only experimental measurements available were the yield stress in the rolling (x) direction of the sheet at the various stages of reduction and the r-value in the rolling direction of the undeformed sheet. However, from the texture analysis described in Chapter 5, it was possible to obtain predicted yield loci for the material after being reduced in each roll stand. The variation of the r-value in the plane of the rolled sheet could also be predicted. The author used the data from the texture analysis to serve as the experimental values. For example, since the shape of the yield locus is known and a value for the yield stress in the rolling (x) direction is known, then the yield locus can be scaled to obtain the biaxial yield stress and the yield stress in the transverse (y) direction.

To demonstrate the method the author selected the case where only two stresses, σ_{xx} and σ_{yy}, are applied to the rolled sheet. Pseudo-experimental values were determined in the manner just described, and used to evaluate the coefficients c_1, c_2, c_3, α_x, α_y (α_z=1) as explained earlier. There is a convenient way of substituting values of σ_{xx} and σ_{yy} into the yield function (3.1), and this is explained with reference to a normalized yield locus

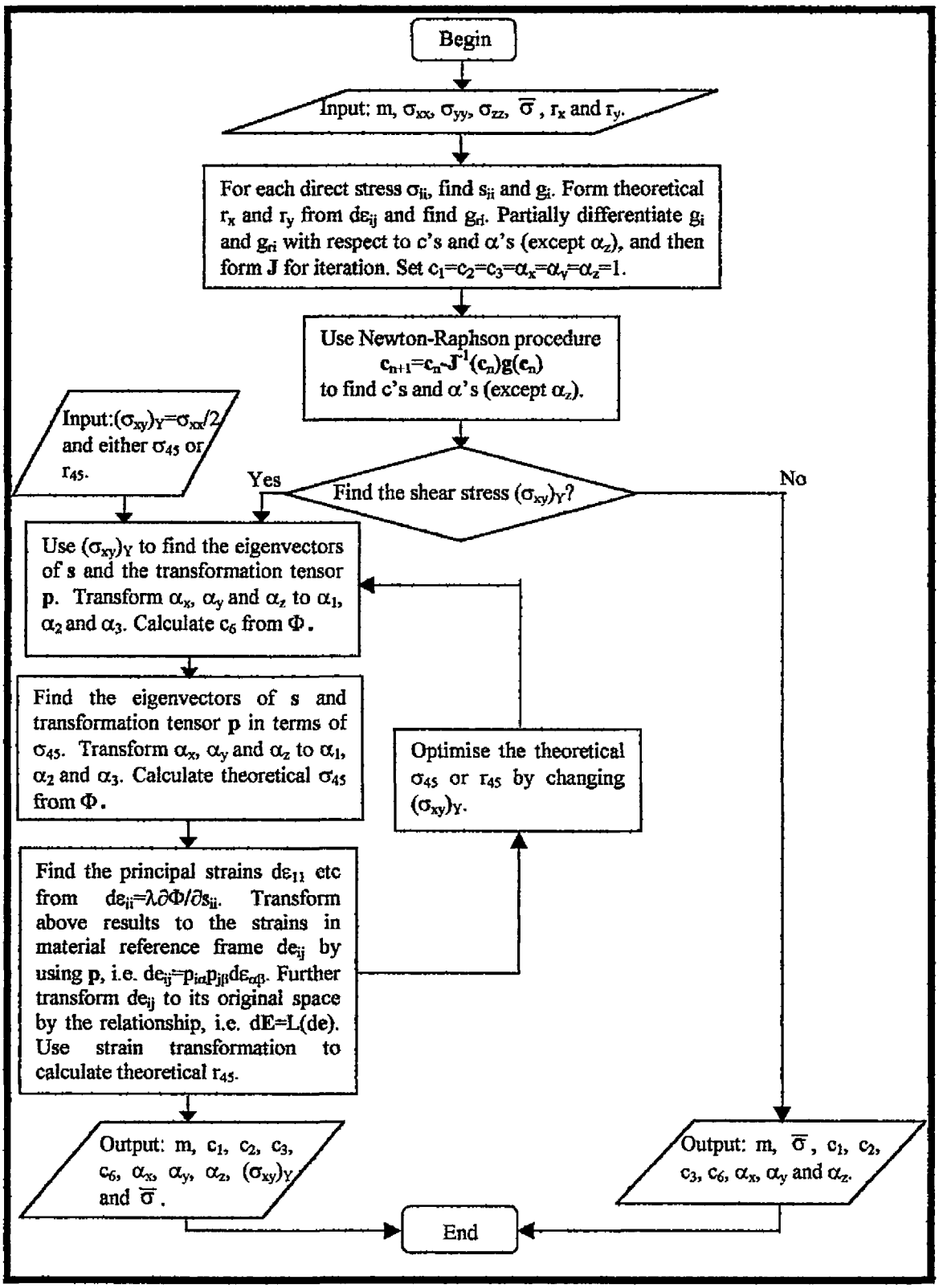

Figure 3.1 A Flow Chart of Yield Criterion with and without Shear Stress $(\sigma_{xy})_Y$

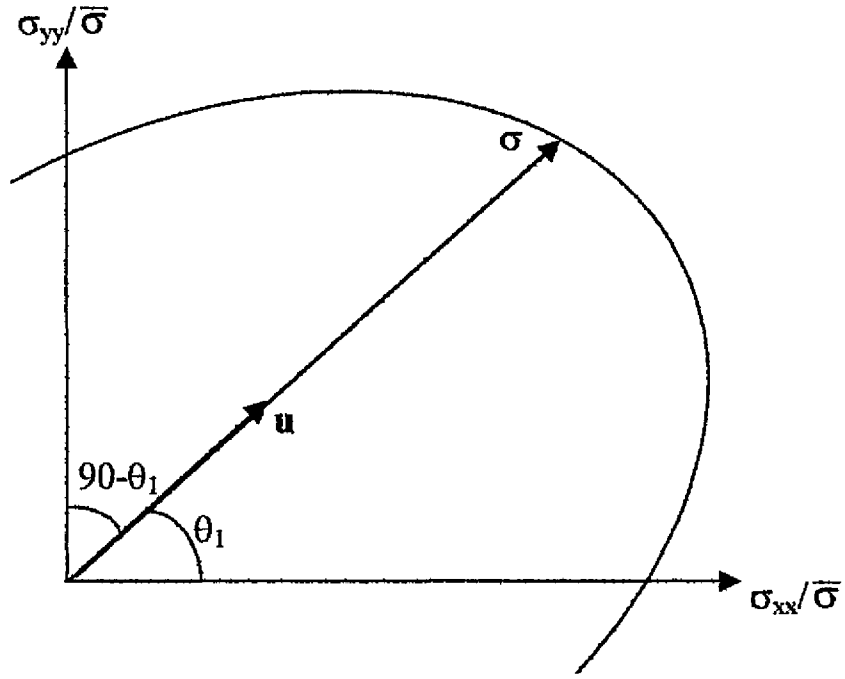

Figure 3.2 A General Point on the Normalized Yield Locus

shown in Fig 3.2. Let σ represent the stress state at a general point on the yield locus, let **u** be a unit vector in the direction of σ and define σ as the norm of σ such that

$$\boldsymbol{\sigma} = \sigma \mathbf{u}, \tag{3.12}$$

where the components of **u** are $\cos\theta_1$ and $\cos(90\text{-}\theta_1)$. The normalized stress components are

$$\left.\begin{aligned} \frac{\sigma_{xx}}{\overline{\sigma}} &= \sigma\cos\theta_1 \\ \frac{\sigma_{yy}}{\overline{\sigma}} &= \sigma\cos(90-\theta_1) = \sigma\sin\theta_1 \end{aligned}\right\} \tag{3.13}$$

The yield function (3.1) can now be as expressed as

$$\phi(\sigma) = \phi\left(\frac{\sigma_{xx}}{\overline{\sigma}}, \frac{\sigma_{yy}}{\overline{\sigma}}\right) = 2 \tag{3.14}$$

where the α and c coefficients are embedded in the function. Now substitute (3.13) into (3.14) and the result can be expressed as

$$\sigma^m f(\mathbf{u}) = 2 \tag{3.15}$$

where $f(\mathbf{u})$ is a function of the material coefficients and also $\cos\theta_1$ and $\sin\theta_1$. Equation (3.15) can be rearranged as

$$\sigma = \left\{\frac{2}{f(\mathbf{u})}\right\}^{\frac{1}{m}}. \tag{3.16}$$

Hence with the aid of (3.13), the following relationships ensue

$$\left.\begin{aligned} \frac{\sigma_{xx}}{\overline{\sigma}} &= \left\{\frac{2}{f(\mathrm{u})}\right\}^{\frac{1}{m}} \cos\theta_1 \\ \frac{\sigma_{yy}}{\overline{\sigma}} &= \left\{\frac{2}{f(\mathrm{u})}\right\}^{\frac{1}{m}} \sin\theta_1 \end{aligned}\right\} \tag{3.17}$$

From (3.17) the normalized stress components are in a convenient form for plotting the normalized yield locus, since the only variable is the angle θ_1.

A more detailed account of the derivation summarized by (3.12) through (3.17) is given in Appendix A.

3.2.2 A Numerical Method Appropriate for the Case when Shear Stresses Act

The stresses are still being applied with respect to orthotropic axes (x, y, z) of the rolled sheet. Equation (3.2) still applies, but the fourth order tensorial operator, **L**, is now given by (3.3). Upon using (3.3) in (3.2) the components of **s** can be obtained from

$$\begin{bmatrix} s_{xx} \\ s_{yy} \\ s_{zz} \\ s_{yz} \\ s_{zx} \\ s_{xy} \end{bmatrix} = \begin{bmatrix} (c_3+c_2)/3 & -c_3/3 & -c_2/3 & 0 & 0 & 0 \\ -c_3/3 & (c_3+c_1)/3 & -c_1/3 & 0 & 0 & 0 \\ -c_2/3 & -c_1/3 & (c_2+c_1)/3 & 0 & 0 & 0 \\ 0 & 0 & 0 & c_4 & 0 & 0 \\ 0 & 0 & 0 & 0 & c_5 & 0 \\ 0 & 0 & 0 & 0 & 0 & c_6 \end{bmatrix} \begin{bmatrix} \sigma_{xx} \\ \sigma_{yy} \\ \sigma_{zz} \\ \sigma_{yz} \\ \sigma_{zx} \\ \sigma_{xy} \end{bmatrix} \tag{3.18}$$

After expanding the right hand side of (3.18) to obtain s_{xx} etc, it is necessary to find the eigen (or principal stress) values, s_{11}, s_{22} and s_{33}, of the resulting stress tensor. This can be achieved in the usual manner by solving the following characteristic equation

$$\det\{\mathbf{s} - s\mathbf{I}\} = 0 \tag{3.19}$$

where **I** is the identity tensor. Once the eigen (principal stress) values have been determined, the eigen vectors (or principal stress directions) can be evaluated from

$$(\mathbf{s} - s_k\mathbf{I})\mathbf{p}_k = 0, \tag{3.20}$$

where $\mathbf{p}_k$ is the principal direction associated with the corresponding principal stress value, say s_k. The above equation can be rewritten as

$$\begin{bmatrix} s_{xx}-s_k & s_{xy} & s_{xz} \\ s_{yx} & s_{yy}-s_k & s_{yz} \\ s_{zx} & s_{zy} & s_{zz}-s_k \end{bmatrix} \begin{bmatrix} p_{xk} \\ p_{yk} \\ p_{zk} \end{bmatrix} = 0 \tag{3.21}$$

The above equation can be solved to reveal the direction cosines for each of the three principal stress directions. The Gram-Schmidt process [79] was used to facilitate the

calculation. Through **p** there now exists the means of transforming from the x, y, z directions (the principal directions of anisotropy) to the principal directions, say 1, 2, 3, of the stress tensor **s**.

The yield function of (3.1) is now generalized as

$$\Phi = \alpha_1 |s_{22}-s_{33}|^m + \alpha_2 |s_{33}-s_{11}|^m + \alpha_3 |s_{11}-s_{22}|^m = 2\,\bar{\sigma}^m \qquad (3.22)$$

Note that it is necessary to transform the α_x, α_y, α_z coefficients in (3.1) to the principal axes of **s** according to

$$\alpha_k = \alpha_x p_{xk}^2 + \alpha_y p_{yk}^2 + \alpha_z p_{zk}^2,\ k = 1, 2, 3 \qquad (3.23)$$

The mathematical fundamentals have now been laid for evaluating the function (3.22) under different conditions of applied stress. We are only going to consider the situation where the only shear component is σ_{xy}. Hence the z-direction is a principal stress direction.

The **c** and α coefficients are evaluated as described in Section 3.2.1.1, and the same pseudo-experimental data was employed. It is not necessary to perform stress transformation calculations because if the yield stress in the x, y, z directions is used in turn then s_{xx}, s_{yy} and s_{zz} are principal stress components, see (3.8). However, another piece of experimental data is required in order to evaluate the coefficient c_6. The most appropriate would be the yield shear stress, $(\sigma_{xy})_Y$. Since the author did not have access to such information it was assumed, in the first instance, that the yield shear stress was one half the yield stress in the x-direction. If only $(\sigma_{xy})_Y$ is applied, then from (3.18) the only components of **s** are

$$s_{xy} = s_{yx} = c_6 (\sigma_{xy})_Y \qquad (3.24)$$

It is then easy to prove that the three eigen values are $s_{11} = -s_{22} = c_6(\sigma_{xy})_Y$, $s_{33}=0$ with the following direction cosines $(1/\sqrt{2}, 1/\sqrt{2}, 0)$, $(1/\sqrt{2}, -1/\sqrt{2}, 0)$, $(0,0,1)$ respectively. From (3.23) it follows that

$$\alpha_1 = \alpha_2 = (\alpha_x+\alpha_y)/2, \quad \alpha_3 = \alpha_z.$$

Upon substituting s_{11}, α_1 etc, into (3.22) it follows that

$$c_6 = \left\{\frac{2}{(\alpha_x + \alpha_y + 2^m \alpha_z)}\right\}^{\frac{1}{m}} \left\{\frac{\bar{\sigma}}{(\sigma_{xy})_Y}\right\} \tag{3.25}$$

There has to be some means of confirming the initial guess for the quantity $(\sigma_{xy})_Y$. One way is to determine the yield stress and r-value in a direction at 45° to the rolling (x) direction of the sheet, say σ_{45} and r_{45}. The author had access to a value for r_{45} from the texture analysis described in Chapter 5, and this was used as the pseudo-experimental value. The determination of a theoretical value for r_{45} requires several steps and the details are given in Appendix B.

Once a theoretical value for r_{45} has been determined a comparison is made with the experimental value. If a discrepancy is observed then $(\sigma_{xy})_Y$ is adjusted. This in turn modifies the value of c_6 from (3.25). If the experimental value of r_{45} is greater than the theoretical value, c_6 should be decreased. The steps, outlined in Appendix B, are then repeated until an acceptable difference (error) between the theoretical and "experimental" value of r_{45} is obtained. The chosen limit on the error was $\pm 5\text{x}10^{-5}$. The iteration procedure is embedded in the program for calculating the yield locus given in Appendix C.

3.2.2.1 Evaluating and Plotting the Yield Locus for a Case of Plane Stress

This is the case when only the components σ_{xx}, σ_{yy} and σ_{xy} act. In the same manner as described earlier, see (3.12) through (3.17), it is convenient to consider a normalized yield locus in $\sigma_{xx}/\bar{\sigma}$, $\sigma_{yy}/\bar{\sigma}$ and $\sigma_{xy}/\bar{\sigma}$ space, see Fig. 3.3. As before, σ represents a normalized stress state on the yield locus and (3.12) still holds. However, the components of the unit vector **u** are $\cos\theta_1\cos\theta_2$, $\sin\theta_1\cos\theta_2$, $\sin\theta_2$. The normalized stress components are

$$\left.\begin{aligned} \frac{\sigma_{xx}}{\bar{\sigma}} &= \sigma\cos\theta_1\cos\theta_2 \\ \frac{\sigma_{yy}}{\bar{\sigma}} &= \sigma\sin\theta_1\cos\theta_2 \\ \frac{\sigma_{xy}}{\bar{\sigma}} &= \sigma\sin\theta_2 \end{aligned}\right\} \tag{3.26}$$

Now substitute these values into (3.18), with $c_4=c_5=0$, and evaluate the components s_{xx} etc. Evaluate the eigen values and eigen vectors of the **s** tensor in the manner indicated by (3.19) through (3.21). Then obtain the α_1, α_2 coefficients as shown by (3.23), with $\alpha_3=\alpha_z=1$. The α_1, s_{11} etc values are substituted into (3.22). The yield function can be reduced to the following form

$$\sigma^m F(\mathbf{u}) = 2 \tag{3.27}$$

which should be compared with (3.15). The function $F(\mathbf{u})$ is a function of the material coefficients and the components of **u**. Upon using (3.26) in conjunction with (3.27) it follows that

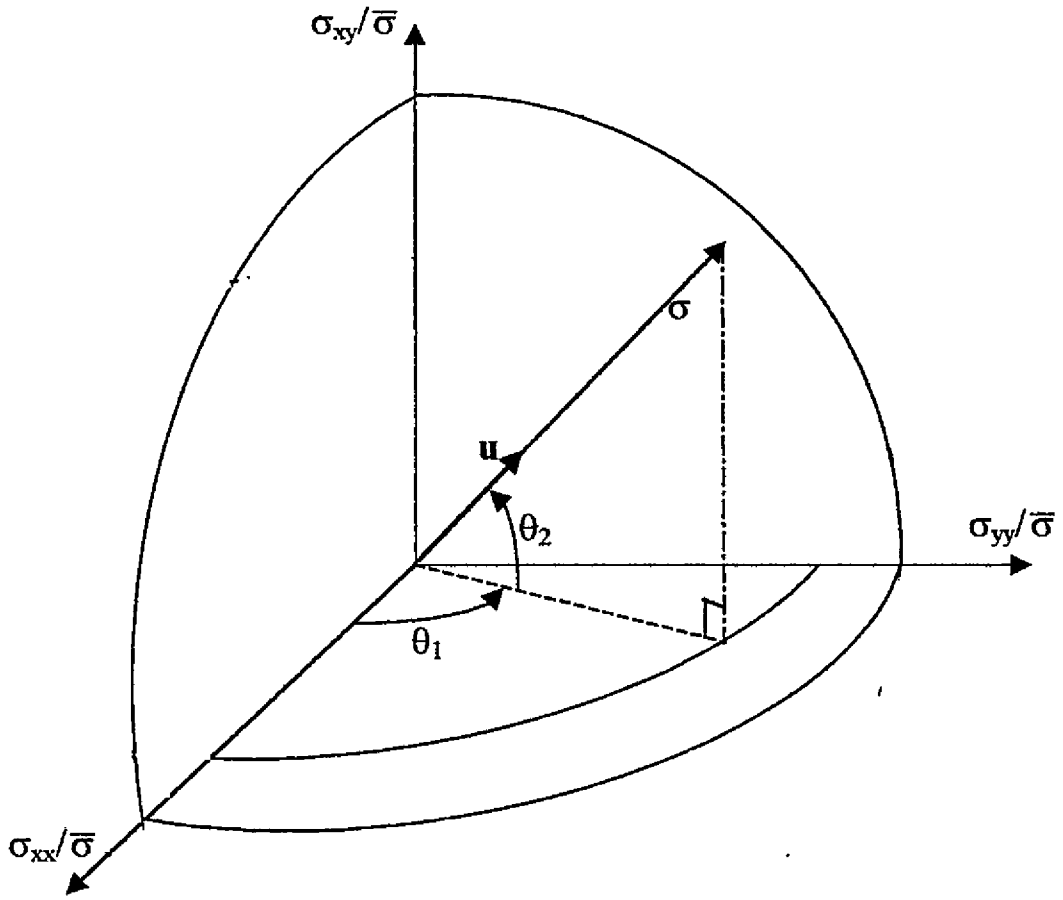

Figure 3.3 A General Plane Stress State on the Normalized Yield Locus

$$\left.\begin{aligned}\frac{\sigma_{xx}}{\bar{\sigma}} &= \left\{\frac{2}{F(u)}\right\}^{\frac{1}{m}} \cos\theta_1 \cos\theta_2 \\ \frac{\sigma_{yy}}{\bar{\sigma}} &= \left\{\frac{2}{F(u)}\right\}^{\frac{1}{m}} \sin\theta_1 \cos\theta_2 \\ \frac{\sigma_{xy}}{\bar{\sigma}} &= \left\{\frac{2}{F(u)}\right\}^{\frac{1}{m}} \sin\theta_2\end{aligned}\right\} \qquad (3.28)$$

Equations (3.28) provide a convenient form for plotting the yield locus. The technique is to pick a value for the ratio $\sigma_{xy}/\bar{\sigma}$, along with a value for θ_1 and then vary θ_2 until the third equation in (3.28) is satisfied. Repeat the process with a new value of θ_1 to plot the yield locus in $\sigma_{xx}/\bar{\sigma}$ vs $\sigma_{yy}/\bar{\sigma}$ space for a fixed value of $\sigma_{xy}/\bar{\sigma}$. With this technique nested yield loci can be plotted each corresponding to a different value of $\sigma_{xy}/\bar{\sigma}$, see Figs 3.4 and 3.5. Note, the bounding yield locus in Fig. 3.4 corresponds to zero shear stress i.e. $\sigma_{xy}/\bar{\sigma} = 0$.

The foregoing steps are shown in greater detail in Appendix A.

3.3 An illustration of how the α Coefficients and the Exponent m can influence the shape of the Yield Locus and the variation in the r-value

The goal of this section is to provide an indication of the role that the α coefficients and the exponent m can play in influencing the shape of the yield locus. The first case considered was their effect in a plane stress yield locus, $\sigma_{xx}/\bar{\sigma}$ vs $\sigma_{yy}/\bar{\sigma}$, when $\sigma_{xy}/\bar{\sigma} = 0$. In this illustration, the fixed values were $m = 6$, $\alpha_x = \alpha_y = 1$, and α_z was the quantity that was varied between 0 and 2 in steps of 0.5. In order to make the

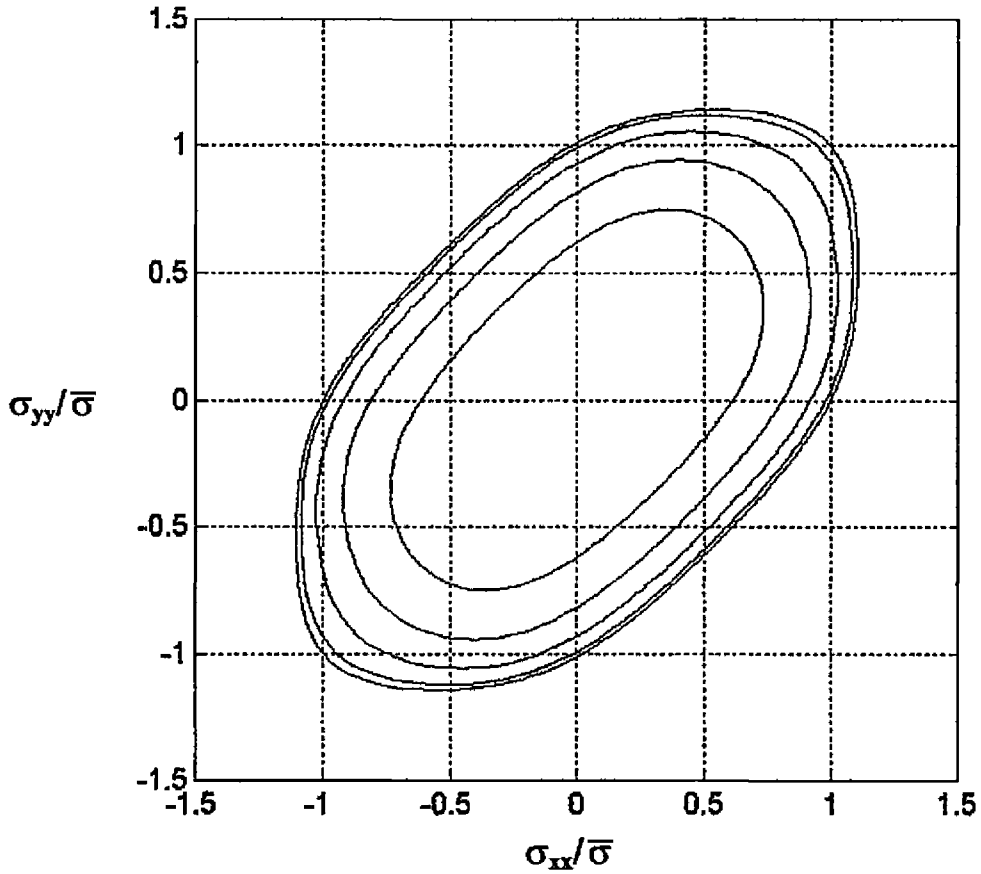

Figure 3.4 A Projection of the Shear Contours in a 2-D View

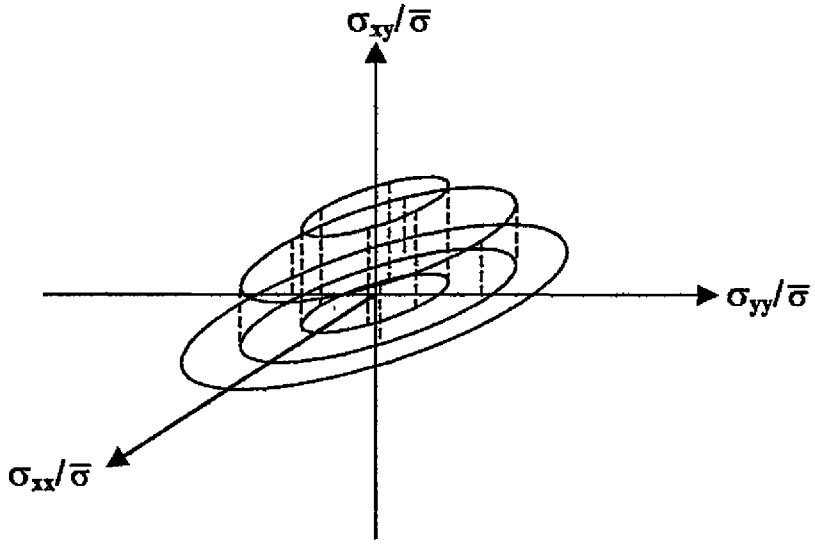

Figure 3.5 A Projection of the Shear Contours in a 3-D View

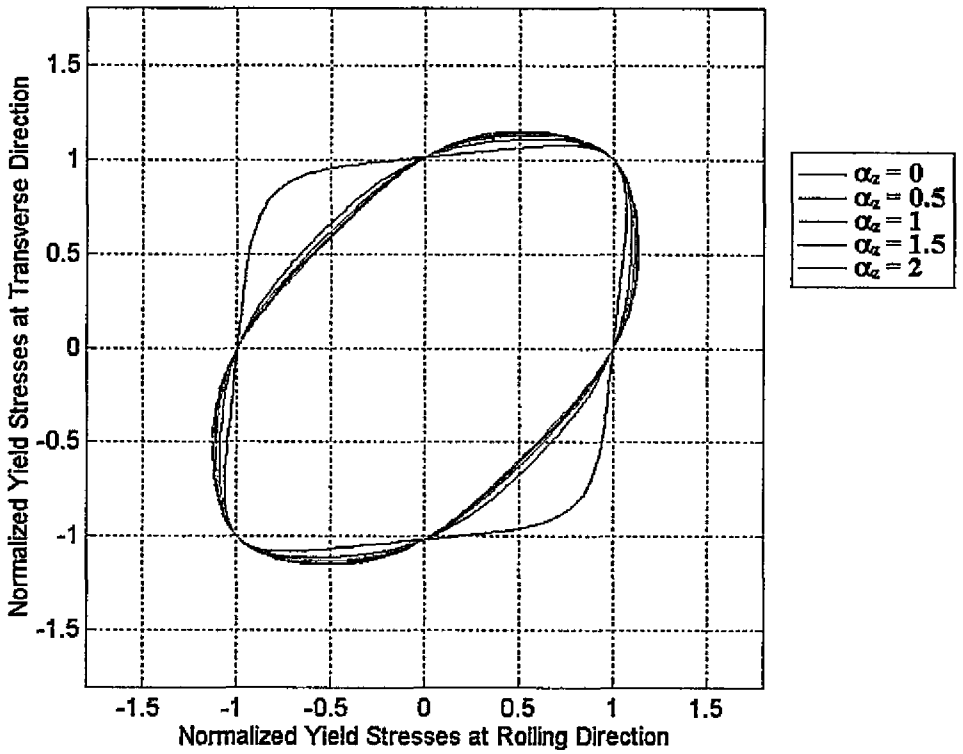

Figure 3.6 Influence of α_z on the Shape of the Yield Locus

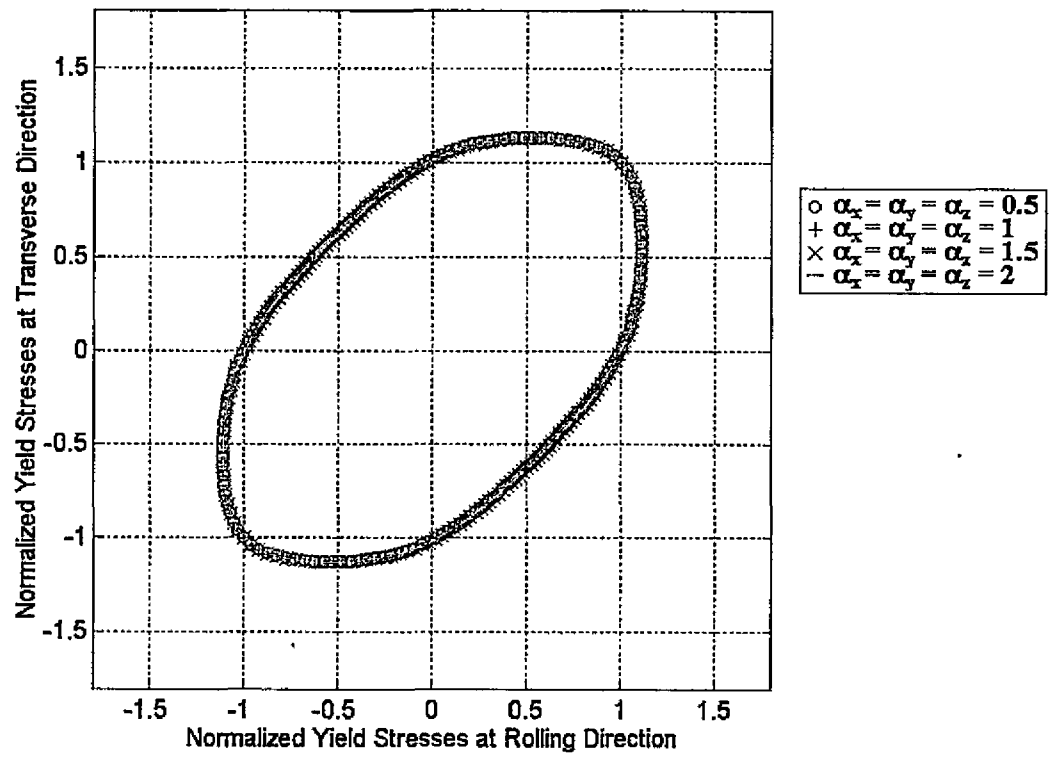

Figure 3.7 Influence of α_x, α_y and α_z on the Shape of the Yield Locus

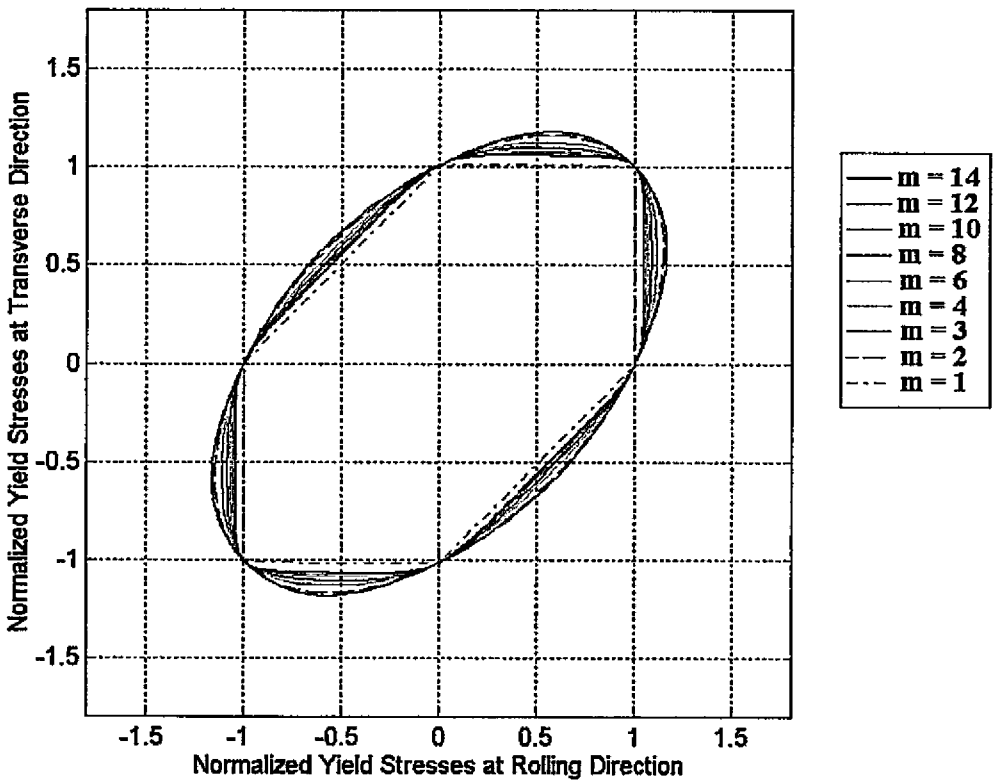

Figure 3.8 Influence of m on the Shape of the Yield Locus

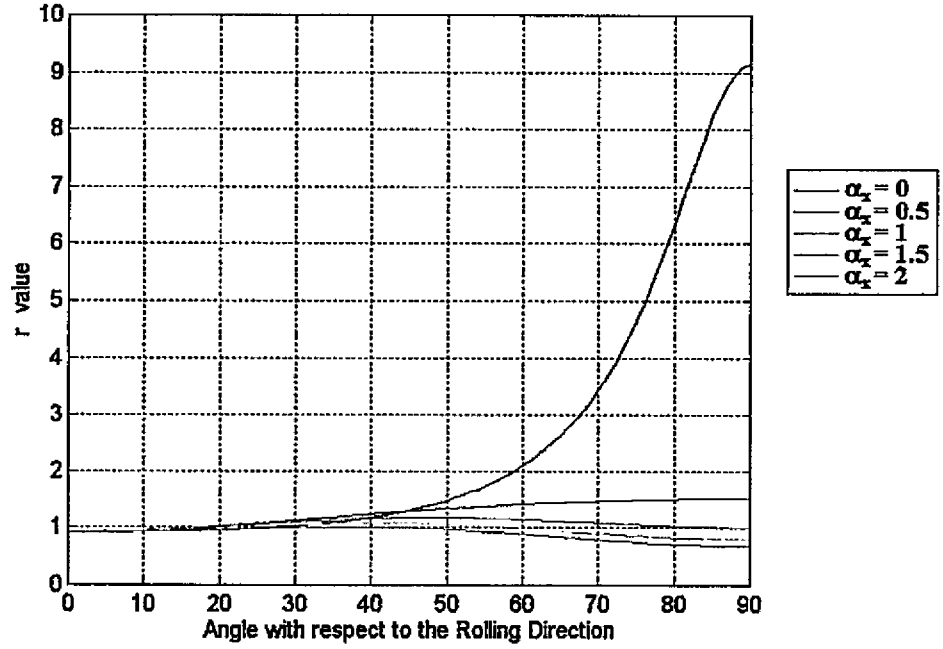

Figure 3.9 Influence of α_x on the Variation in the r-value

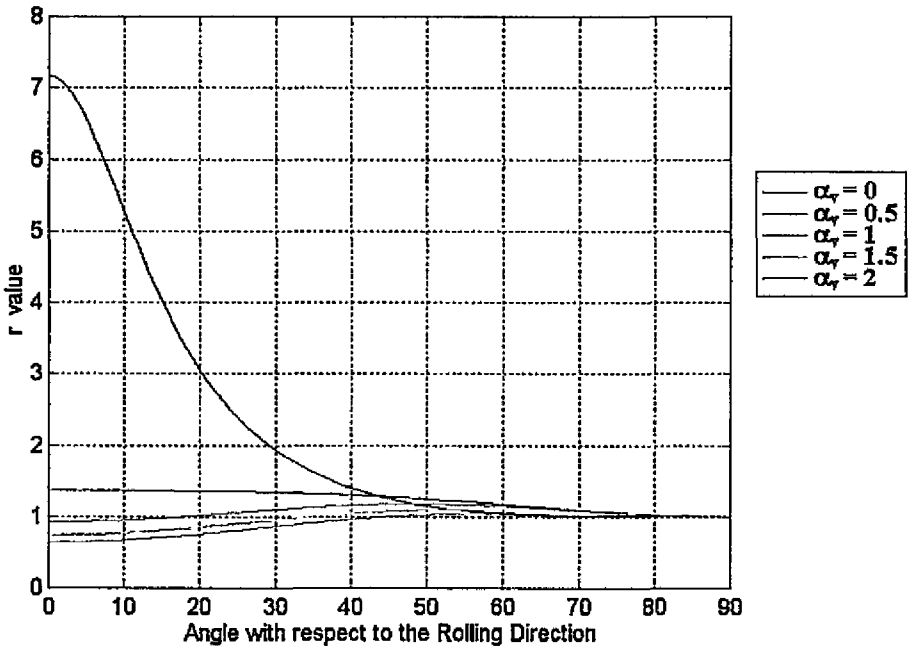

Figure 3.10 Influence of α_y on the Variation in the r-value

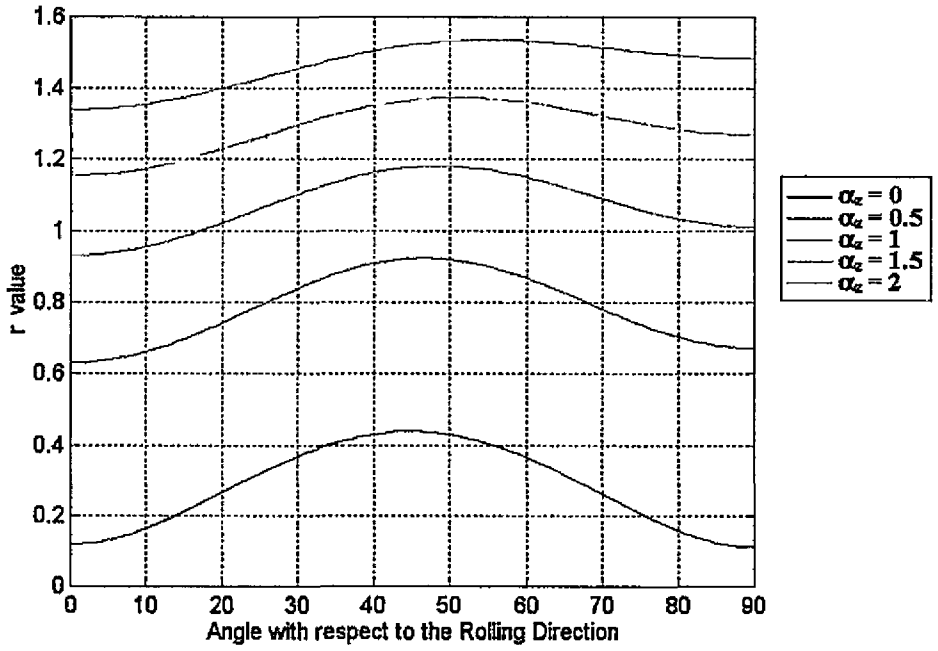

Figure 3.11 Influence of α_z on the Variation in the r-value

calculations more realistic a procedure very similar to that described in Section 3.2 was followed to calculate the c coefficients. The experimental values of the yield strength in the x, y and z directions are still required to calculate the c coefficients, but in the present case the α values were selected. The author did not have access to such experimental data, and as described in Section 3.2.1.1 data from a theoretical yield locus generated using CODF analysis was used instead. The theoretical yield locus was calculated for the "as-received" material i.e. the ultra-low carbon steel sheet prior to entering the rolling mill. The biaxial yield stress, σ_b, was assumed to be equal to the through thickness yield strength, σ_{zz}, and the ratio $\sigma_{zz}/\overline{\sigma}$ was taken as being equal to unity. The values for $\sigma_{xx}/\overline{\sigma}$ and $\sigma_{yy}/\overline{\sigma}$ are given in Table 3.1. The calculated c values for the different values of α_z are listed in Table 3.2. The influence of α_z on the yield locus is evident from Fig. 3.6.

Additional calculations were performed maintaining m = 6, but setting the α values equal to each other i.e. $\alpha_x = \alpha_y = \alpha_z$. The α values were then incremented from 0 to 2 in steps of 0.5. This had little effect on the shape and level of the resulting yield loci as shown in Fig. 3.7. The corresponding values of c_1, c_2 etc are given in Table 3.3.

Table 3.1 Experimental Data and Variables used in Figs 3.6 to 3.11

Experimental Data	Variables
σ_{xx}=0.9978	m
σ_{yy}=1.0135	α_x
σ_b=σ_{zz}=1.0000	α_y
σ_{45}=0.5352	α_z

Table 3.2 Influence of α_z without Shear Stresses

m=6, α_x=α_y=1			
α_z	c_1	c_2	c_3
0	0.9869	1.0130	1.3487
0.5	0.9849	1.0149	1.0962
1	0.9844	1.0154	0.9889
1.5	0.9843	1.0156	0.9207
2	0.9842	1.0157	0.8710

Table 3.3 Influence of α_x, α_y and α_z

m=6			
α_x, α_y, α_z	c_1	c_2	c_3
0.5	1.1050	1.1398	1.1100
1	0.9844	1.0154	0.9889
1.5	0.9201	0.9491	0.9243
2	0.8770	0.9046	0.8810

The final calculations in this series was to set $\alpha_x = \alpha_y = \alpha_z = 1$ and vary the value of the exponent m from 1 to 14. Figure 3.8 shows the resulting yield loci, which vary from an elliptical shape to a locus which resembles the Tresca yield criterion. The corresponding c values are listed in Table 3.4.

To assess the influence of the α values on the r-values it was decided to calculate the in-plane variation of r from the rolling direction (r_0) to the transverse direction (r_{90}). The same pseudo-experimental data, as given in Table 3.1, were employed but now an additional parameter is required, namely the yield shear stress of the material $(\sigma_{xy})_Y$. As described in Section 3.2.2 a knowledge of $(\sigma_{xy})_Y$ will enable the coefficient c_6 to be determined which is necessary for evaluating the r values. Previous calculations, see Section 3.2.2 and Appendix B, had led to the evaluation of r_{45} and a value for the ratio

$(\sigma_{xy})_Y/\bar{\sigma} = 0.5352$. The same stress ratio was used in the current calculations where the r-values were calculated at 1° intervals. In all the calculations, m was chosen to be 6 and the α values were varied. Initially $\alpha_y = \alpha_z = 1$ was chosen and α_x was varied from 0 to 2 in steps of 0.5. The corresponding variations in r are plotted in Fig. 3.9, while Table 3.5 shows the calculated c values and the value of r at 0, 45 and 90 degrees to the rolling direction. Only when $\alpha_x = 0$ is there any dramatic change in the r-value which occurs at r_{90}. The calculations were repeated with $\alpha_x = \alpha_z = 1$ and varying α_y from 0 to 2 in steps of 0.5. Figure 3.10 plots the variation in the r-values. The figure is very similar to the preceding diagram, Fig 3.9, but a dramatic increase now occurs at r_0 (rather than r_{90}) when $\alpha_y = 0$. Table 3.6 shows the calculated c values and the r-values at 0, 45 and 90 degrees. The final calculations were performed with $\alpha_x = \alpha_y = 1$ and α_z varying from 0 to 2 in 0.5 increments. The variation in the r-value is shown in Fig. 3.11, and it can be seen that there is a general increase in r at all orientations as α_z decreases, which suggests that as α_z decreases the through thickness strength of the material decreases. As before Table 3.7 shows the variation in the c values and selected r-values.

Table 3.4 Influence of m

$\alpha_x=\alpha_y=\alpha_z=1$			
m	c_1	c_2	c_3
1	0.9845	1.0155	0.9889
2	0.9845	1.0155	0.9889
3	0.9845	1.0155	0.9889
4	0.9845	1.0155	0.9889
6	0.9845	1.0155	0.9889
8	0.9845	1.0155	0.9889
10	0.9845	1.0155	0.9889
12	0.9845	1.0155	0.9889
14	0.9845	1.0155	0.9889

Table 3.5 Influence of α_x

m=6, α_y=α_z=1							
α_x	c_1	c_2	c_3	c_6	r_0	r_{45}	r_{90}
0	1.3406	1.0134	0.9909	1.0460	0.9341	1.3126	9.1529
0.5	1.0910	1.0150	0.9893	1.0446	0.9316	1.2970	1.5217
1	0.9844	1.0154	0.9889	1.0433	0.9323	1.1805	1.0122
1.5	0.9166	1.0156	0.9887	1.0420	0.9334	1.0801	0.8063
2	0.8672	1.0156	0.9887	1.0407	0.9345	0.9989	0.6902

Table 3.6 Influence of α_y

m=6, α_x=α_z=1							
α_y	c_1	c_2	c_3	c_6	r_0	r_{45}	r_{90}
0	0.9848	1.3978	0.9885	1.0460	7.1706	1.2590	1.0118
0.5	0.9845	1.1271	0.9888	1.0446	1.3750	1.2860	1.0124
1	0.9844	1.0154	0.9889	1.0433	0.9323	1.1805	1.0122
1.5	0.9844	0.9450	0.9889	1.0420	0.7501	1.0851	1.0120
2	0.9844	0.8939	0.9889	1.0407	0.6463	1.0065	1.0118

Table 3.7 Influence of α_z

m=6, α_x=α_y=1							
α_z	c_1	c_2	c_3	c_6	r_0	r_{45}	r_{90}
0	0.9869	1.0130	1.3487	1.8685	0.1201	0.4391	0.1124
0.5	0.9849	1.0149	1.0962	1.1653	0.6324	0.9244	0.6733
1	0.9844	1.0154	0.9889	1.0433	0.9323	1.1805	1.0122
1.5	0.9843	1.0156	0.9207	0.9768	1.1573	1.3697	1.2711
2	0.9842	1.0157	0.8710	0.9319	1.3411	1.5235	1.4852

Chapter 4

Experiments and Results

4.1 Material

The material selected for this present study was a cold rolled, ultra-low carbon, Nb treated, interstitial-free (IF) sheet steel. The steel was cold rolled in a commercial 5 stand, 4 high mill located at Dofasco Incorporated, Hamilton, Ontario. The author had the rare opportunity of be able to stop the mill during production and to cut out samples at entry and exit to the mill and also between each stand. Hence six sets of samples were collected and subjected to the tests described in this and subsequent chapters. The chemical composition of the steel sheet is given in Table 4.1 and the thickness, t, of each sample and its associated reduction ratio, R, and rolling strain, ε_r, is given in Table 4.2.

Table 4.1 The Chemical Composition of the Ultra-low Carbon Steel

Element	Weight %
C	0.0026
P	0.0072
S	0.0074
Si	0.0082
N	0.0040
Nb	0.0075
Al	0.0500
Ti	0.0500
Mn	0.1500

Table 4.2 Sample Thickness, and the Reduction and the Rolling Strain after each Roll Pass

Stage	Thickness t (mm)	Reduction R (%)	Total Reduction R_T (%)	Strain ε_r (%)	Total Strain ε_T (%)
0	3.815				
1	2.733	28.36	28.36	33.35	33.35
2	1.412	48.34	76.70	66.04	99.39
3	1.125	20.33	97.03	22.72	122.11
4	1.099	2.31	99.34	2.34	124.45
5	0.833	24.20	123.54	27.71	152.16

4.2 Tensile Tests

A tensile test is one of the simplest mechanical tests to evaluate the formability of materials. The behaviour of the material in the plastic range of a true stress-strain curve can be described by the following empirical power law expression

$$\sigma = K \varepsilon^n$$

where K and n are material parameters and n is the so-called strain-hardening index.

In the present work, all tensile tests were conducted on a MTS series 810 universal testing machine and an extensometer was attached to the gauge length of each specimen during each test. The load-displacement data were collected, via a data acquisition system, as voltage signals and an associated software package converted the signals to true stress-true strain data. Owing to the limited amount of material available tensile specimens were prepared along the rolling direction only. The samples were produced according to the ASTM, E10 specification, as shown in Fig. 4.1. Three specimens of each stage were tested and the averages of their results are listed in Table 4.3. For steels, the percentage error of the measured yield stress is typical less than 8 % [102]. The true stress-true strain curves for the samples of ultra-low carbon steel at each of the different stages of reduction are shown in Figs. 4.2 to 4.7.

As seen from the true stress-true strain tensile test in Fig. 4.3 the ductility of the material is essentially exhausted after passing through the first roll stand. Therefore, the individual tensile tests reveal nothing about the plastic behaviour of the material after stands one through five however, the current yield stress can be monitored and this is listed in Table 4.3. The yield stress as a function of accumulated plastic strain (see the final column in Table 4.2) is plotted in Fig. 4.8. From these results it is possible to generate a pseudo stress-strain curve and fit this with the empirical relationship

$$\sigma = K \varepsilon^n.$$

The estimated stress-strain curve is shown in Fig. 4.8 and the value of K was calculated as 568 MPa with n = 0.21. These values are comparable with the K and n values calculated for the as-received material, see Table 4.3.

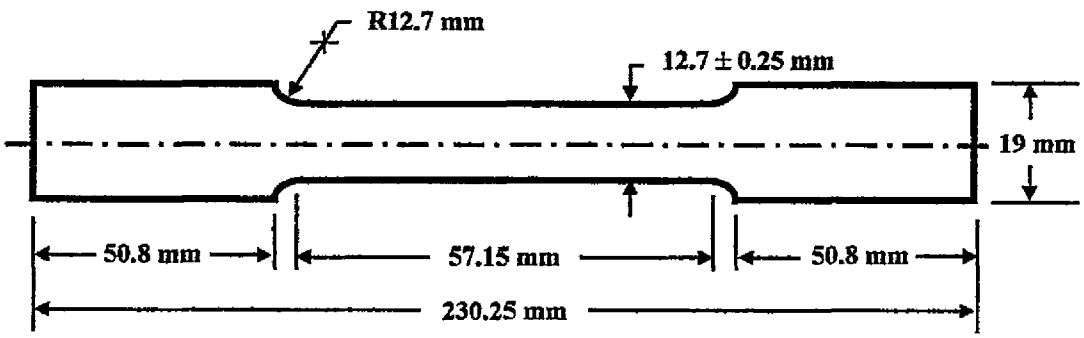

Figure 4.1 An ASTM Standard E10 Strip Tensile Specimen

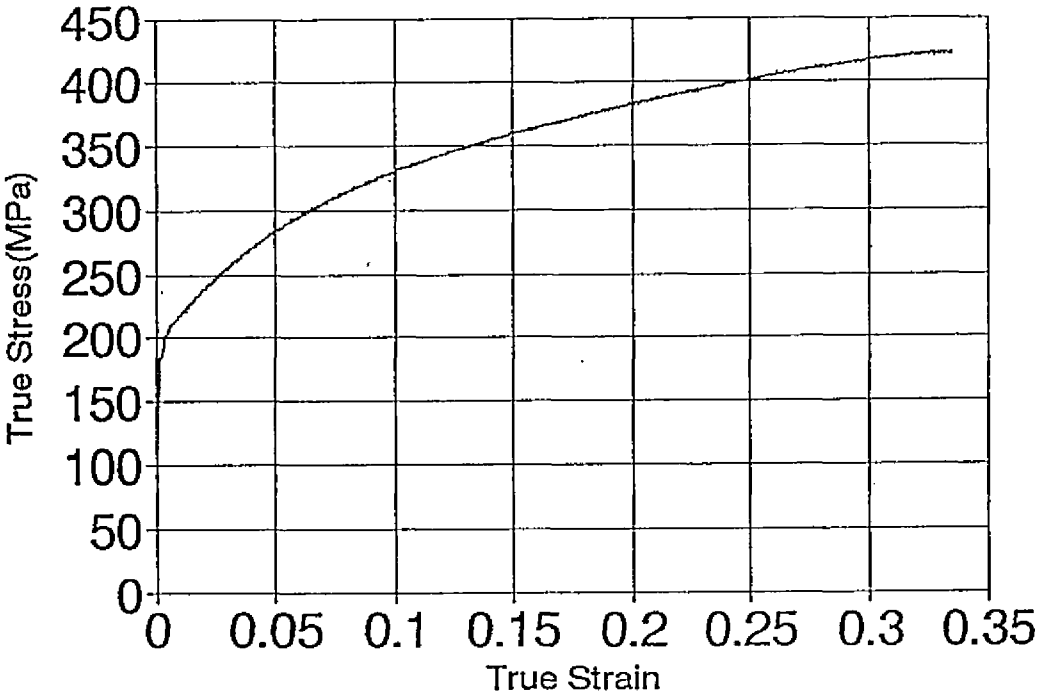

Figure 4.2 The True Stress-Strain Curve for the Material at Entry

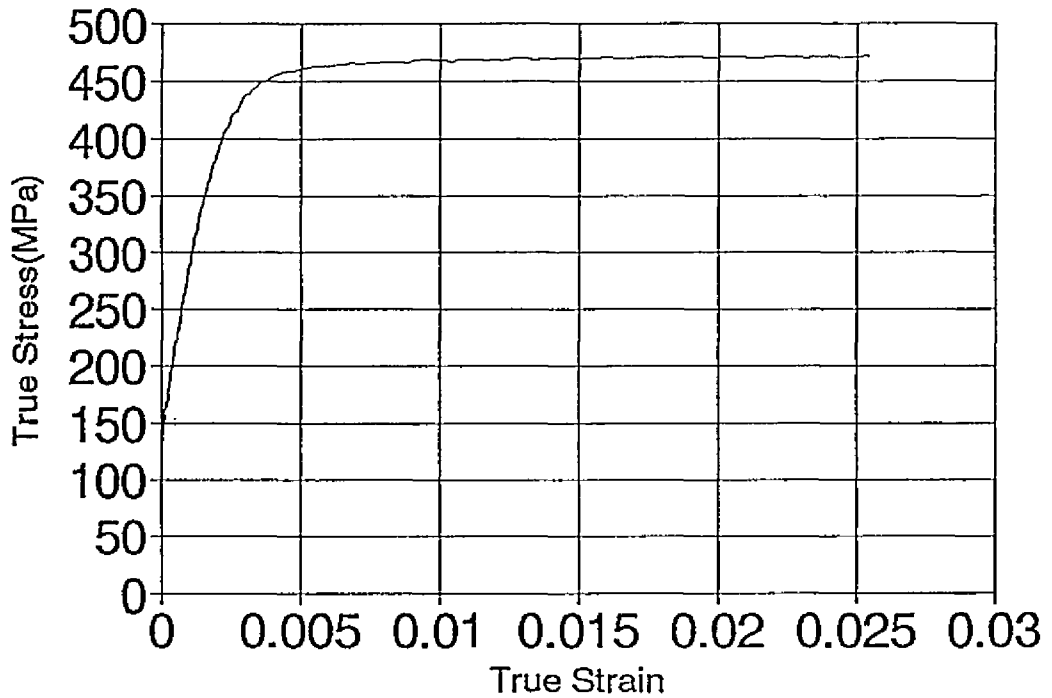

Figure 4.3 The True Stress-Strain Curve for the Stage One Sample

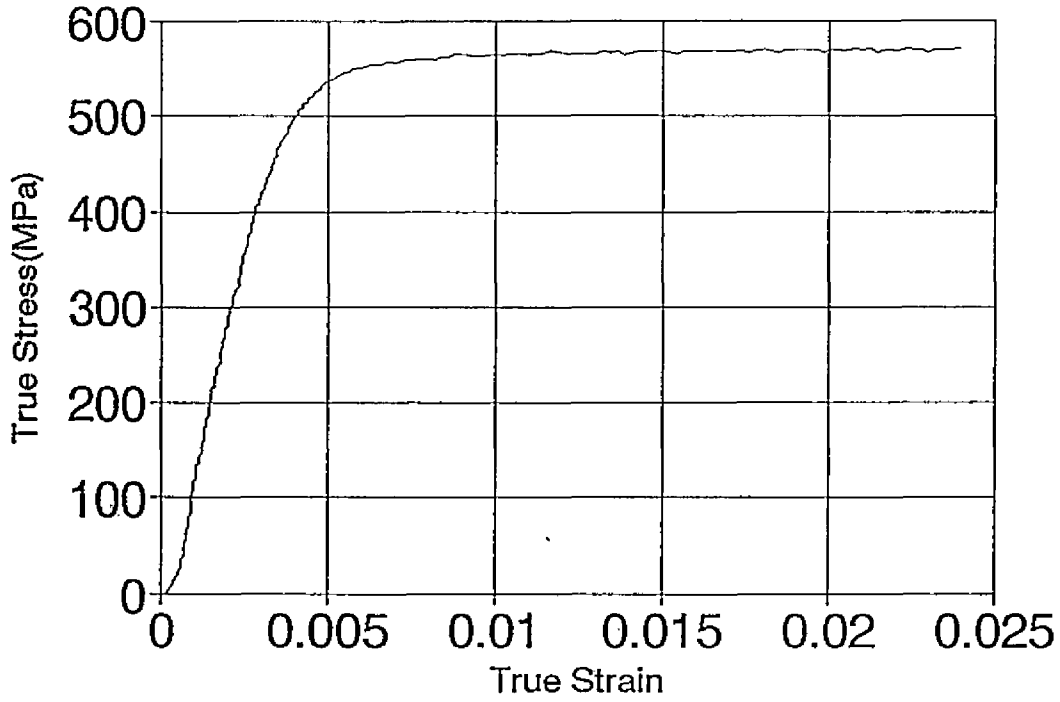

Figure 4.4 The True Stress-Strain Curve for the Stage Two Sample

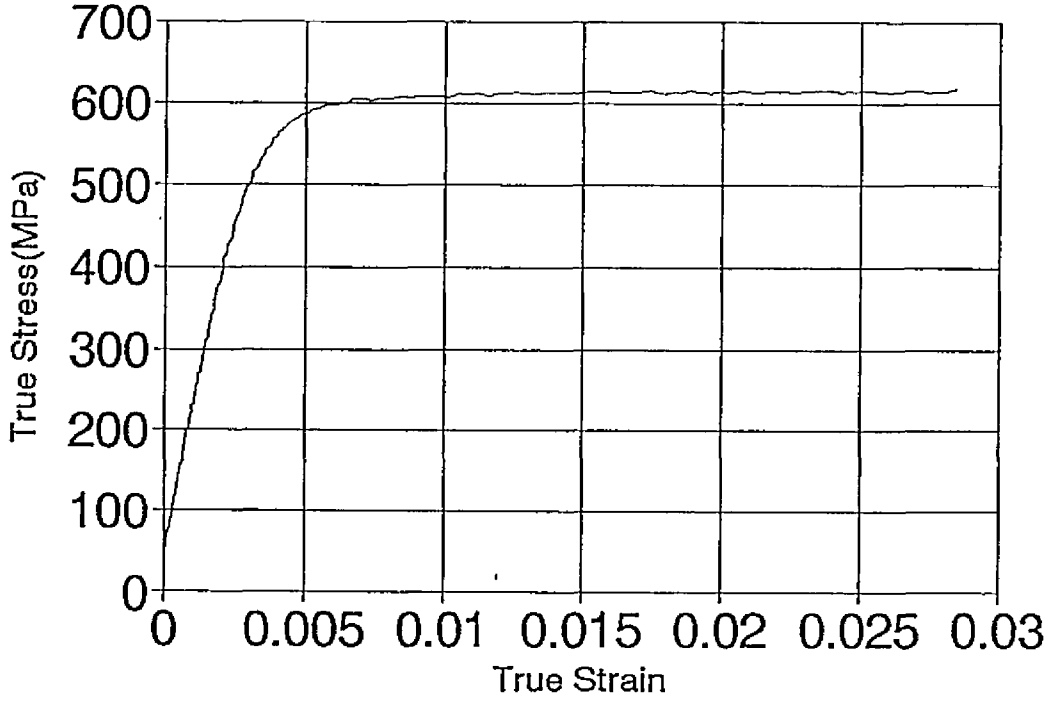

Figure 4.5 The True Stress-Strain Curve for the Stage Three Sample

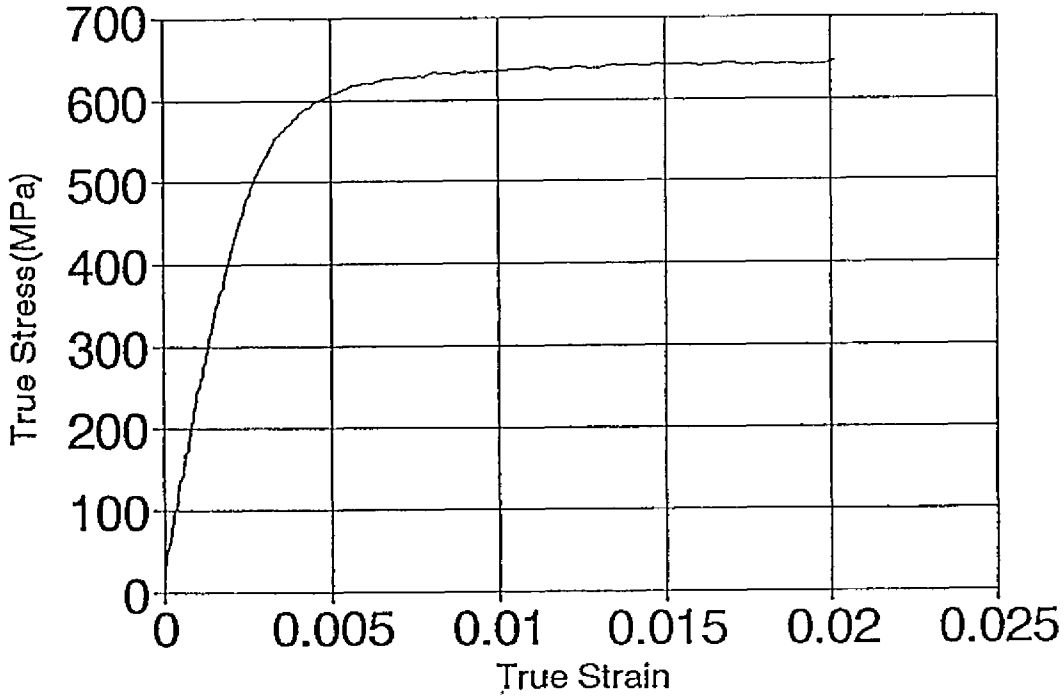

Figure 4.6 The True Stress-Strain Curve for the Stage Four Sample

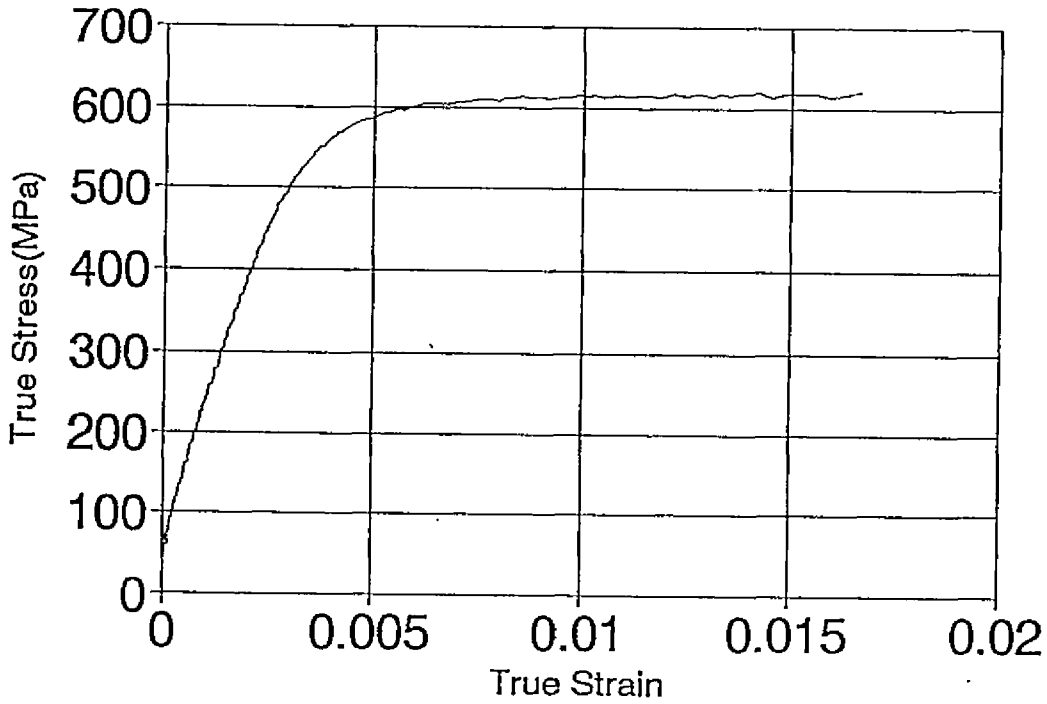

Figure 4.7 The True Stress-Strain Curve for the Material at Exit

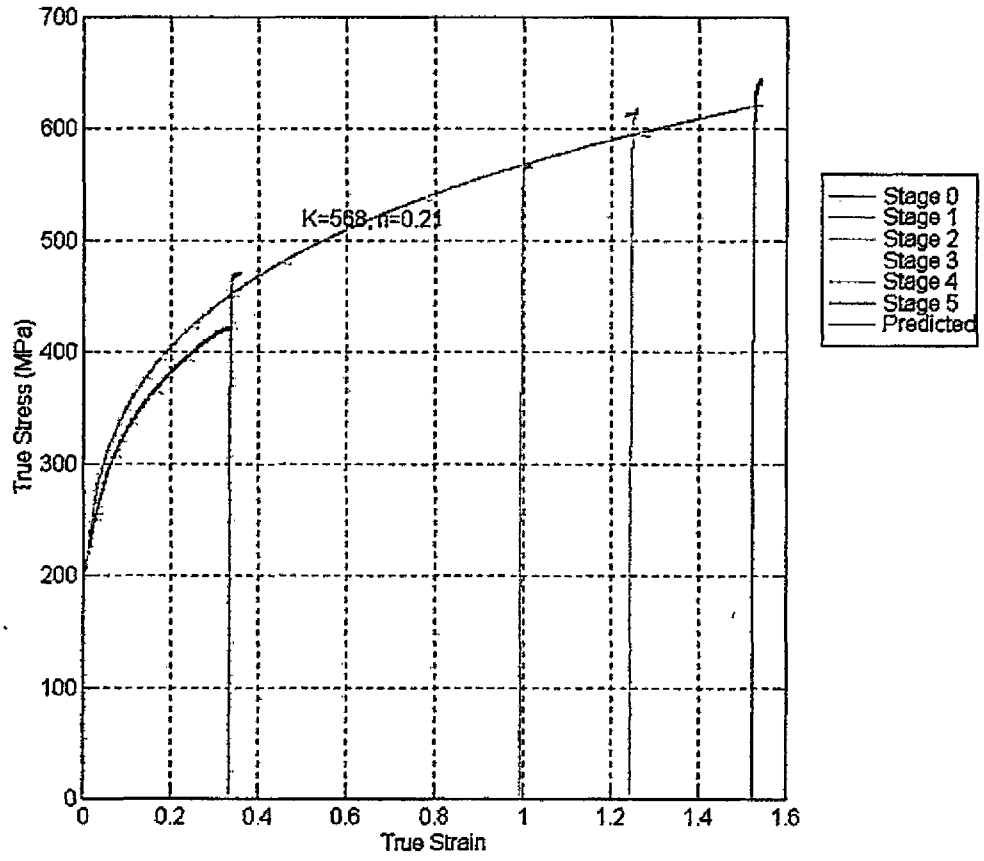

Figure 4.8 Experimental and Predicted True Stress-Strain Curve

Table 4.3 Mechanical Properties of the Ultra-low Carbon Steel at Rolling Direction

Stage	Yield Stress (MPa)	Ultimate Tensile Stress (MPa)	Y.S./U.T.S Ratio	Strain at U.T.S Ratio	n value	K value	r value
0	217.380	314.085	0.693	0.220	0.216	542.0	0.95
1	462.242						
2	543.233						
3	596.030						
4	600.740						
5	619.062						

4.3 r-value Tests

A qualitative measure of material anisotropy can be obtained from the plastic strain ratio or r-value. The r-value is defined as the ratio of true width strain, ε_w, to true thickness strain, ε_t, at some specified axial strain in a tensile test i.e.

$$r_\theta = \frac{\varepsilon_w}{\varepsilon_t}$$

Under normal circumstances tensile specimens would be cut from the plane of a rolled sheet at a different orientation, θ, with respect to the rolling direction. For a perfectly isotropic material the r-value would be unity and independent of θ. See Refs [27-28] for a more detailed discussion.

However, as already mentioned, the author had a limited amount of material available to him, such that tensile specimens were prepared in the rolling direction only. Furthermore, as discussed above, the material was severely cold worked after passing through the first roll stand and therefore it was not possible to achieve any meaningful axial strain in a tensile test before fracture of the specimen occurred. Consequently, only for the as-received material could a r-value be determined, see Table 4.3.

As described in Chapter 5, it is possible to predict r_θ once the Crystallite Orientation Distribution Function (CODF) for each material sample is known.

4.4 Microhardness Tests

Another test to depict the variation of a mechanical property as a function of reduction in cold rolling is the hardness test. In the present study it was decided to take

the hardness impressions on a face perpendicular to the thickness direction. Since the thickness of the different samples varied from about 3.8mm to 0.83mm it was considered that a microhardness impression would minimize the risk of the plastic zone (surrounding the impression) spreading to the top and bottom surfaces of the specimen. The samples were mounted in a plastic casing, see Fig. 4.9, and the surface ground and polished before performing the indentation tests. A NMT-3 microhardness tester, equipped with a Vickers type indentor, was used to evaluate the hardness. In general, the impressions were made across the thickness of sample starting near one surface and spaced at 0.1 to 0.2mm intervals as shown in Fig. 4.10(a). An enlarged view of the impressions is shown in Fig. 4.10(b). The results of the hardness tests are listed in the Table 4.4 and plotted in Fig. 4.11. As can be seen there is considerable scatter in the results. The author believes this is a feature of inconsistent experimental technique rather than inhomogeneous plastic deformation within the specimen, see Section 4.5. However, on average, the hardness increases with increasing reduction as shown in Table 4.5 and Fig 4.12. Empirical relationships can be used to relate the hardness, h, with the current thickness, t, of the sample. Four such relationships are given below [28]

$$h = a - b \ln t$$
$$h = a \exp(-bt)$$
$$h = t / \ln(a + t/b)$$
$$h = at^{-b},$$

in the above a and b are constants.

As shown in Fig. 4.13 each of the above relationships can be used to fit the experimental data. In the present case, the third expression provides the best fit.

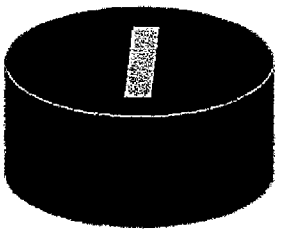

Figure 4.9 A Mounted Specimen for Microhardness Tests

Some preliminary annealing experiments were performed on steel samples after exiting the mill. Six samples were used and five of these were cleaned and coated with a protective firm before continuously annealing in an automatically controlled furnace. The annealing temperature employed were 680, 730, 760, 790 and 850 degrees Celsius. The microstructure of the samples was observed under an optical microscope and the results are shown in Fig. 4.14. Increasing recrystallization is observed with increasing annealing temperature. There is a corresponding reduction in the microhardness with increasing annealing temperature as shown in Fig. 4.15.

4.5 A Preliminary Study of Inhomogeneous Deformation during Cold Rolling

An attempt was used to assess the degree of inhomogeneous deformation in the cold rolled sheet using optical and scanning electron microscopy. Slip bands and shear bands i.e. a macroscopic localization of intense shear, have often been observed in metals subjected to large deformation processes such as forging and rolling. Figure 4.16 is a schematic representation of shear bands formed during cold rolling. Figure 4.17 shows the distinction between a coarse slip band and a macroscopic shear band, which appeared

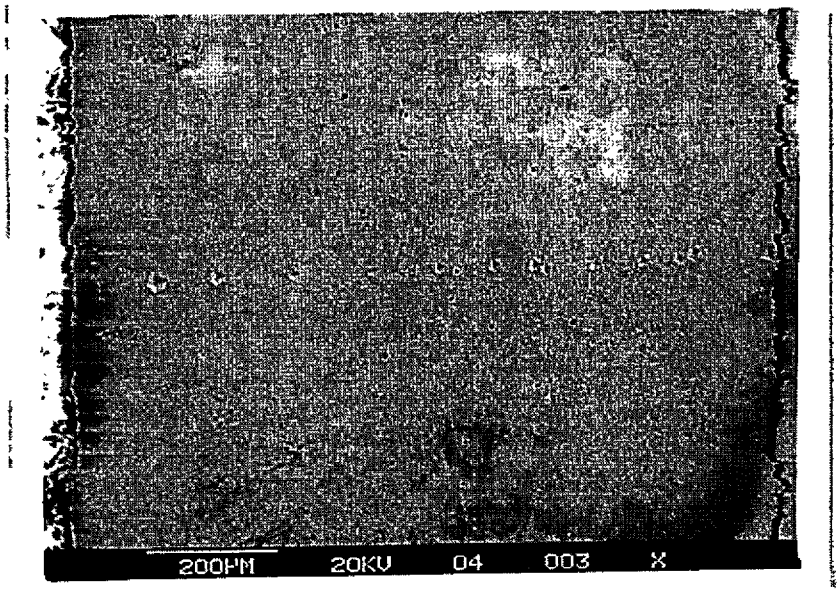

(a)

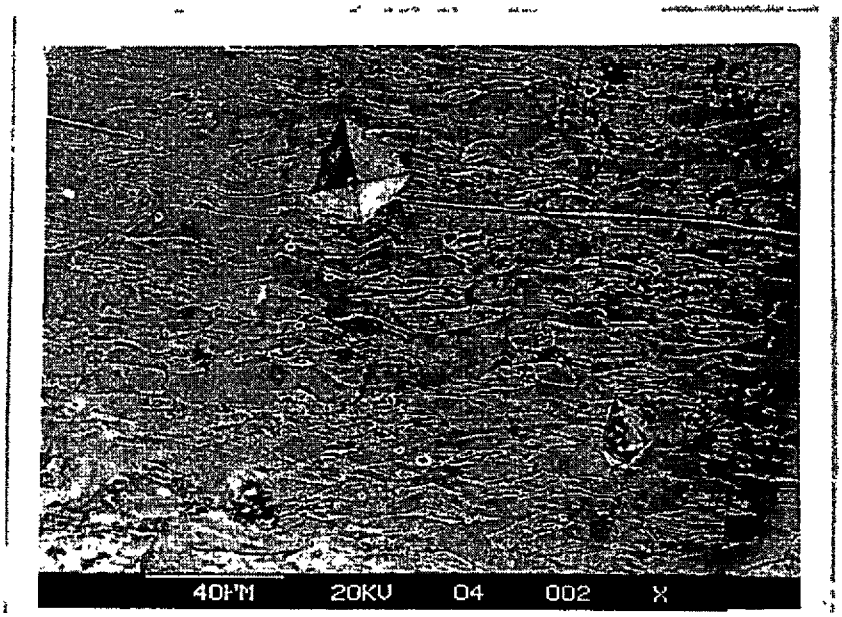

(b)

Figure 4.10 The Stage Five Sample after Indentation

Table 4.4 Hardness for Ultra-low Carbon Steel at Different Stages

Stage 0														
No.	1	2	3	4	5	6	7	8	9	10	11	12	13	14
Distance (mm)	0.1	0.2	0.3	0.3	0.5	0.6	0.7	0.8	0.9	1.1	1.2	1.3	1.5	1.6
Hardness (kg/mm^2)	97	102	102	102	104	91	127	125	99	102	89	110	99	102

Stage 0														
No.	15	16	17	18	19	20	21	22	23	24	25	26	27	28
Distance (mm)	1.7	1.9	2.0	2.2	2.3	2.4	2.6	2.7	2.8	3	3.1	3.3	3.5	3.7
Hardness (kg/mm^2)	118	99	100	86	99	94	93	121	69	129	67	100	88	76

Stage 1										
No.	1	2	3	4	5	6	7	8	9	10
Distance (mm)	0.1	0.2	0.5	0.8	1.1	1.4	1.7	2.0	2.3	2.6
Hardness (kg/mm^2)	136	132	136	142	129	132	136	142	106	132

Stage 2											
No.	1	2	3	4	5	6	7	8	9	10	11
Distance (mm)	0.0	0.2	0.3	0.4	0.6	0.7	0.8	1.0	1.1	1.2	1.3
Hardness (kg/mm^2)	58	75	172	166	161	161	161	184	161	184	129

Stage 3								
No.	1	2	3	4	5	6	7	8
Distance (mm)	0.1	0.2	0.4	0.5	0.7	0.9	1.0	1.0
Hardness (kg/mm^2)	184	118	142	142	156	170	172	178

Stage 4												
No.	1	2	3	4	5	6	7	8	9	10	11	12
Distance (mm)	0.0	0.2	0.2	0.3	0.4	0.4	0.5	0.6	0.8	0.9	1.0	1.0
Hardness (kg/mm^2)	118	184	199	190	172	172	199	184	172	84	60	233

Stage 5											
No.	1	2	3	4	5	6	7	8	9	10	11
Distance (mm)	0.1	0.2	0.2	0.3	0.4	0.5	0.5	0.6	0.7	0.8	0.8
Hardness (kg/mm^2)	207	199	190	190	217	207	232	184	223	207	190

Table 4.5 Thickness and Hardness for All Stages

Stage	Thickness t (mm)	Average of Hardness h (kg/mm^2)	Range of Hardness (kg/mm^2)
0	3.815	99.6	67.1-129.0
1	2.733	132.3	106.0-136.0
2	1.412	146.5	57.9-184.0
3	1.125	157.8	118.0-184.0
4	1.099	163.9	60.2-223.0
5	0.833	204.2	184.0-232.0

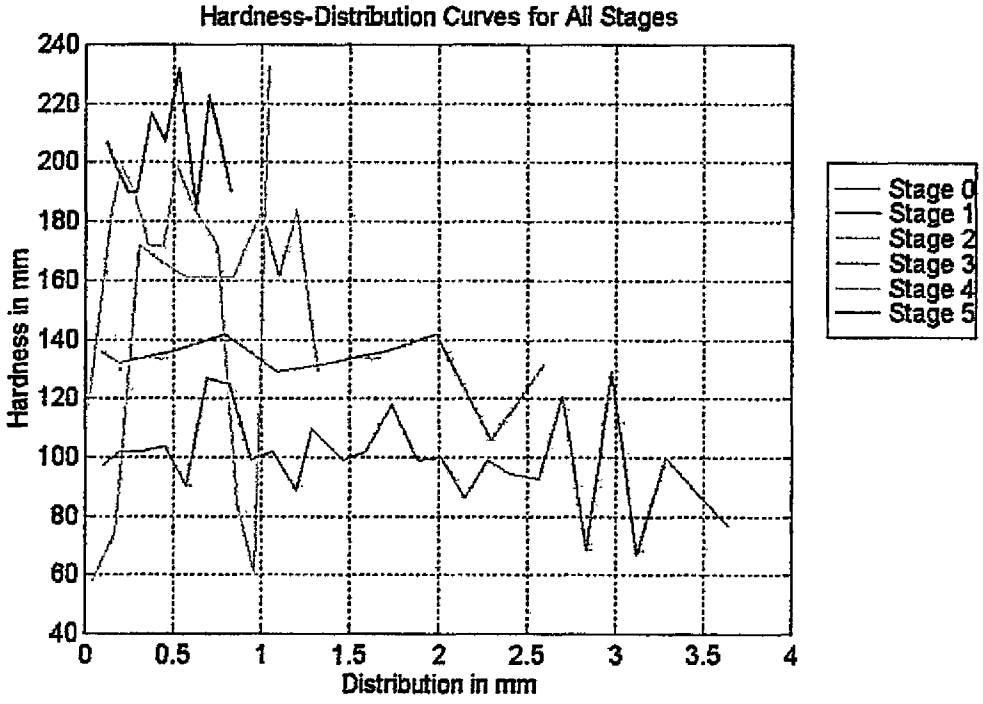

Figure 4.11 The Hardness-Distance from Surface Curves for All Stages

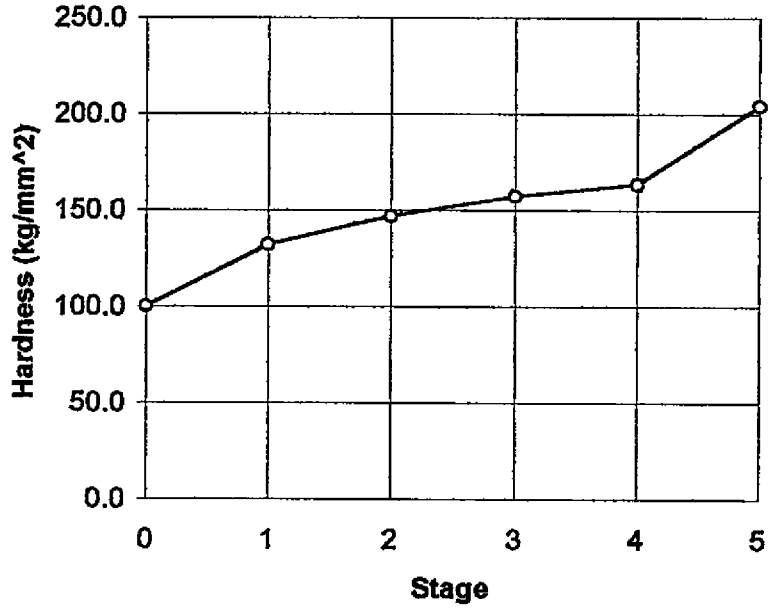

Figure 4.12 Average Hardness in Each Stage

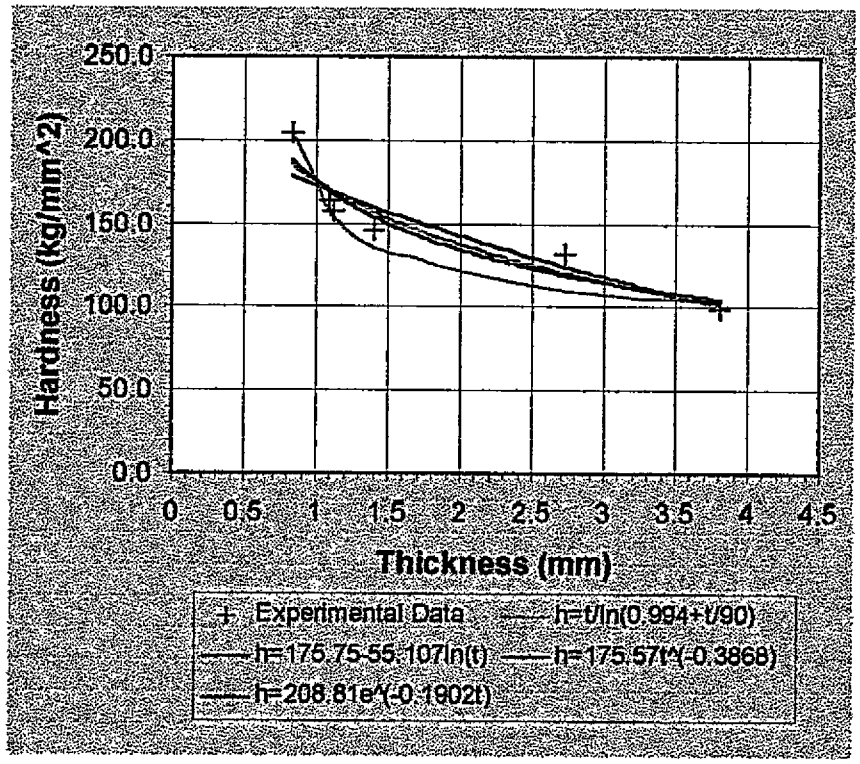

Figure 4.13 The Experimental Data and Empirical Hardness-Thickness Curves

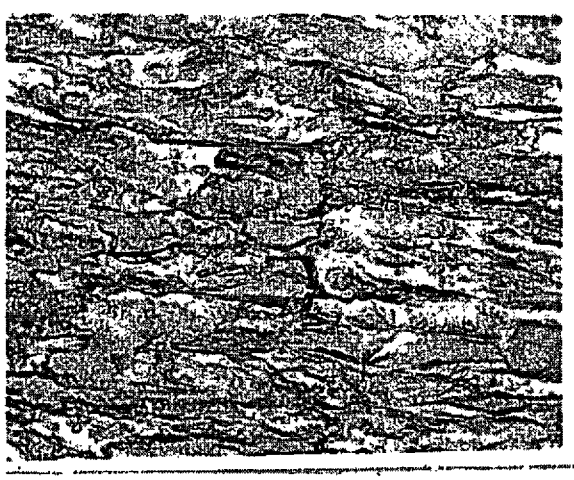

Microstructure at 20°C (200X)

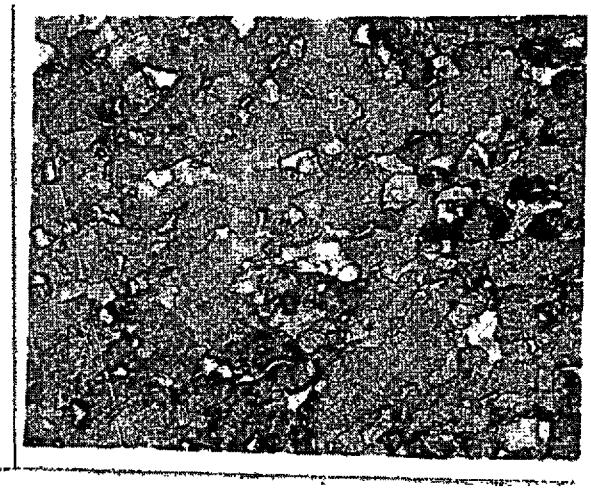

Microstructure at 680°C (200X)

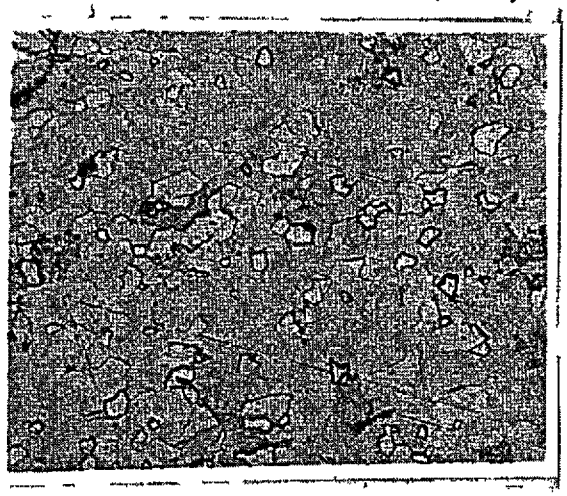

Microstructure at 730°C (200X)

Microstructure at 760°C (200X)

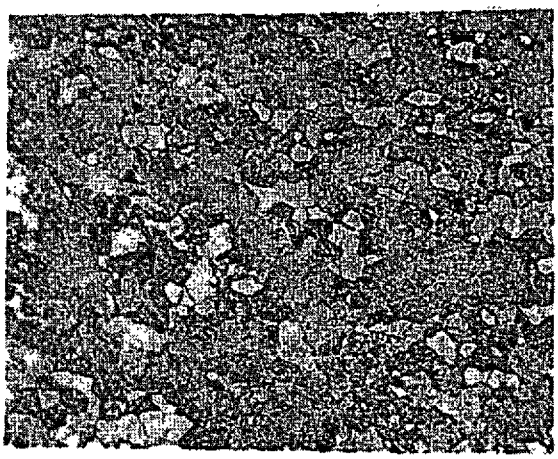

Microstructure at 790°C (200X)

Microstructure at 850°C (200X)

Figure 4.14 The Microstructures of the Cold Rolled Steel at Different Temperatures

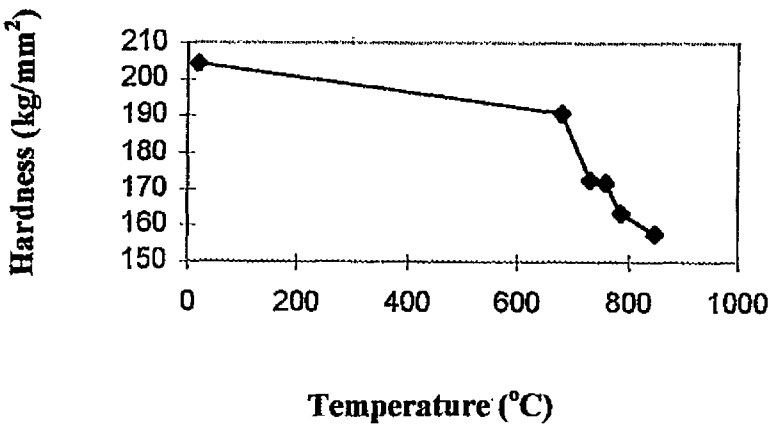

Figure 4.15 The Hardness-Temperature Curve for the Cold Rolled Steel

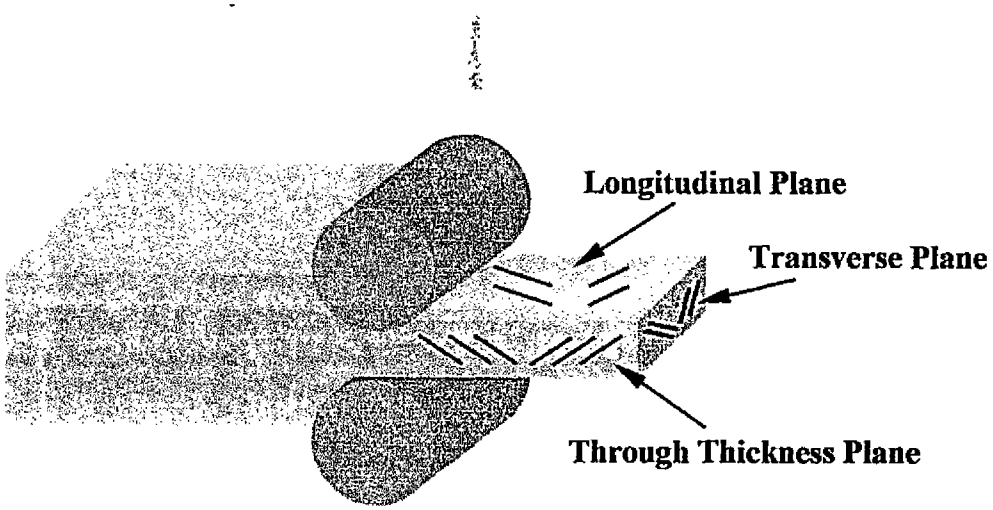

Figure 4.16 Shear Bands during Rolling

during a tensile test on an aluminum-copper alloy. Figure 4.17 was taken from Ref [77], and it can be seen that the macroscopic shear band is not aligned with the coarse slip bands. No clear explanation for this was given in the article and the authors claimed the phenomenon was not well understood. It is beyond the scope of this thesis to provide an in-depth study of shear banding, the interested reader will find additional information on the topic in Refs. 78 to 81.

Figure 4.18 is a photomicrograph of the structure of the as-received material, showing equi-axed grains. The material is relatively pure and the main inclusions tend to be Al_2O_3 and TiN, these are not visible in Fig. 4.18 but can be seen in Figs. 4.19 to 4.20 taken in the scanning electron microscope. After passing through the cold mill the material is heavily deformed and due to inhomogeneous deformation around the inclusions they could become detached from the matrix. Preparing the samples for optical and electron microscopy examination may further loosen the inclusion. The photograph shown in Fig. 4.21 was taken in the electron microscope and shows a number of voids, the material was fully cold rolled having been passed through the fifth (exit) stand of the mill.

No macroscopic shear bands were observed, although it was anticipated that these would be present. Coarse slip bands were observed and their numbers increased with increasing deformation, this is evident from Figs. 4.22 to 4.24.

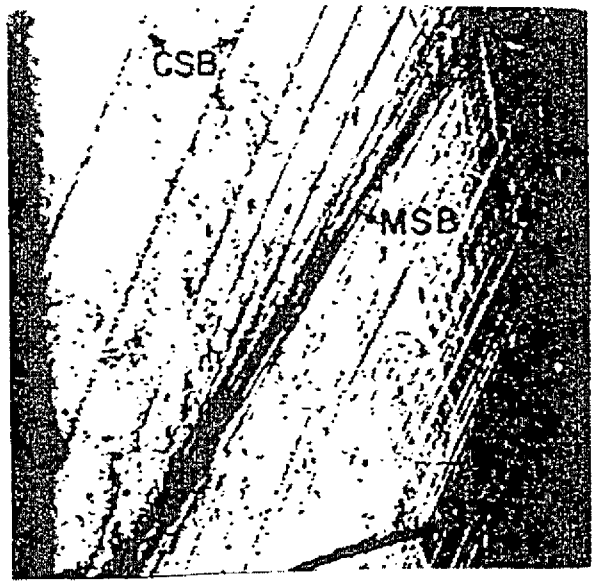

Figure 4.17 Coarse Slip Bands (CSB) and Macroscopic Slip Band (from Chang and Asaro, 1981)

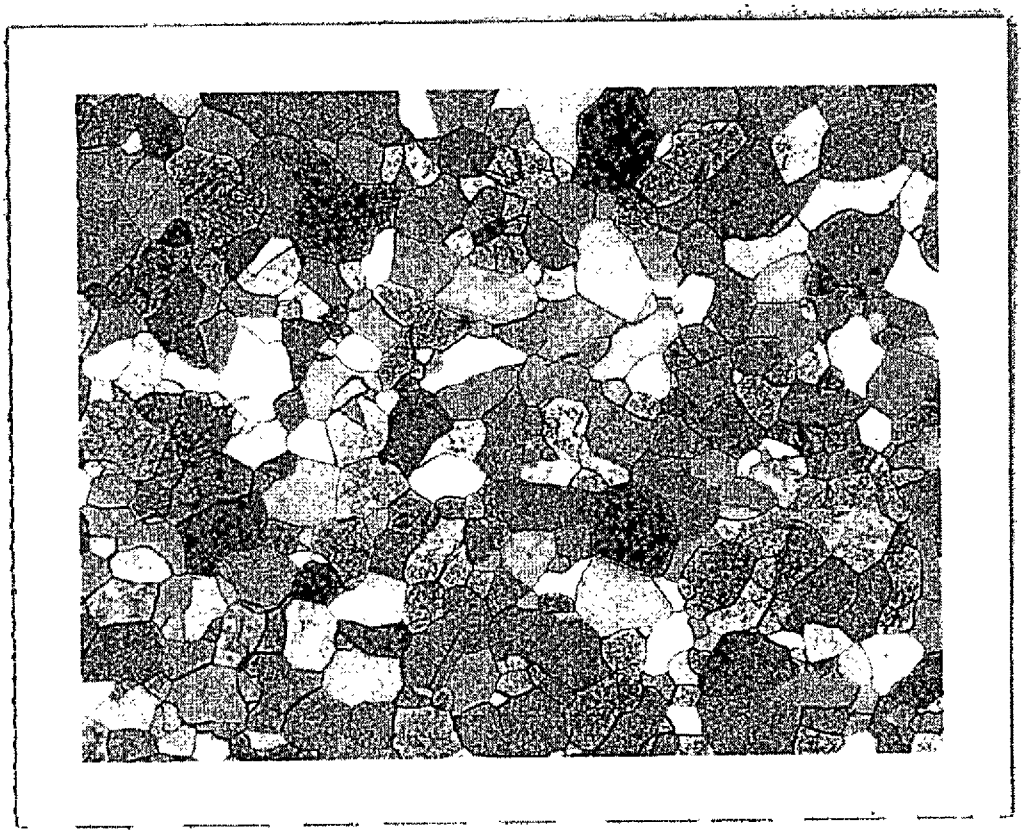

Figure 4.18 The Stage Zero Sample with the Equi-cored Grains in the Longitudinal Plane

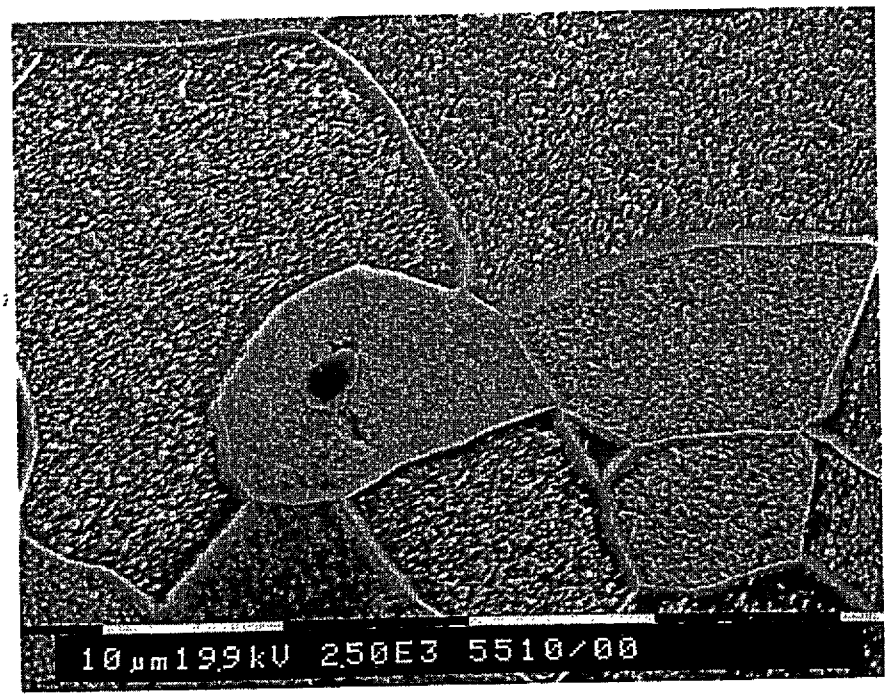

Figure 4.19 An Al_2O_3 Inclusion in the Longitudinal Plane

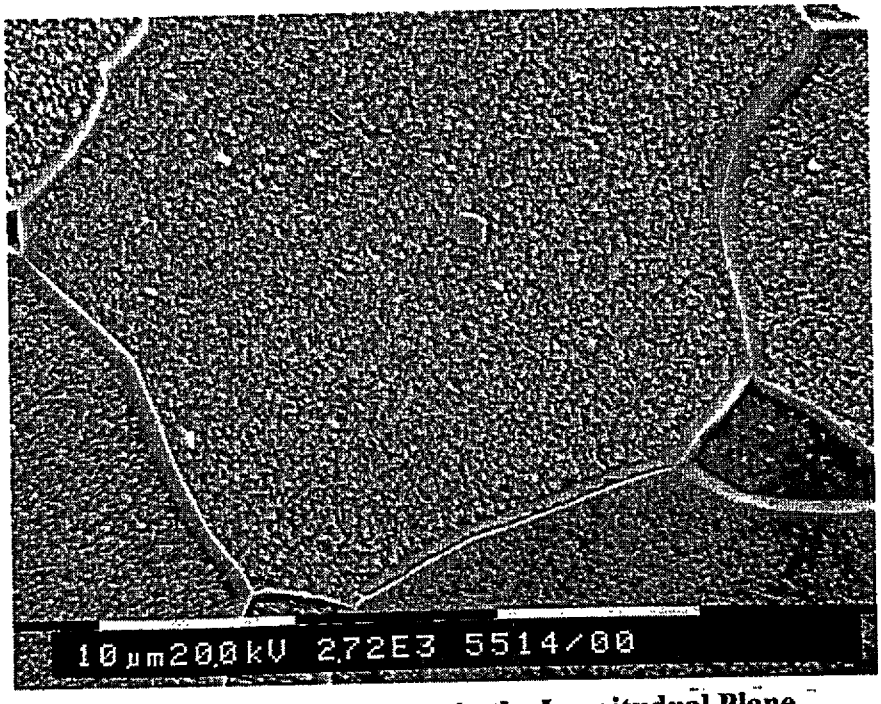

Figure 4.20 A TiN Inclusion in the Longitudual Plane

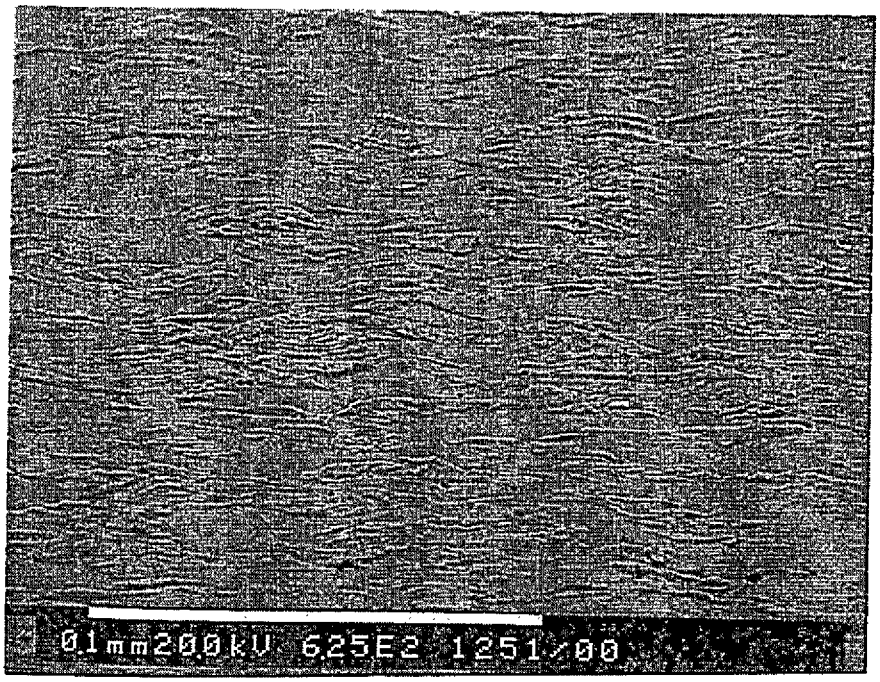

Figure 4.21 Voids in the Transverse Plane, Stage 5 Sample

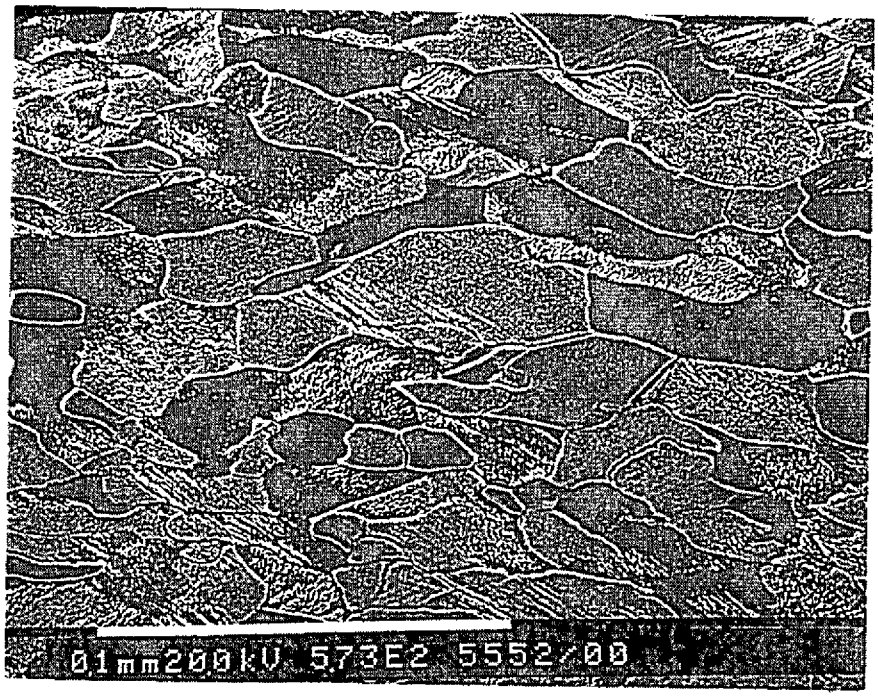

Figure 4.22 Slip Bands in the Through-Thickness Plane of the Stage One Sample

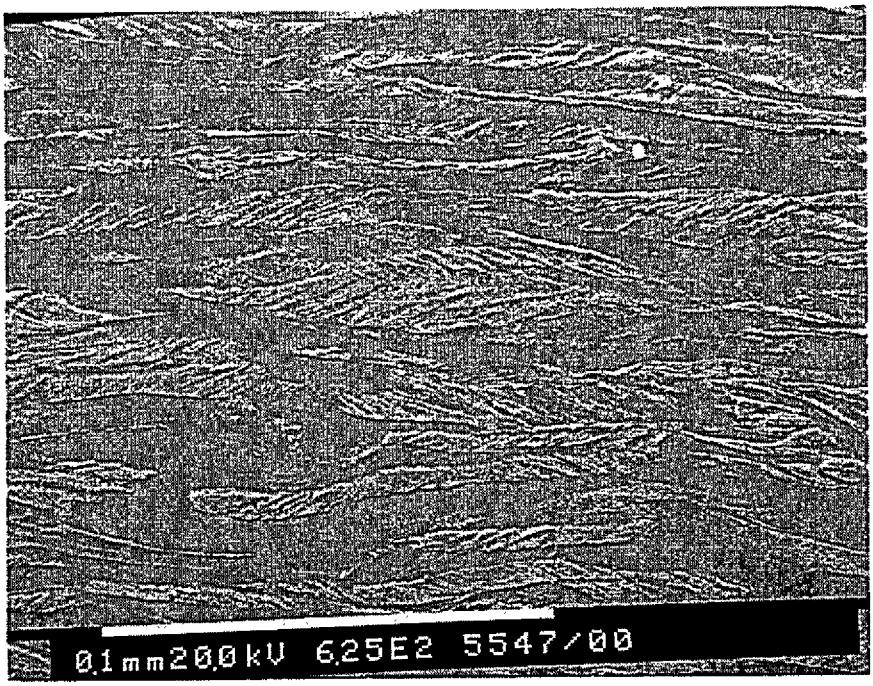

Figure 4.23 Slip Bands in the Through-thickness Plane of the Stage Three Sample

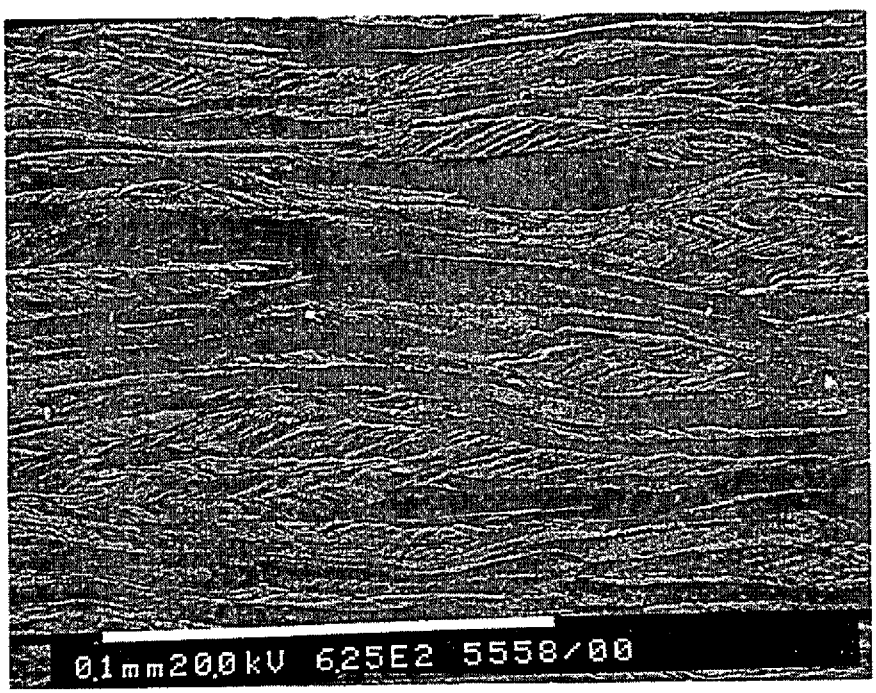

Figure 4.24 Slip Bands in the Through-thickness Plane of the Stage Five Sample

Chapter 5

Comparison of Pole Figures and Their Corresponding Yield Loci

5.1 Introduction

In Chapter 2, a selected review of texture measurement techniques, pole figures and Taylor-Bishop-Hill models has been presented, while Chapter 3 describes the mathematical development of Barlat's 94 yield criterion. Among other things, Chapter 4 gives the results of the tensile tests on samples cut from the cold rolled sheet in order to determine the r-values. As also mentioned in Chapter 4, the sheet was reduced in 5 successive stands in the Dofasco cold mill. However, the tensile ductility of the sheet was exhausted after the first pass and therefore the r-value for the *as received* material only could be determined.

The data obtained in Chapters 2 to 4 were used to ascertain the pole figures of the samples and their corresponding yield loci. Some of these results are presented in this chapter. The pole figures were determined from two different sources namely, Queen's University, Kingston, Ontario and Los Alamos National Laboratory in New Mexico. For texture analysis, samples between each roll stand were sent to the Los Alamos Laboratory while only the as-received sample was dispatched to Queen's University. The Los Alamos Laboratory supplied experimental pole figures, obtained by direct measurement on each of the samples. A Scintag Five Axis Pole Figure Goniometer similar to the one shown in Fig. 5.1 was employed to generate the pole figures. By contrast the researchers

at Queen's University measured only the pole figure for the as received sample, the remaining pole figures were predicted. The technique was to generate a Crystallite Orientation Distribution Function (CODF) from the pole figures taken on the *as received* sample. The cold rolling schedule was discretized into a number of small but finite steps. With the aid of a computer software package the texture evolution could be predicted i.e. a new CODF, after each reduction step. Once having the CODF it is then possible to convert this back to generate a new pole figure. A knowledge of the CODF enables a prediction of the corresponding crystallographic yield locus using Van Houtte's fully constrained (FC) Taylor model [37]. In addition r-values can also be predicted.

As already mentioned only the r-values for the *as received* material could be determined from mechanical tests. It so happened that the measured r-value was close to that predicted from the analysis performed at Queen's University, see tables 4.3 and 6.3. As discussed in Chapter 3 some r-values are required in order to calculate Barlat's 94-yield function, and the values presented by Queen's were used in this study.

It should be noted that the present author has little knowledge of pole figures and CODF's, and the computer software that links them. I have been guided by the researchers both at Queen's University and Los Alamos to obtain a very rudimentary understanding of the procedures involved.

5.2 Texture Measurement for and A Comparison of Pole Figures

5.2.1 Introduction

As mentioned in Chapter 2, a pole figure is a stereographic projection, which shows the variation in density of a plane normal (or pole) with orientation, for a selected set of crystallographic planes. Intensities are plotted as multiples of the intensity expected from a randomly oriented specimen. One disadvantage of the pole figure is that it gives information only about the distribution of the plane normals and does not contain information about the rotation around the normals. It is for this reason that CODFs have been employed to provide a more complete description of the texture.

In this section, the two sets of pole figures developed by Los Alamos National Laboratory and Queen's University for the cold rolled, ultra-low carbon steel samples are compared. The experimental procedure of texture measurement at the Los Alamos National Laboratory is also briefly described. As mentioned earlier, Dofasco provided all the samples and these were ground down to their mid-planes in the thickness direction before performing the experiments.

5.2.2 Texture Measurement and the Resulting Pole Figures

5.2.2.1 Textures Measured at Los Alamos

All the samples provided from Dofasco were first ground to their mid-planes by 320 sand grinding at McMaster University and then sent to the Department of Material Science and Technology at the Los Alamos National Laboratory for texture measurement. Before measurement, the samples were further polished. This was to eliminate any unseen surface damage on the mid-planes. A Scintage Five Axis Pole

Figure Goniometer was then used to examine the polished samples for stereographic projections. As usual for rolled sheet, the pole figures were referred to the sample directions, i.e. the rolling, transverse and normal directions (RD, TD and ND). As will be seen in Fig. 5.2, the vertical and horizontal axes in the pole figures are with respect to the RD and TD, denoted as 1 and 2. Since the samples are ultra-low carbon steel, Fe was the source of radiation and (100) and (110) pole figures were generated.

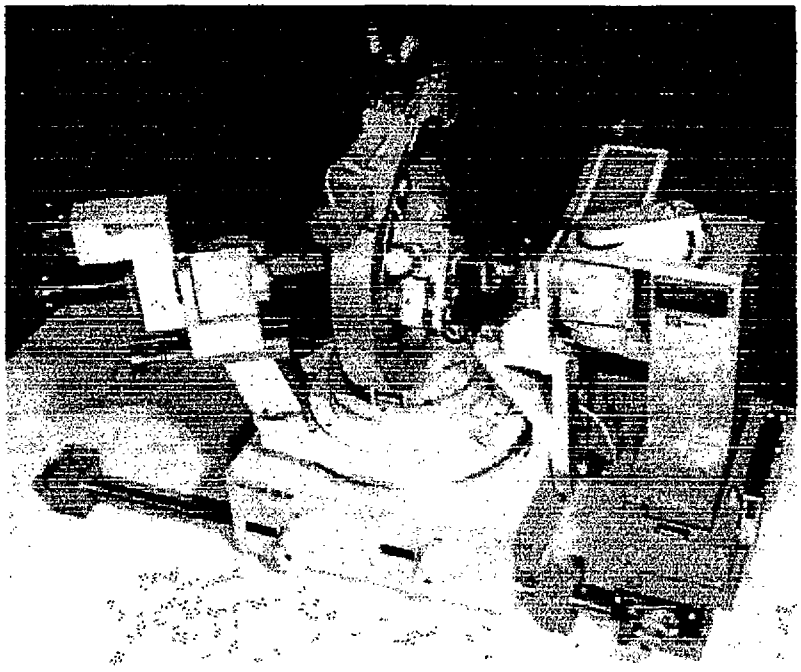

Figure 5.1 A Scintag Five Axis Pole Figure Goniometer

The textures were examined over a five-degree grid and the samples were tilted to 80°. The counting time was set to one second at each point. Upon completing the measurements a computer programme called popLA, developed at Los Alamos, was used so that the initial data could be corrected for background and defocusing, normalized to the standard intensity, relocated to the maximum symmetry, and extrapolated between 80° to 90° sample tilt. The pole figure inversion algorithm (WIMV) [82-83] included in the programme was then used to further re-calculate the pole figures. All of the 100 and 110 re-calculated pole figures are shown in Figs. 5.2(a) to (f).

5.2.2.2 Texture (Pole Figure) Simulation Performed at Queen's University

An identical set of as-received sample to that delivered to Los Alamos was forwarded to Queen's University. An outline of the procedure followed by Queen's has already been presented in Section 5.1.

The as-received sample was first measured on its mid-plane to obtain the (100), (110) and (211) pole figures, and the CODF of this sample was calculated based on the assumption of orthorhombic sample symmetry. Under the assumption of plane strain compression, the Taylor-Bishop-Hill (TBH) fully constrained model was then used to simulate the texture associated with the rolling process. Since the as-received sample is a body centred cubic (b.c.c) material, the model selects 5 out of 24 slip systems {110}<111> + {112}<111> from each of the discretized crystals based on their Schmid factors. The texture was determined using 3,194 crystallites discretized from the experimentally measured texture.

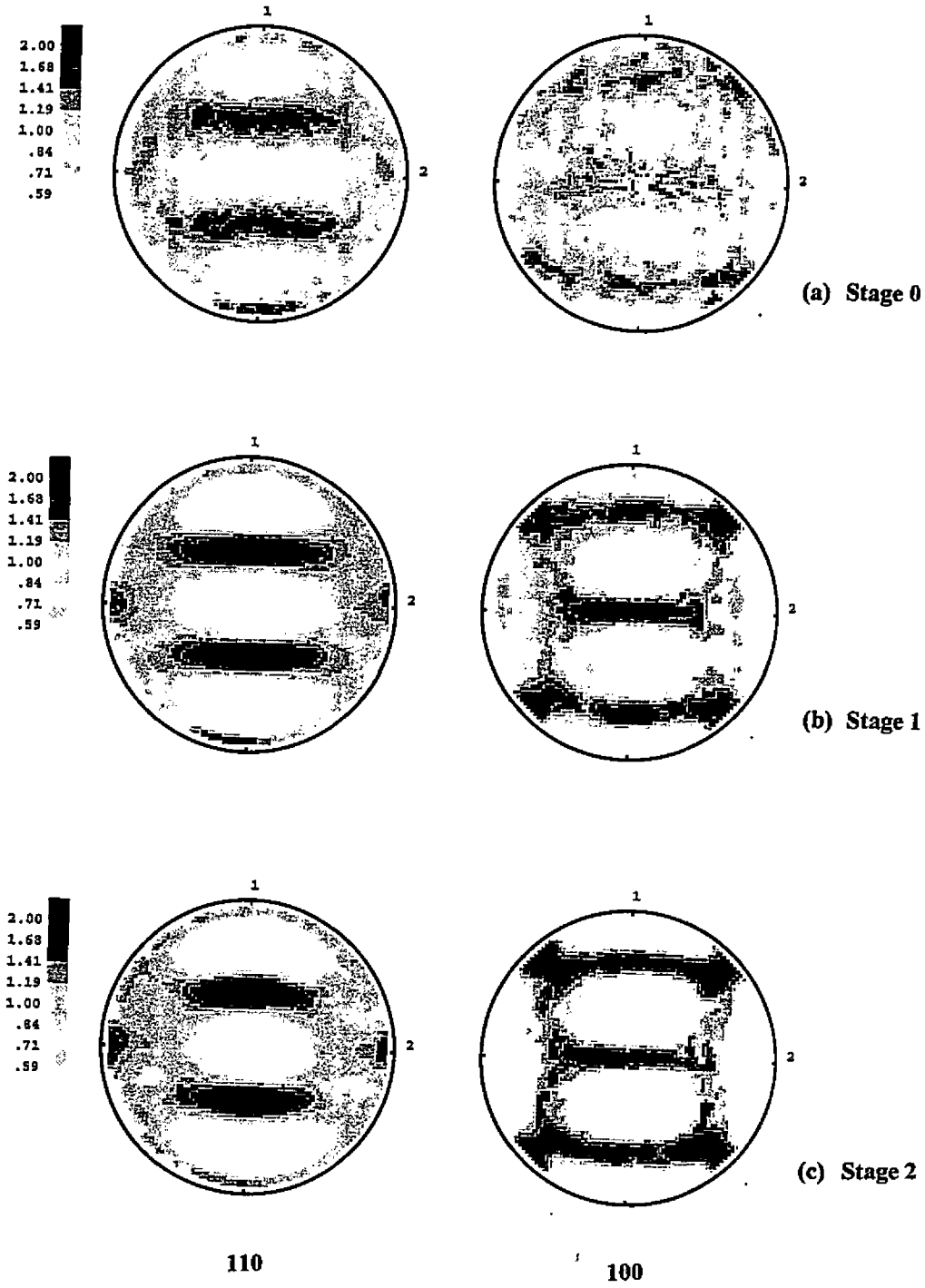

Figure 5.2 (100) and (110) Pole Figures Re-calculated by Los Alamos

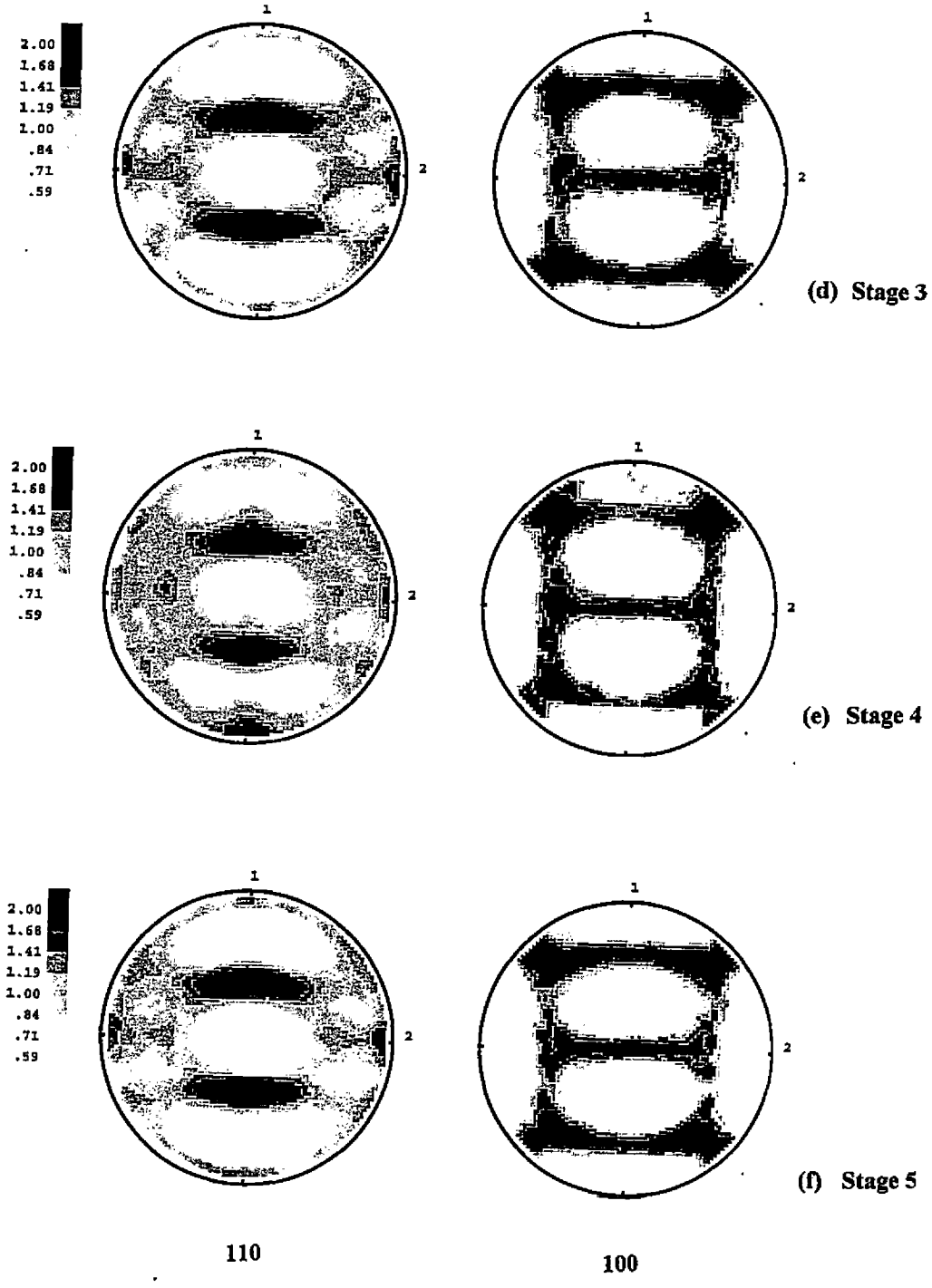

Figure 5.2 (100) and (110) Pole Figures Re-calculated by Los Alamos (Cont'd)

To predict the texture evolution, the total rolling strain, ε_T, was divided into a number of discrete steps. As seen in Table 4.2, the ε_T was 1.52. Initially it was divided into 15 deformation steps, and each step was further subdivided into increments of 0.01. During each increment the individual crystals would rotate, based on the selected set of active slip systems. At each strain increment a different set of slip systems could operate. Note, that when modelling the strain path the rolling process was assumed to be one of plane strain i.e. no change in width of the sheet. The CODFs, the pole figures and the corresponding yield loci yield loci were calculated after each roll stand. The method of producing the yield loci is explained in some detail in Ref. [37]. All of the pole figures are shown in Figs 5.3 (a) to (f).

Using the same approach, the r-values after each roll pass were calculated and are shown in Table 6.3.

5.2.2.3 Comparison of Pole Figures

The pole figures received from Los Alamos National Laboratory and Queen's University are compared in this section, and some of them are shown in Figs. 5.2 and 5.3 respectively. All these pole figures show the classical cold rolling texture of steel, where the {100} and {110} planes are the dominant orientation in the plane of the rolled sheet. In general the texture tended to strengthen as the material was reduced. The exception seems to be the measured texture after the final pass, as seen in Fig. 5.2(f). The agreement between the measured and predicted pole figures is very good, particularly for the 110 pole figures. The correspondence is not quite so good for the 100 pole figures.

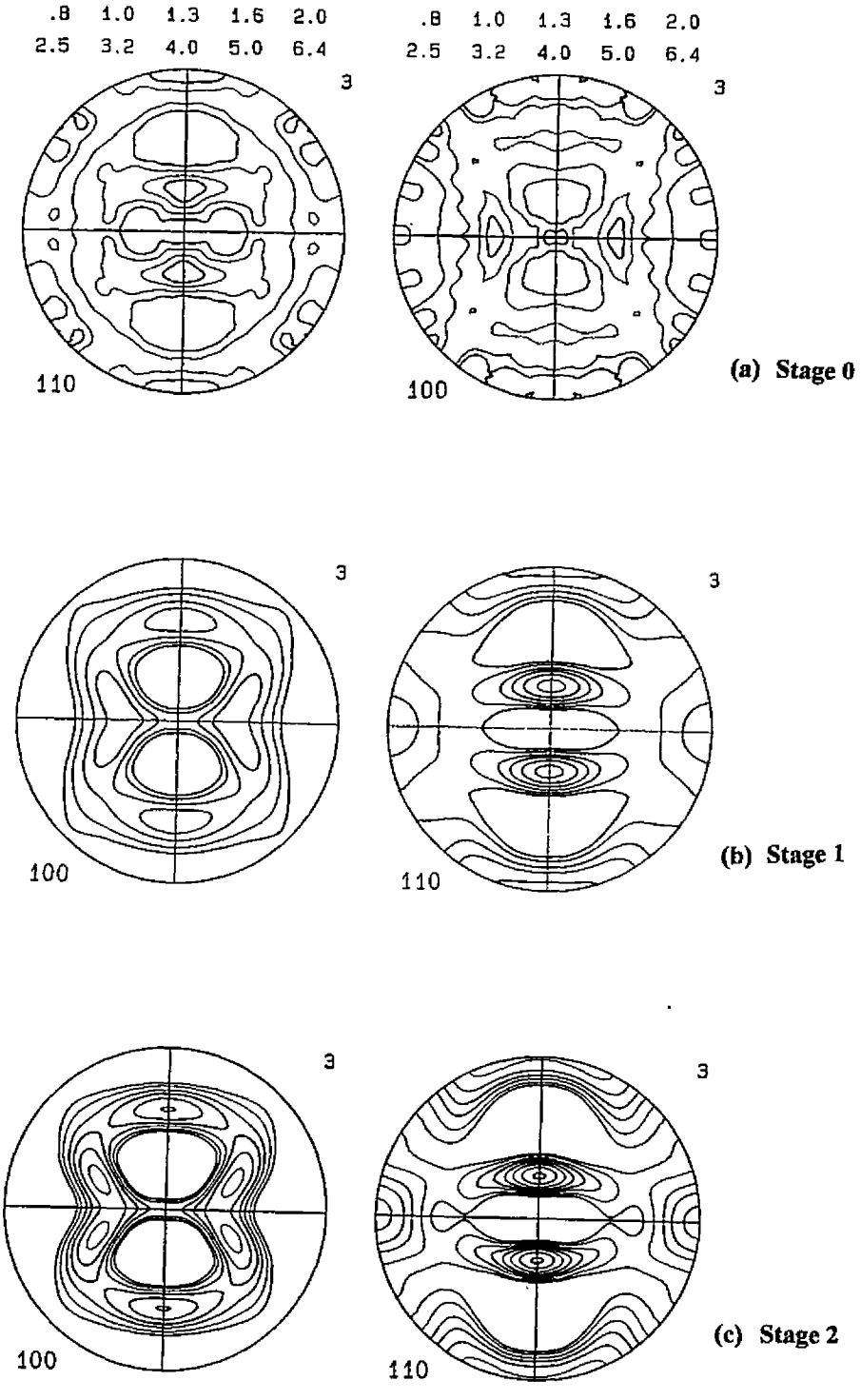

Figure 5.3 (100) and (110) Pole Figures Simulated by Queen's University

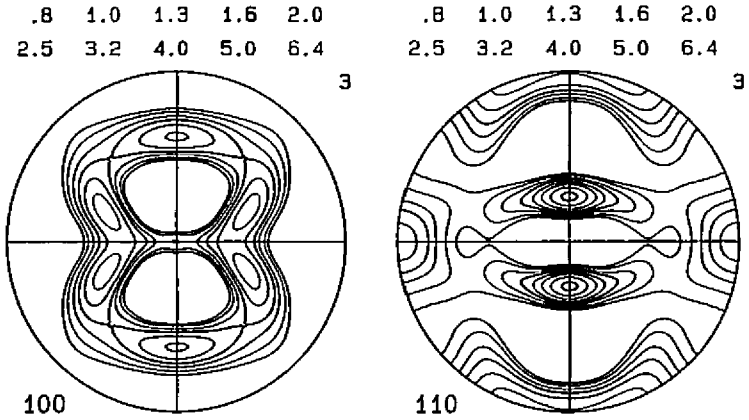

(d) Stage 3

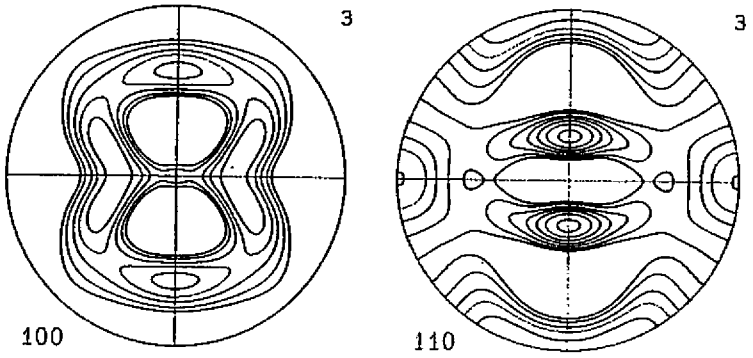

(e) Stage 4

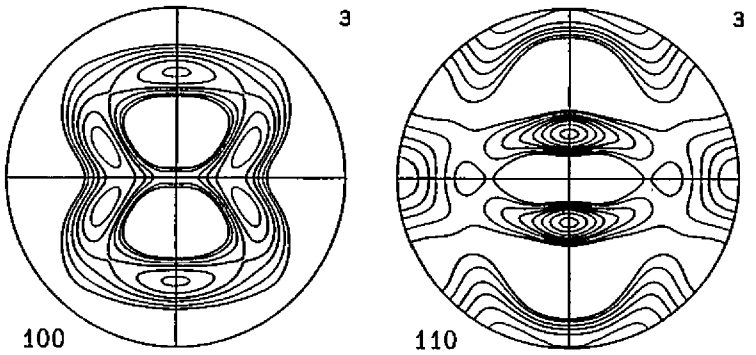

(f) Stage 5

Figure 5.3 (100) and (110) Pole Figures Simulated by Queen's University (Cont'd)

However, the similarity is obvious particularly after the first roll stand. The peaks have developed into three bands, which appear to be more concentrated in the experimental pole figures. The active slip systems are not known, and the predicted pole figures are based on the most likely systems but not necessarily those that actually operate. The results show the good predictability of the Van Houtte software, at least in this instance.

5.3 A Comparison of the Selected Yield Loci

5.3.1 Introduction

The crystallographic yield loci generated from the Van Houtte software and received from Queen's University are compared with the normalized yield loci calculated from Barlat's 94-yield criterion. The former and the latter yield loci are shown in Figures 5.4 and 5.5 respectively. As already stated, Barlat's loci are computed based on some the data generated from the yield loci and r-values determined at Queen's University. As discussed in Chapter 6, the material coefficients, the exponent m and some pseudo-experimental data are employed following the procedures described in Section 3.2.1.1 and Appendix A. A program for plotting Barlat's normalized yield criterion has been written in MATLAB is given in Appendix E.

5.3.2 A Comparison of the Selected Yield Loci

As seen in Figure 5.4, the dotted arrows demonstrate the change in shape of the yield locus as the reduction is increased. Figure 5.5 shows the yield loci after each reduction stage superimposed on each other. A comparison between the loci predicted by

Queen's University and the loci calculated according to Barlat are shown in Fig. 5.6 for each reduction stage. It is clear that the shapes are very similar and therefore demonstrates the predictive capabilities of Barlat's method [38, 47-48, 57-58].

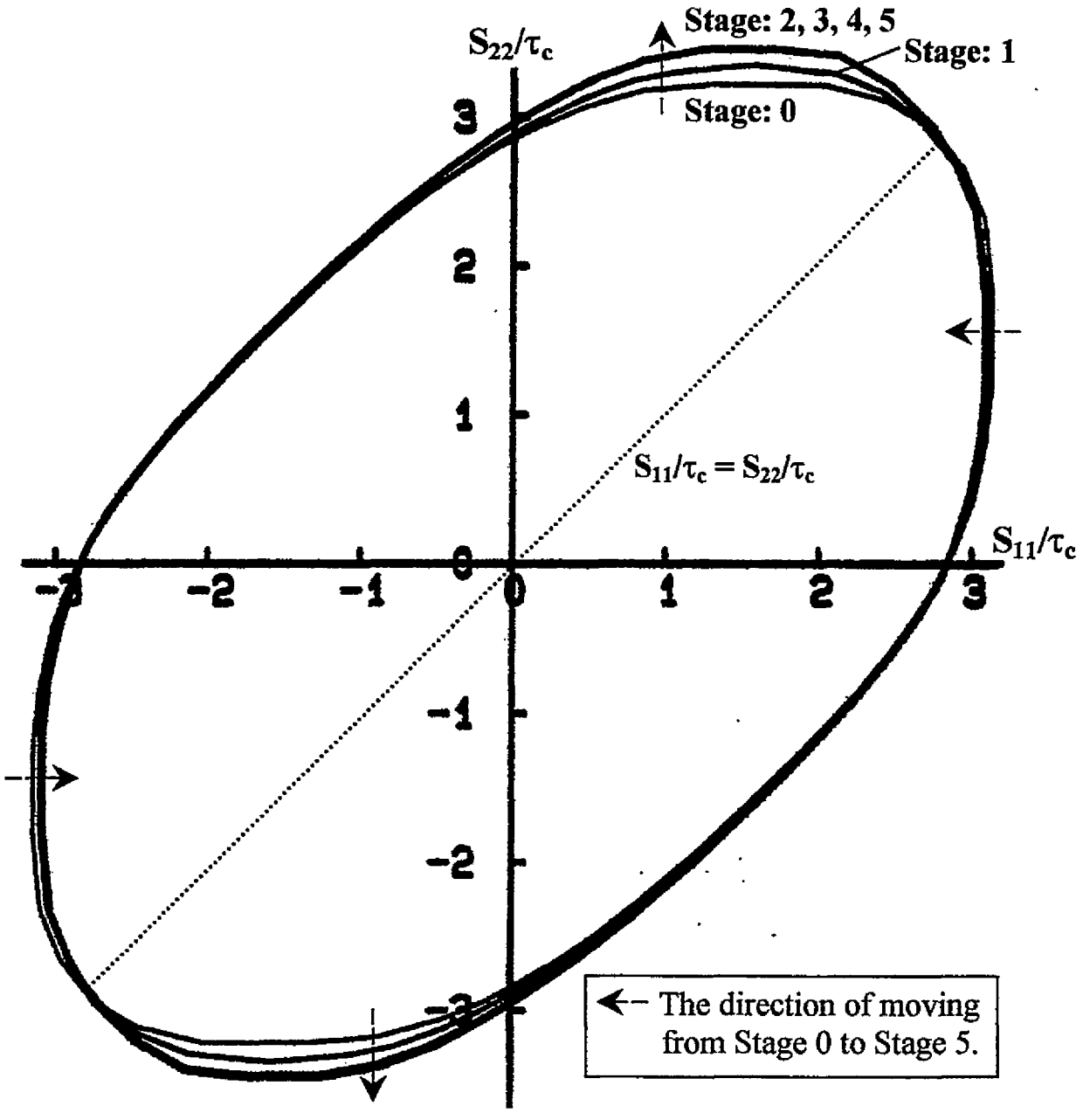

Figure 5.4 The Change in the Shape of the Yield Loci with Reduction

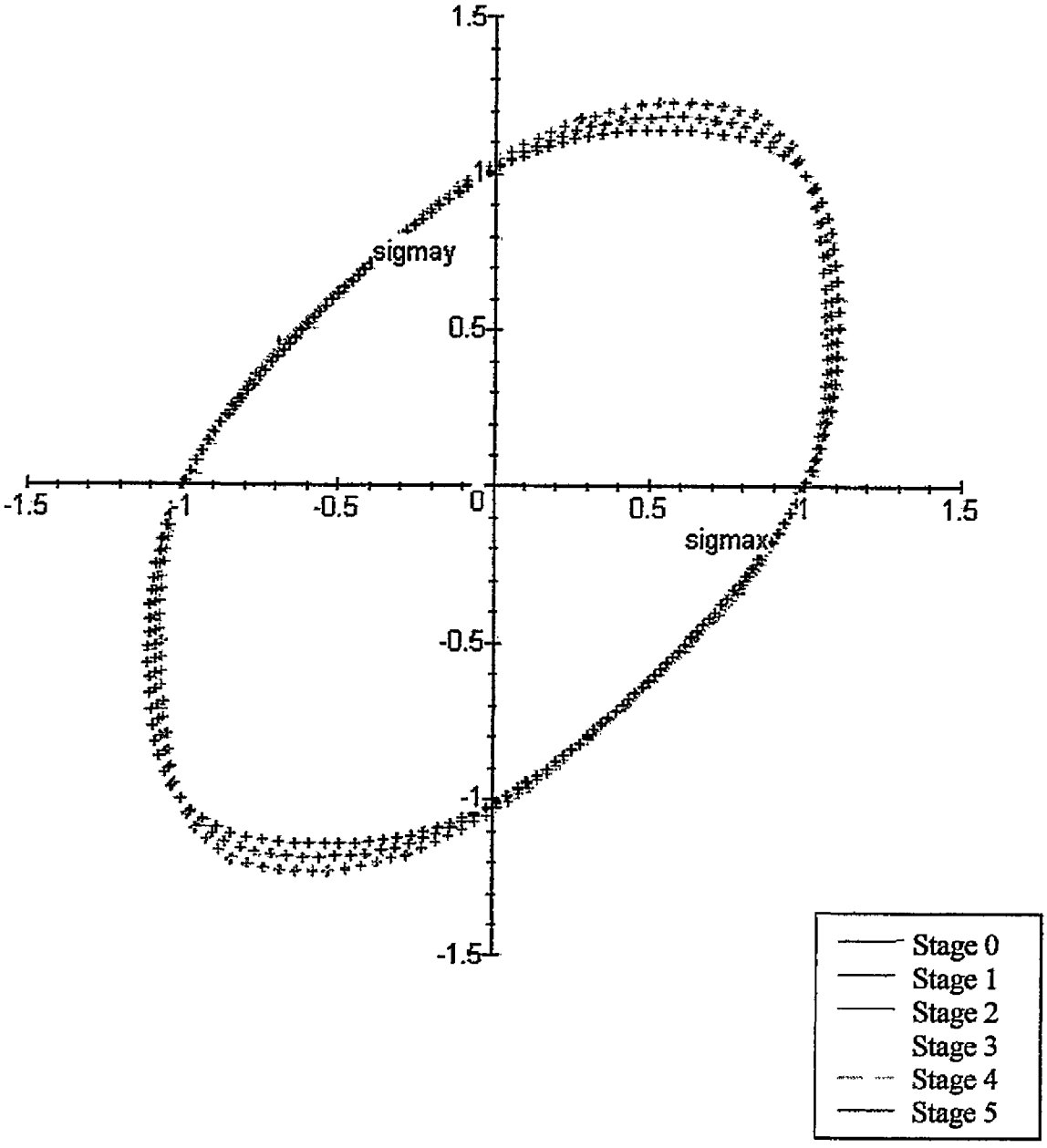

Figure 5.5 Barlat's 94 Yield Loci after each Roll Pass

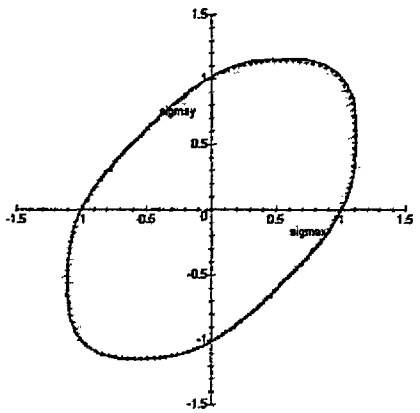

(a) Stage 0

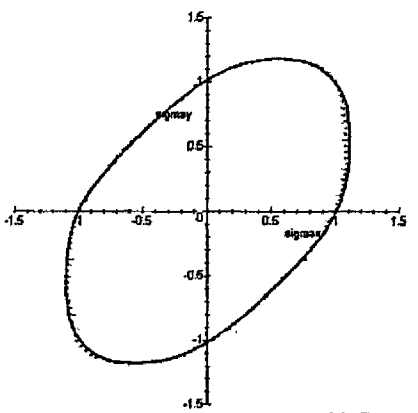

(b) Stage 1

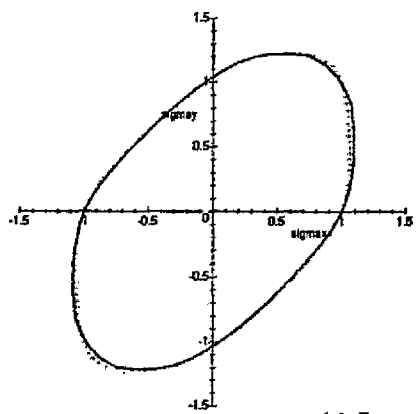

(c) Stage 2

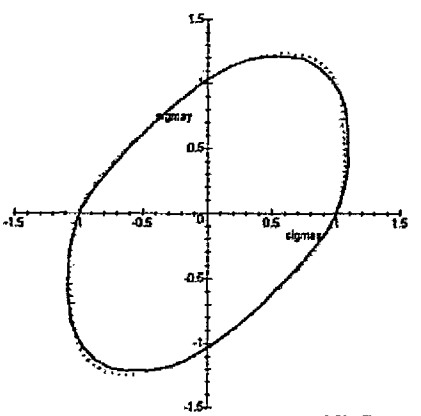

(d) Stage 3

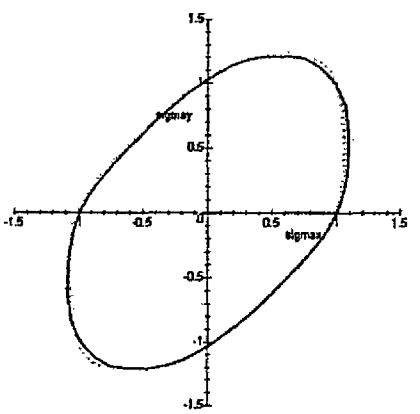

(e) Stage 4

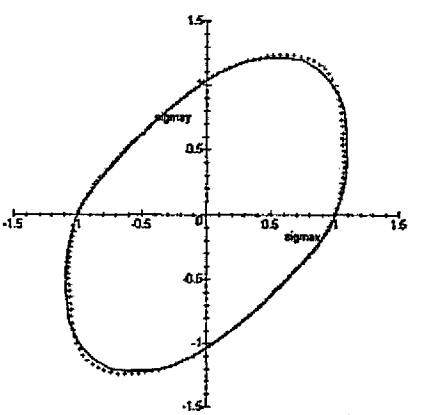

(f) Stage 5

Figure 5.6 A Comparison between the Loci Predicted by Queen's University and Barlat's 94 after each Roll Pass

Chapter 6

A Comparison of Some Analytical Yield Criteria

6.1 Introduction

In this chapter the predictions by some of the non-quadratic yield functions discussed in Chapter 2 and 3 are compared with each other, and also with the crystallographic yield loci derived using CODF analysis as outlined in Chapter 5. In order to evaluate certain coefficients in the various yield criteria it is necessary to perform experiments on the material to determine certain mechanical properties. However, as mentioned in Chapter 4, the author did not have sufficient material available to perform all the necessary mechanical tests. Instead mechanical property data were generated using CODF analysis. In particular, the predicted yield loci provide values for the uniaxial yield strength in the rolling (σ_0) and transverse (σ_{90}) directions as well as the biaxial yield strength (σ_b). CODF analysis can also predict the variation in the uniaxial yield strength (σ_θ) and the r-value (r_θ) at different orientations, θ, to the rolling direction i.e. θ varies from 0 to 90 degrees. The various yield criteria also use different values for the exponent m. Some investigators have used m = 6 or 8 following a suggestion by Hosford [50-52] who arrived at these values based on a comparison of yield loci derived from crystallographic calculations. With other criteria m can be evaluated explicitly once certain mechanical properties have been determined. For the yield function proposed by

Montheillet et al [61] the m value can be adjusted to give the best agreement between the predictions from the yield function and some other measured (or calculated) yield locus. In the present study the comparison locus was that determined from CODF analysis for the *as-received* IF steel. The best fit was with m = 2.1.

6.2 A Comparison of Some Analytical Yield Criteria

In this section predictions from five anisotropic functions are compared. The analytical functions are given below and in the form presented they are all based on the condition that the applied stress state is one of plane stress. Some include the shear stress term, σ_{xy}, others do not. The following are the selected yield functions.

Hosford [50-52] proposed a non-quadratic anisotropic yield function as follows

$$\phi = \left(\frac{r_{90}}{r_0 + r_{90}}\right)|\sigma_x|^m + \left(\frac{r_0}{r_0 + r_{90}}\right)|\sigma_y|^m + \left(\frac{r_0 r_{90}}{r_0 + r_{90}}\right)|\sigma_x - \sigma_y|^m = \bar{\sigma}^m \qquad (6.1)$$

where σ and $\bar{\sigma}$ are the tensile and the effective yield stresses, and r is the r-value. The subscripts x, y (or 0, 90) refer to the principal directions of anisotropy in the plane of a sheet.

Montheillet et al [61] derived the following yield function,

$$\Phi = g|\beta_1\sigma_x + \beta_2\sigma_y|^m + h|\sigma_x - \sigma_y|^m + 2n_{r(s)}|\sigma_{xy}|^m = \bar{\sigma}^m \qquad (6.2)$$

where $\beta_1 = \left(\frac{(\bar{\sigma}/\sigma_0)^m - h}{g}\right)^{\frac{1}{m}}$ and $\beta_2 = \left(\frac{(\bar{\sigma}/\sigma_{90})^m - h}{g}\right)^{\frac{1}{m}}$. The coefficients g and h can be calculated from,

$$\left.\begin{aligned} g &= \frac{(\bar{\sigma}/\sigma_{ave})^m}{2(r_{ave}+1)} \\ h &= g(2r_{ave}+1) \end{aligned}\right\} \tag{6.3}$$

where $r_{ave} = (r_0 + r_{90})/2$ and $\sigma_{ave} = (\sigma_0 + \sigma_{90})/2$. But the coefficient $n_{r(s)}$ can be obtained either from

$$n_r = g\left(r_{45} + \frac{1}{2}\right)(\beta_1 + \beta_2)^m \Big/ 2 \tag{6.4}$$

or

$$n_s = 2^{m-1}\{(\bar{\sigma}/\sigma_{45}) - g\} \tag{6.5}$$

depending on the accessibility of r_{45} and σ_{45} i.e. the r-value and tensile yield stress respectively at the 45° to the rolling direction. The yield stress, σ_θ, and r-value, r_θ, in any direction, θ, to the rolling direction are

$$\sigma_\theta = \frac{\bar{\sigma}}{\left(g\left|\beta_1\cos^2\theta + \beta_2\sin^2\theta\right|^m + h\left|\cos 2\theta\right|^m + 2n_{r(s)}\left|\sin\theta\cos\theta\right|^m\right)^{1/m}} \tag{6.6}$$

and

$$r_\theta = \frac{h\left|\cos 2\theta\right|^m + 4n_{r(s)}\left|\sin\theta\cos\theta\right|^m}{g(\beta_1+\beta_2)\left(\beta_1\cos^2\theta + \beta_2\sin^2\theta\right)\left|\beta_1\cos^2\theta + \beta_2\sin^2\theta\right|^{m-2}} - \frac{\beta_1\sin^2\theta + \beta_2\sin^2\theta}{\beta_1+\beta_2} \tag{6.7}.$$

Hill's 90-yield function [63] was expressed as

$$\begin{aligned} \Phi = \left|\sigma_x + \sigma_y\right|^m + \left|\sigma_x^2 + \sigma_y^2 + 2\sigma_{xy}^2\right|^{\frac{m}{2}-1}\left\{-2a_{r(s)}\left(\sigma_x^2 - \sigma_y^2\right) + b_{r(s)}(\sigma_x - \sigma_y)^2\right\} \\ + k_{r(s)}{}^m\left|(\sigma_x - \sigma_y)^2 + 4\sigma_{xy}^2\right|^{\frac{m}{2}} = (2\sigma_b)^m \end{aligned} \tag{6.8}$$

where σ_b and σ_{xy} are the biaxial tensile and the shear stress respectively, and $m = \frac{\ln(2+2r_{45})}{\ln(2\sigma_b/\sigma_{45})}$.

Naruse et al [74] explicitly expressed the coefficients a, b and using two different approaches either,

$$\left.\begin{aligned} a_r &= \left\{1+\frac{(m-2)\{r_{45}(r_0-r_{90})-2r_0r_{90}\}}{2\{r_0r_{90}(m-2)-(r_0+r_{90})\}}\right\}\frac{(r_0-r_{90})}{(r_0+r_{90})} \\ b_r &= \frac{m\{r_{45}(r_0+r_{90})-2r_0r_{90}\}}{r_0r_{90}(m-2)-(r_0+r_{90})} \\ k_r &= (1+2r_{45})^{\frac{1}{m}} \end{aligned}\right\} \qquad (6.9)$$

or

$$\left.\begin{aligned} a_s &= \{(2\sigma_b/\sigma_{90})^m-(2\sigma_b/\sigma_0)^m\}/4 \\ b_s &= \{(2\sigma_b/\sigma_{90})^m+(2\sigma_b/\sigma_0)^m\}/2-(2\sigma_b/\sigma_{45})^m \\ k_s &= \{(2\sigma_b/\sigma_{45})^m-1\}^{\frac{1}{m}} \end{aligned}\right\} \qquad (6.10)$$

The yield stress and r-value at any direction θ to the rolling direction are

$$\sigma_\theta = 2\sigma_b/\left(1-2a_{r(s)}\cos 2\theta+b_{r(s)}\cos^2 2\theta+k_{r(s)}{}^m\right)^{\frac{1}{m}} \qquad (6.11)$$

and

$$r_\theta = \left(\frac{k_{r(s)}{}^m+\frac{2}{m}b\cos^2(2\theta)-1}{1-a_{r(s)}\cos(2\theta)+\frac{m-2}{2m}b_{r(s)}\cos^2(2\theta)}\right)/2 \qquad (6.12)$$

Hill's (93) yield function [65] is of the following form,

$$\phi = \frac{\sigma_x{}^2}{\sigma_0{}^2}-\frac{c_h\sigma_x\sigma_y}{\sigma_0\sigma_{90}}+\frac{\sigma_y{}^2}{\sigma_{90}{}^2}+\left\{(p+q)-\frac{p|\sigma_x|+q|\sigma_y|}{\sigma_b}\right\}\frac{\sigma_x\sigma_y}{\sigma_0\sigma_{90}}=1 \qquad (6.13)$$

where $c_h = \sigma_0\sigma_{90}\left(\frac{1}{\sigma_0^2}+\frac{1}{\sigma_{90}^2}-\frac{1}{\sigma_b^2}\right)$, $p = \dfrac{\frac{2r_0(\sigma_b-\sigma_{90})}{\sigma_0^2(1+r_0)} - \frac{2r_{90}\sigma_b}{\sigma_{90}^2(1+r_{90})} + \frac{c_h}{\sigma_0}}{\sigma_0^{-1}+\sigma_{90}^{-1}-\sigma_b^{-1}}$

and $q = \dfrac{\frac{2r_{90}(\sigma_b-\sigma_0)}{\sigma_{90}^2(1+r_{90})} - \frac{2r_0\sigma_b}{\sigma_0^2(1+r_0)} + \frac{c_h}{\sigma_{90}}}{\sigma_0^{-1}+\sigma_{90}^{-1}-\sigma_b^{-1}}$.

Barlat [38, 47, 48] has recently proposed a new (94) yield function in the following manner,

$$\phi = \alpha_x |s_{yy}-s_{zz}|^m + \alpha_y |s_{zz}-s_{xx}|^m + \alpha_z |s_{xx}-s_{yy}|^m = 2\bar{\sigma}^m \qquad (6.14)$$

It can be generalized as

$$\Phi = \alpha_1 |s_{22}-s_{33}|^m + \alpha_2 |s_{33}-s_{11}|^m + \alpha_3 |s_{11}-s_{22}|^m = 2\bar{\sigma}^m \qquad (6.15)$$

by using $\alpha_k = \alpha_x p_{xk}^2 + \alpha_y p_{yk}^2 + \alpha_z p_{zk}^2$ and $\mathbf{s} = \mathbf{L}\,\sigma$, the detailed derivation of this function is discussed in Chapter 3.

The basic requirements for each yield function are summarized in Table 6.1.

Table 6.1 Basic Requirements for the Yield Criteria

Yield Criterion	Yield Stress	r-value	Exponent m
Hosford [50-52]	$\sigma_b = \bar{\sigma}$	r_0, r_{90}	m = 6 (b.c.c.)
Hill's 93 [65]	$\sigma_0, \sigma_{90}, \sigma_b = \bar{\sigma}$	r_0, r_{90}	
Montheillet [61]	$\sigma_0, \sigma_{90}, \sigma_b = \bar{\sigma}, (\sigma_{45})^*$	$r_0, r_{90}, (r_{45})^*$	m = 2.1 (selected)
Hill's 90 [63]	$\sigma_{45}, \sigma_b = \bar{\sigma}, (\sigma_0, \sigma_{90})^*$	$r_{45}, (r_0, r_{90})^*$	$m = \frac{\ln(2+2r_{45})}{\ln(2\sigma_b/\sigma_{45})}$
Barlat's 94 [38, 47-48]	$\sigma_0, \sigma_{90}, \sigma_b = \bar{\sigma}, (\sigma_{45}, \sigma_{xy})^*$	$r_0, r_{90}, (r_{45})^*$	m = 6 (b.c.c.)

*Parentheses ( ) denote options, i.e. depending on the accessibility of the data and the application.

6.2.1 Yield Strengths and r-values

6.2.1.1 Yield Criteria without a Shear Stress Term

Hosford's [50-52] and Hill's 93 [65] yield criteria have no in-plane shear stress term, σ_{xy}. As shown in Table 6.1, the experimental data they need are, three yield stresses (σ_0, σ_{90}, and σ_b) and two r-values (r_0 and r_{90}). As Barlat et al suggested [48], the effective yield stress $\bar{\sigma}$ is made equal to σ_b. As discussed in Chapter 4, the present author did not have access to all of these experimental data. Only the yield stress in the rolling (x) direction after each roll stand, and the r-value in the same direction of the *as-received* material only were available. Therefore, the crystallographic yield loci and the r-values (r_0, r_{45} and r_{90}) predicted from the texture analysis served as the experimental data, see Chapter 5. The yield stresses, σ_0, σ_{90} and σ_b, could be obtained and used after the shape of each yield locus was normalized. The experimental normalized biaxial yield stresses, $\sigma_b/\bar{\sigma}$, and the experimental normalized uniaxial yield stresses in the rolling and transverse directions, $\sigma_0/\bar{\sigma}$ and $\sigma_{90}/\bar{\sigma}$, are listed in Table 6.2 while the r-values at 0, 45 and 90 degrees to the rolling direction are shown in Table 6.3.

Table 6.2 Experimental Normalized Yield Stresses at Various Stages

Stage	$\sigma_0/\bar{\sigma}$	$\sigma_{90}/\bar{\sigma}$	$\sigma_b/\bar{\sigma}$
0	0.998	1.014	1
1	0.998	1.021	1
2	0.998	1.039	1
3	0.998	1.039	1
4	0.998	1.039	1
5	0.998	1.039	1

Table 6.3 Experimental r-values at Various Stages

Stage	r_0	r_{45}	r_{90}
0	0.97	1.26	1.20
1	0.83	1.34	1.49
2	0.67	1.66	1.77
3	0.67	1.70	1.82
4	0.68	1.65	1.74
5	0.67	1.74	1.85

6.2.1.2 Yield Criteria with a Shear Stress Term

It should be noted that the yield criteria with an in-plane shear stress term i.e. Hill's 90 [63], Montheillet's [61] and Barlat's 94 [38, 47, 48] may require additional experimental data to execute the computations. To compare the three criteria, regardless of whether an in-plane shear stress σ_{xy} is acting, an additional piece of information is required. As described in Section 3.2.2 and Appendix B, if one of the experimental values σ_{45}, r_{45} or $(\sigma_{xy})_Y$ is determined, the numerical method can predict the theoretical value of the other two. Since only the pseudo-experimental r-value, r_{45}, was available from the texture analysis, the theoretical yield stress at 45° to the rolling direction, σ_{45}, and theoretical yield shear stress, $(\sigma_{xy})_Y$, were generated by the numerical method. The present author also used the theoretical value, σ_{45} , as a means of evaluating each of the three criteria. These results are discussed later this chapter. Table 6.4 shows the normalized pseudo-experimental data $\sigma_{45}/\overline{\sigma}$ at all stages. As a reference, the normalized theoretical data $(\sigma_{xy})_Y/\overline{\sigma}$ are also shown in Table 6.4.

Table 6.4 Normalized Pseudo-Experimental and Theoretical Yield Stresses

Stage	$\sigma_{45}/\bar{\sigma}$	$(\sigma_{xy})_Y/\bar{\sigma}$
0	0.974	0.535
1	0.958	0.524
2	0.894	0.485
3	0.890	0.481
4	0.899	0.487
5	0.885	0.478

6.2.2 Exponent m

Another basic requirement for computing the yield criteria is the exponent m, as seen in Table 6.1. The value of this exponent is usually determined either, explicitly pre-assigned from the crystal structure of the material or selected to give the best fit between the predicted and the experimental data. Based on the crystallographic calculation for b.c.c. and f.c.c. metals, Hosford [50-52] and Barlat et al [38, 47, 48, 57, 58] suggested that for a good fit to their analytical yield loci, the values of the exponent m should be 6 and 8 respectively. A value of 6 was used here since the cold rolled steel was more in accordance with the material used by Hosford. Alternatively, Hill [63, 65] calculated the exponent m either from $m = \frac{\ln(2 + 2r_{45})}{\ln(2\sigma_b / \sigma_{45})}$ or it was ignored, see Eqns. (6.8) and (6.13) for details.

Likewise, Montheillet et al [61] suggested that the exponent m can be either determined explicitly if the yield stress in plane strain tension at 0° or 90° to the rolling direction is known, or determined by comparing the predicted and the experimental data. An explicit determination of the yield stress was not possible, and so the comparison method was used. As mentioned in Section 6.2.1.2 two approaches were used to

calculate the yield loci. The first used the r_{45} value (referred to herein as Scheme R), while the second used σ_{45}, which is defined as Scheme S.

Figure 6.1 shows the variation in the normalized yield stress with orientation, θ, to the rolling direction according to Montheillet and his co-workers, based on Scheme S. The results are for the *as-received* material at entry to the roll stands i.e. stage 0. Different values of m have been used in the calculations, and it is seen that it can have a marked effect on the results. Figure 6.2 shows how the r-value varies with θ, according to Scheme R. Values can be read from Figs. 6.1 and 6.2 and should be compared with some of the numerical value given in Tables 6.2 and 6.3. Some of the results given in these tables are repeated in tables 6.7 and 6.8. The latter two tables provide a more comprehensive listing and give results for each yield criterion analyzed in this chapter.

Figure 6.3 shows yield loci calculated according Montheillet et al [61] at stage 0 for different values of m. The yield locus with black outline is the crystallographic locus calculated by researchers at Queen's University. The yield locus with m=2.1 gives the best fit to the crystallographic locus. Consequently this value of m was used to compare the results derived in [61] with those from Hosford and Barlat. Table 6.5 lists some of the m-values used in the calculations.

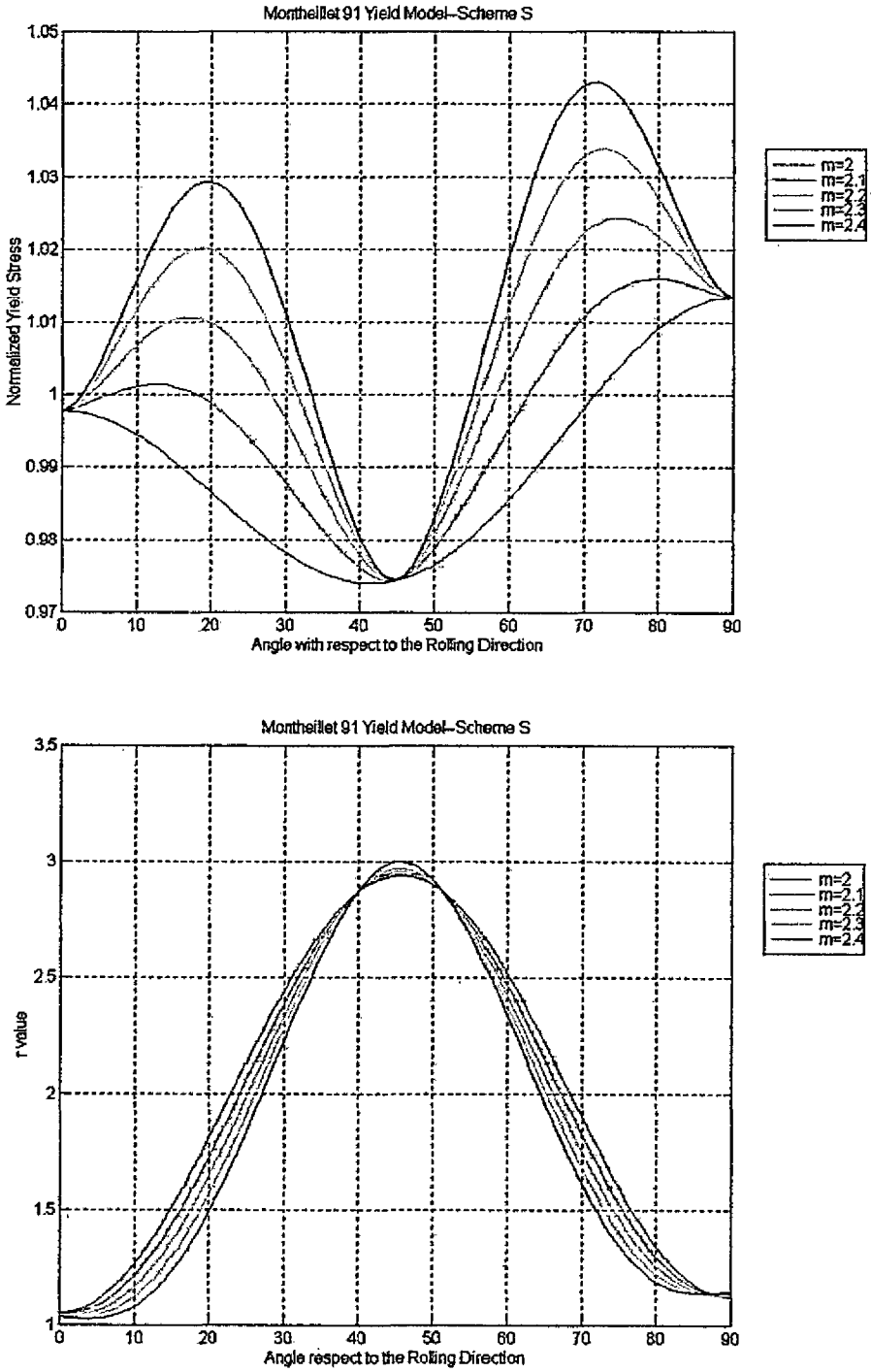

Figure 6.1 Influence of m on the Normalized Yield Stress and r-value due to Montheillet et al [61] SCHEME S

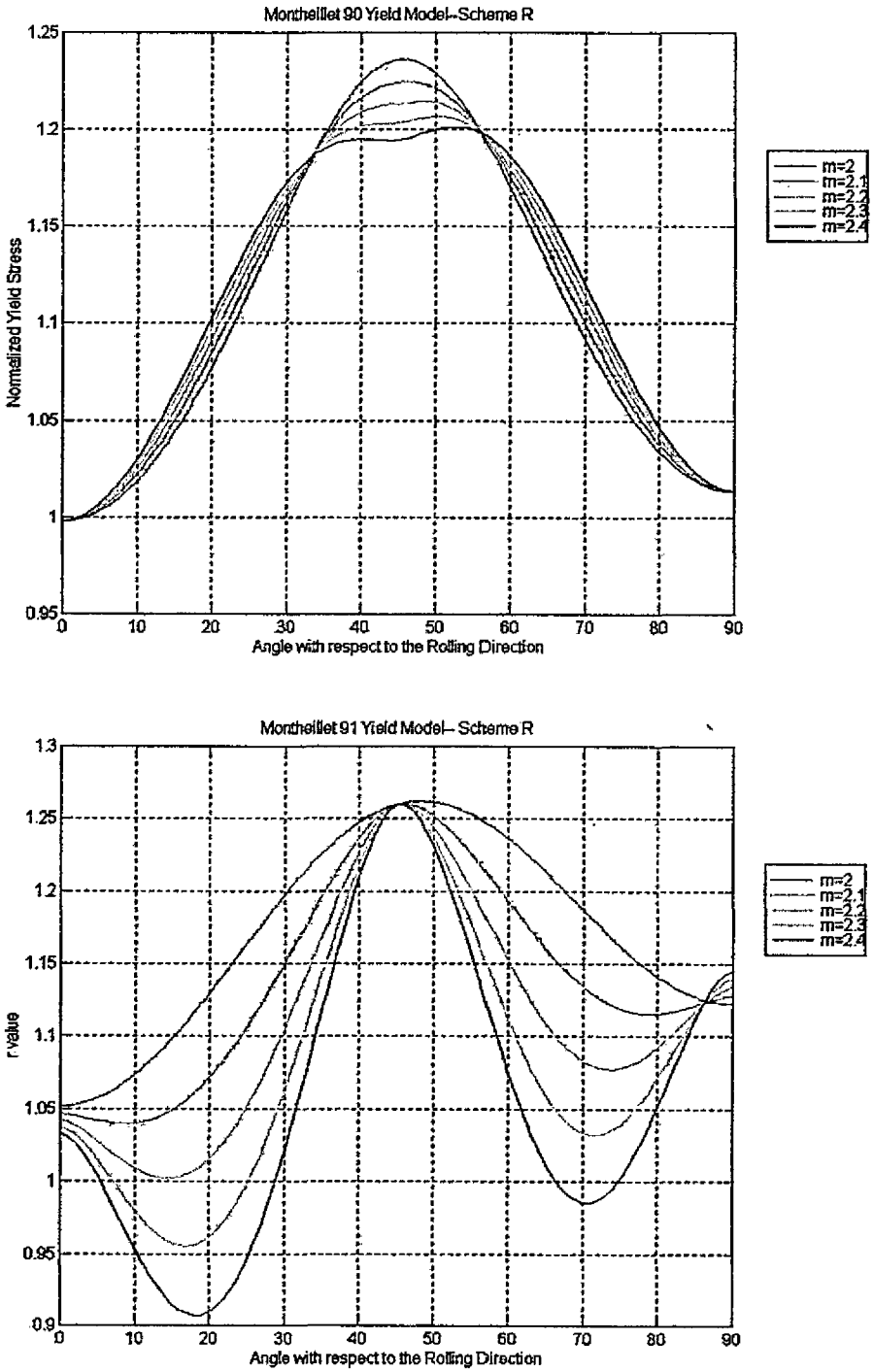

Figure 6.2 Influence of m on the Normalized Yield Stress and r-value due to Montheillet et al [61] SCHEME R

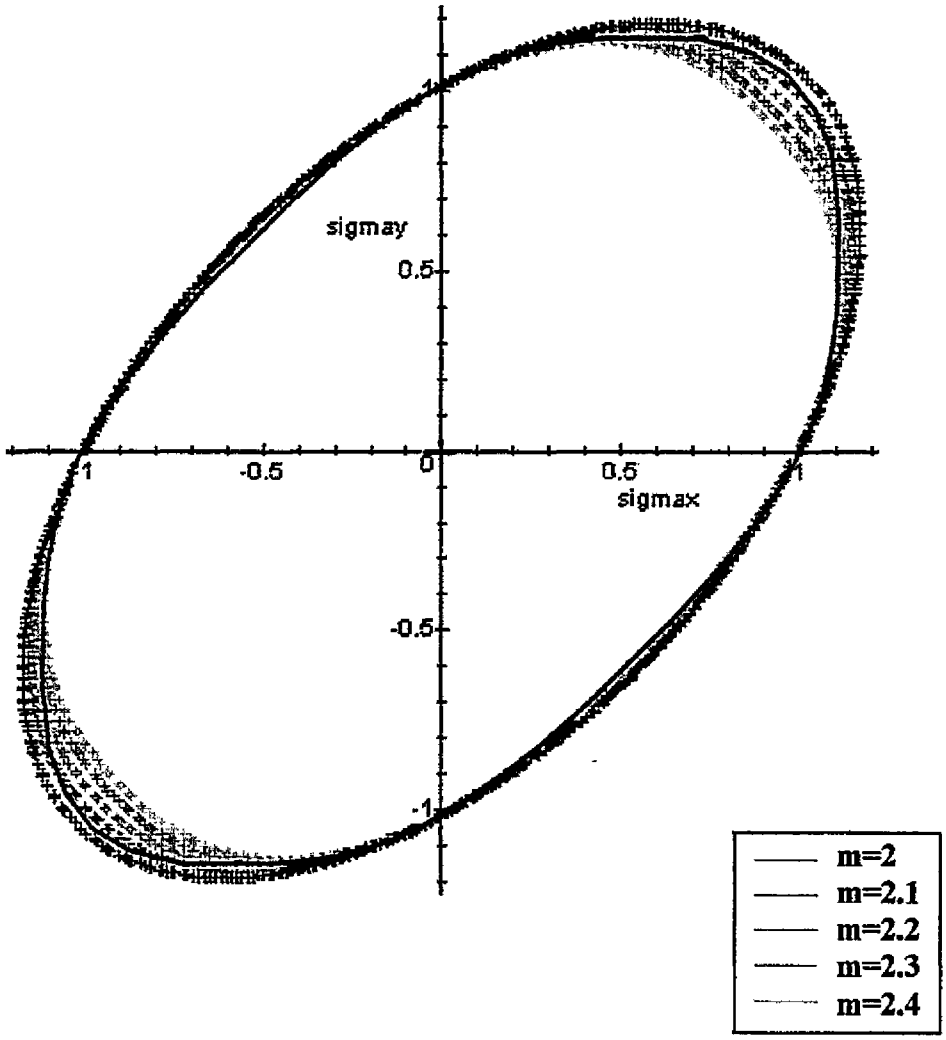

Figure 6.3 Influence of m on the Normalized Yield Loci at Stage 0, predicted by Montheillet et al

Table 6.5 Exponent m at All Stages for the Four Yield Criteria

Stage	Exponent m			
	Hosford	Montheillet	Hill's 90	Barlat's 94
0	6	2.1	2.0978	6
1	6	2.1	2.0966	6
2	6	2.1	2.0765	6
3	6	2.1	2.0814	6
4	6	2.1	2.0841	6
5	6	2.1	2.0858	6

6.2.3 Material Coefficients

The material coefficients in each of the five yield criteria can now be determined. The coefficients in Hosford's [50-52], Montheillet's [61], Hill's 90 [63] and 93 [65] criteria were calculated from the equations mentioned earlier, while the coefficients in Barlat's 94 criteria [38] was found by the numerical method described in Section 3.2 (see Appendix C for the MATLAB program). Table 6.6 lists the results of all the coefficients at each deformation stage.

Table 6.6 Material Coefficients for All Yield Criteria at All Stages

Hosford's Yield Criterion [50-52]			
Stage	$\frac{r_{90}}{(r_0 + r_{90})}$	$\frac{r_0}{(r_0 + r_{90})}$	$\frac{r_0 r_{90}}{(r_0 + r_{90})}$
0	0.5530	0.4470	0.5364
1	0.6422	0.3578	0.5331
2	0.7254	0.2746	0.4860
3	0.7309	0.2691	0.4897
4	0.7190	0.2810	0.4889
5	0.7341	0.2659	0.4919

Table 6.6 Material Coefficients for All Yield Criteria at All Stages (Continued)

Hill's 93 Yield Criterion [65]			
Stage	c_h	p	q
0	0.9890	-0.0852	-0.0111
1	0.9814	-0.1866	0.0533
2	0.9652	-0.2574	0.1306
3	0.9652	-0.2697	0.1306
4	0.9652	-0.2501	0.1231
5	0.9652	-0.2769	0.1306

Montheillet's Yield Criterion* [61]						
Stage	g	h	β_1	β_2	n_r	n_s
0	0.2370	0.7512	1.0324	0.9672	0.8937	1.7557
1	0.2269	0.7533	1.0500	0.9490	0.8940	1.8596
2	0.2168	0.7459	1.0877	0.9091	1.0006	2.2460
3	0.2144	0.7484	1.0886	0.9080	1.0076	2.2814
4	0.2178	0.7450	1.0873	0.9095	1.0005	2.2170
5	0.2130	0.7498	1.0892	0.9074	1.0190	2.3154

Hill's 90 Yield Criterion* [63]						
Stage	k_r	k_s	a_r	a_s	b_r	b_s
0	1.8220	1.8220	-0.1050	-0.0347	-0.4144	-0.2891
1	1.8616	1.8616	-0.2805	-0.0513	-0.6054	-0.4859
2	2.0232	2.0232	-0.4385	-0.0847	-1.4837	-1.2523
3	2.0814	2.0814	-0.4477	-0.0852	-1.5620	-1.3188
4	2.0135	2.0135	-0.4251	-0.0854	-1.4609	-1.2112
5	2.0523	2.0523	-0.4524	-0.0856	-1.6469	-1.3866

Barlat's 94 Yield Criterion [38, 47-48]							
Stage	α_x	α_y	α_z	c_1	c_2	c_3	c_6
0	0.7443	0.9273	1	1.0322	1.0286	0.9985	1.0442
1	0.5266	1.1625	1	1.0722	0.9940	0.9842	1.0657
2	0.4142	1.5412	1	1.0778	0.9523	0.9752	1.1523
3	0.3965	1.5449	1	1.0828	0.9515	0.9757	1.1601
4	0.4252	1.4910	1	1.0755	0.9590	0.9743	1.1469
5	0.3865	1.5475	1	1.0856	0.9509	0.9760	1.1677

*The subscripts r and s stand for calculations based on Scheme R and Scheme S respectively, see Sections 6.2.1.2 and 6.2.2.

6.3 Comparison of Normalized Yield Loci

The procedure, described in Section 3.2.1.1 and Appendix A, and written in the MATLAB program in Appendix E, was employed to plot the Barlat's normalized yield loci after each deformation stage. As seen in Chapter 5, it was found that the shape of the Barlat's loci and the crystallographic yield loci were very similar, especially at the stage 0. Hence, these two yield loci are now compared in the following sections with the yield loci predicted from the other four analytical yield criteria, both with and without the shear stress term σ_{xy}.

6.3.1 Yield Criteria without a Shear Stress Term

Figures 6.4(a) to (f) the normalized yield loci due to Barlat, Hill (93) and Hosford with that predicted by Queen's University from texture analysis, after each reduction stage. Barlat's yield criterion [38, 47, 48] provides the best fit to the crystallographic yield loci, although Hosford's [50-52] criterion is also very close. While Hill's [65] model provides a reasonable fit; there is deviation in the 2^{nd} and 4^{th} quadrants. Tables 6.7 and 6.8 provide numerical values for the normalized yield stress and r-values according to Queen's University and from the predictions due to Hill, Hosford and Barlat.

6.3.2 Yield Criteria with a Shear Stress Term

In a similar manner to Fig. 6.4, Figs. 6.5(a) to (f) compare the normalized yield loci due to Barlat [38, 47, 48], Montheillet et al [61] and Hill [63] with the crystallographic yield loci predicted by Queen's University, but now a shear stress term,

σ_{xy}, is included. As before, the Barlat's yield criterion gives the best correspondence, while Hill's (Scheme R) method provides the worst agreement, particularly in the 2nd and 4th quadrants.

6.4 Variation in the Normalized Yield Stress and r-value with Orientation

To calculate the variation in the normalized yield stress and the r-value with orientation to the rolling direction, it is necessary to include the shear stress term, σ_{xy} , in the yield criterion. Hence only the criteria discussed in the preceding section are appropriate. Hosford [73] did attempt to modify his earlier model [50–52] to allow for a shear stress term, but without too much success.

Detailed programs for plotting Barlat's yield loci when a shear stress is considered are given in Appendix D. While Appendix F provides programs for calculating and plotting the variation in the normalized yield stress and the r-value with orientation to the rolling direction. To calculate the yield criterion due to Hill [63] and Montheillet et al [61] two approaches were used, as discussed in Sections 6.2.1.2 and 6.2.2. The first used the r_{45} value and is referred to as Scheme R (or Hill-r, Montheillet-r), the second used the σ_{45} value and is denoted as Scheme S (or Hill-s, Montheillet-s).

6.4.1 Results of the Variation in the Yield Stress and r-value with Orientation

Figures 6.6 (a) to (e) show the variation in the normalized yield stress with orientation to the rolling direction based on the yield criteria due to Barlat, Hill, and Montheillet. Similarly Figs. 6.7 (a) to (e) show how the r-value varies. As already

mentioned Tables 6.7 and 6.8 list the numerical (predicted) values, and it is clear that the method of calculation i. e. Scheme R or Scheme S, can exert a strong influence on the results.

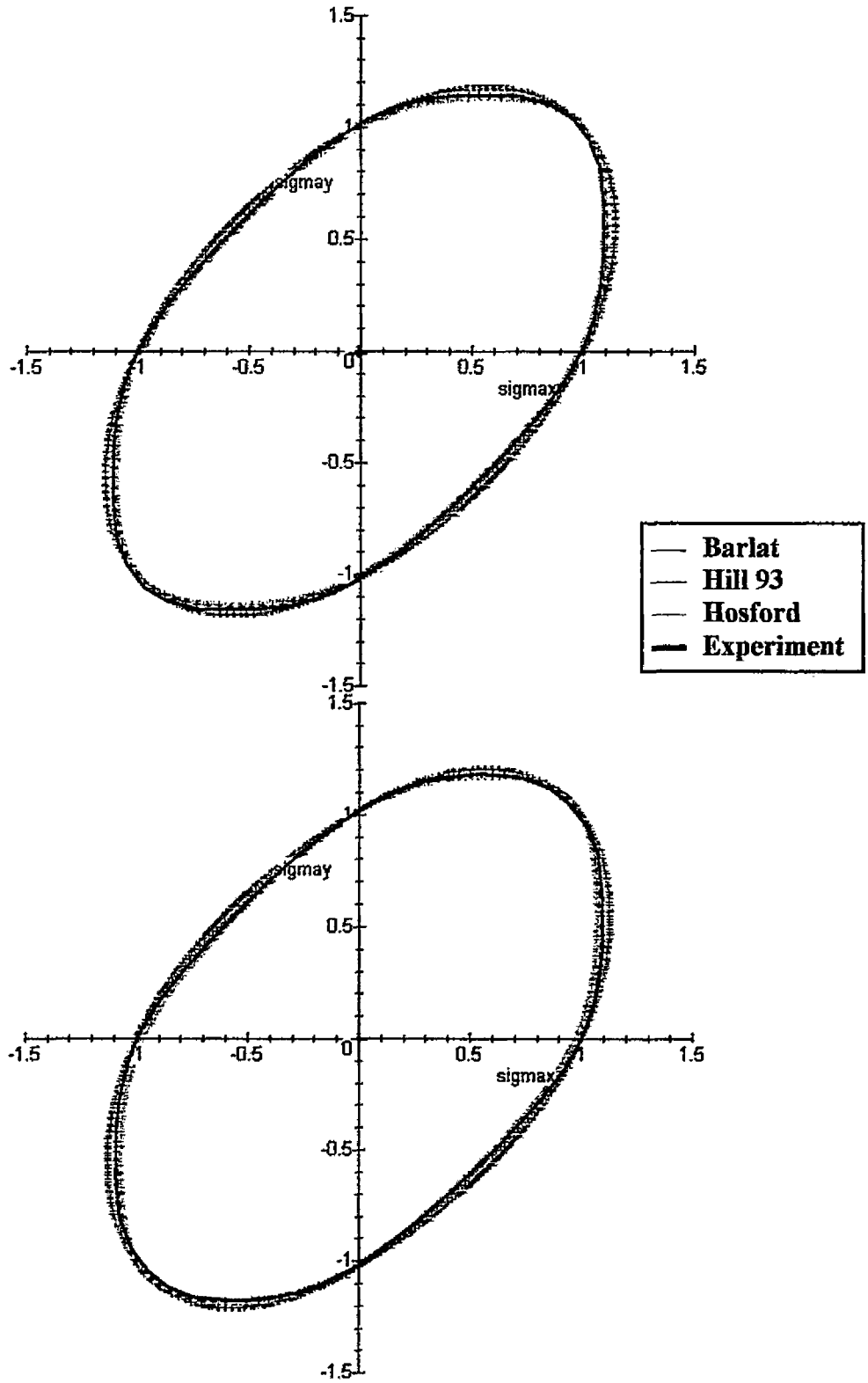

Figure 6.4 Comparison of the Normalized Yield Loci without a Shear Stress Term

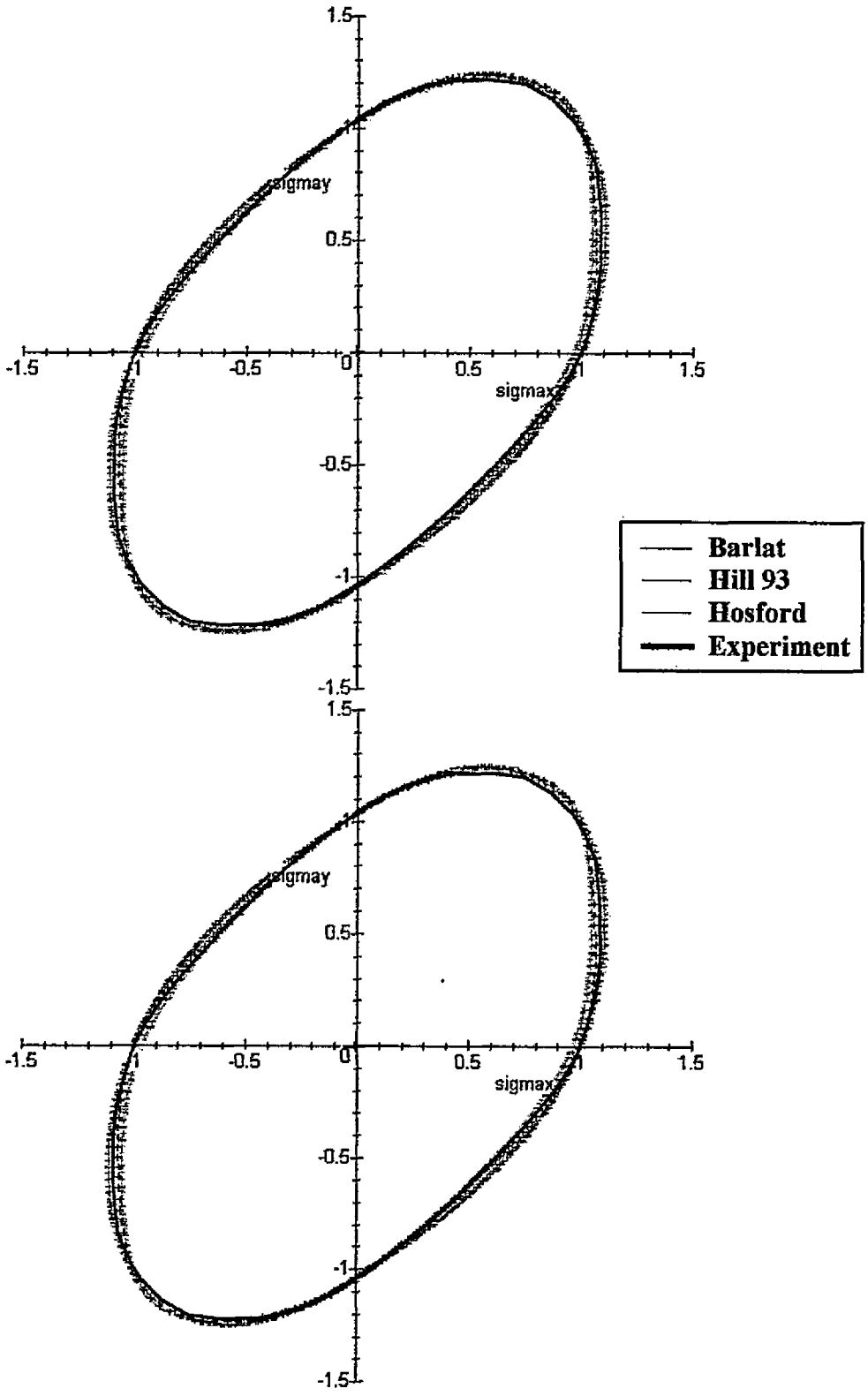

Stage 2

Stage 3

Figure 6.4 Comparison of the Normalized Yield Loci without a Shear Stress Term (Cont'd)

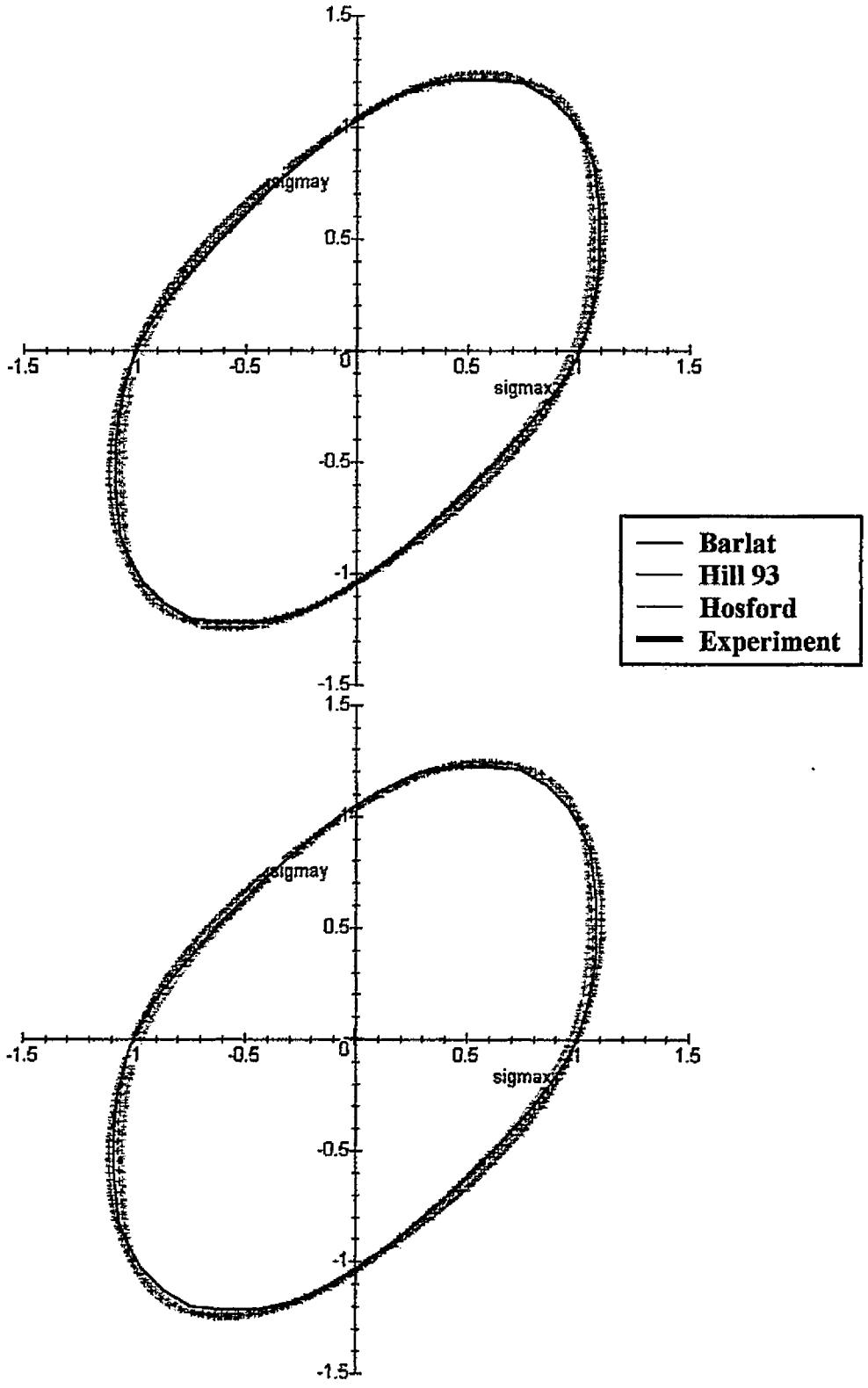

Stage 4

Stage 5

Figure 6.4 Comparison of the Normalized Yield Loci without a Shear Stress Term (Cont'd)

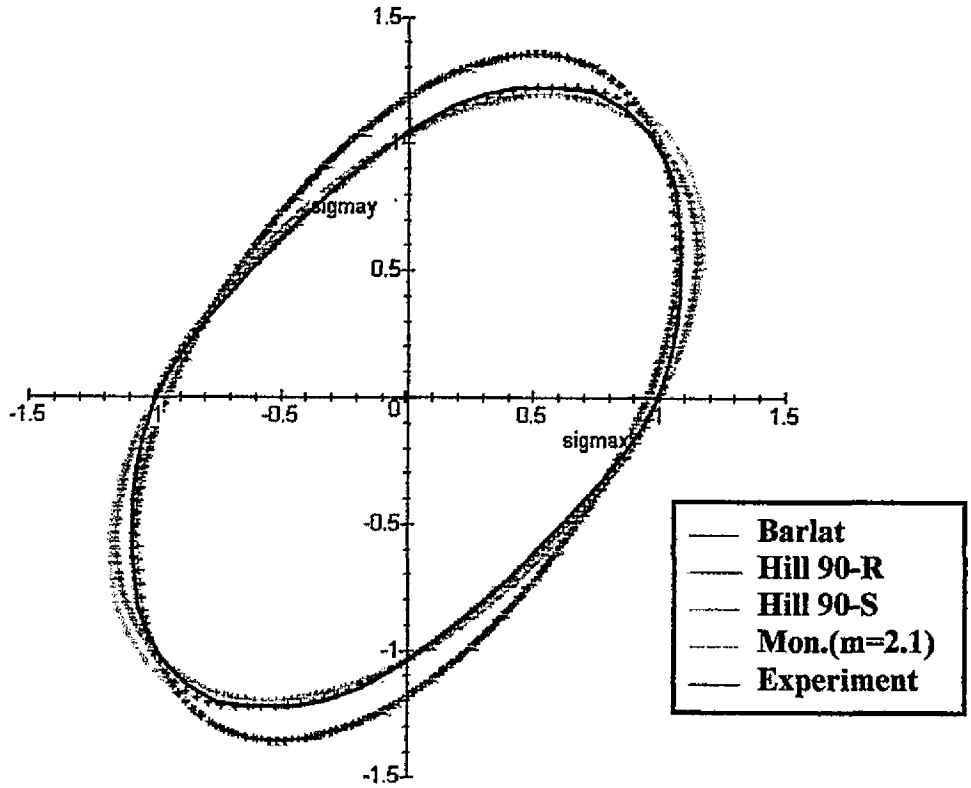

Stage 4

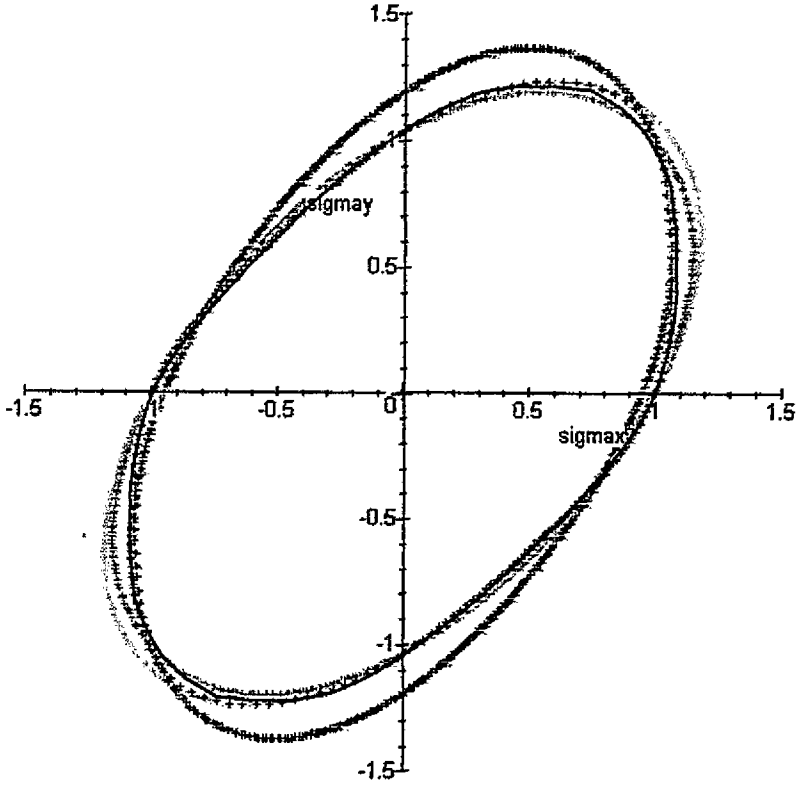

Stage 5

Figure 6.5 Comparison of the Normalized Yield Loci with a Shear Stress Term (Cont'd)

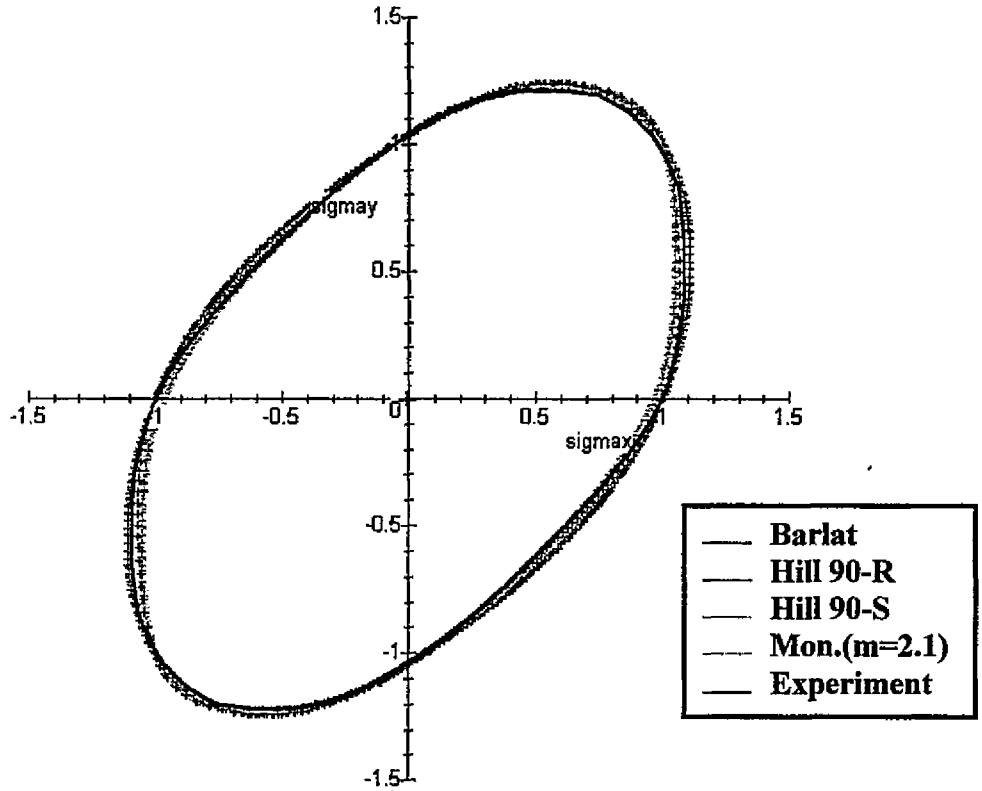

Stage 2

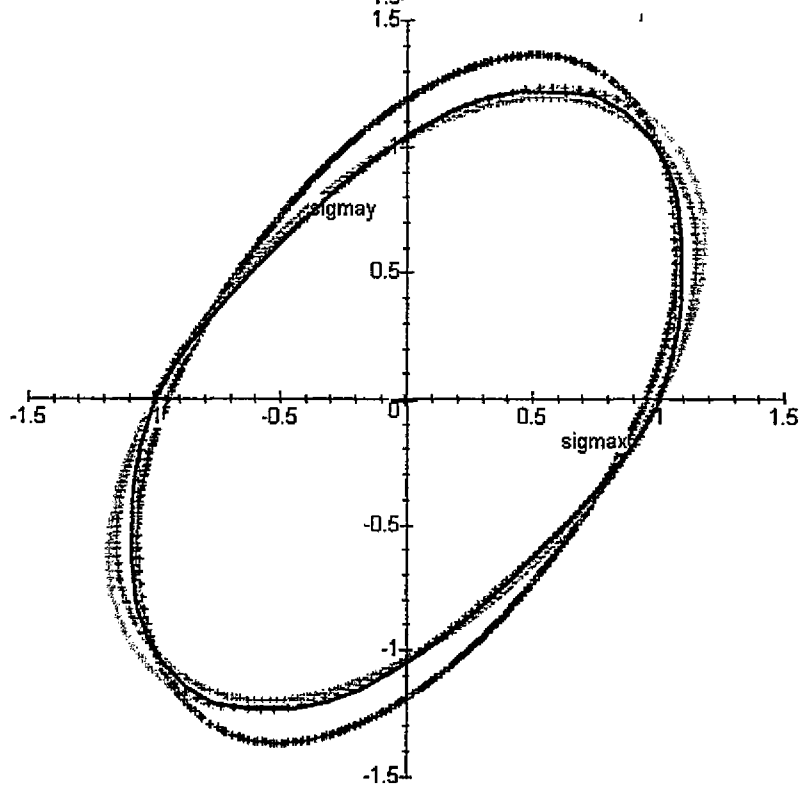

Stage 3

Figure 6.5 Comparison of the Normalized Yield Loci with a Shear Stress Term (Cont'd)

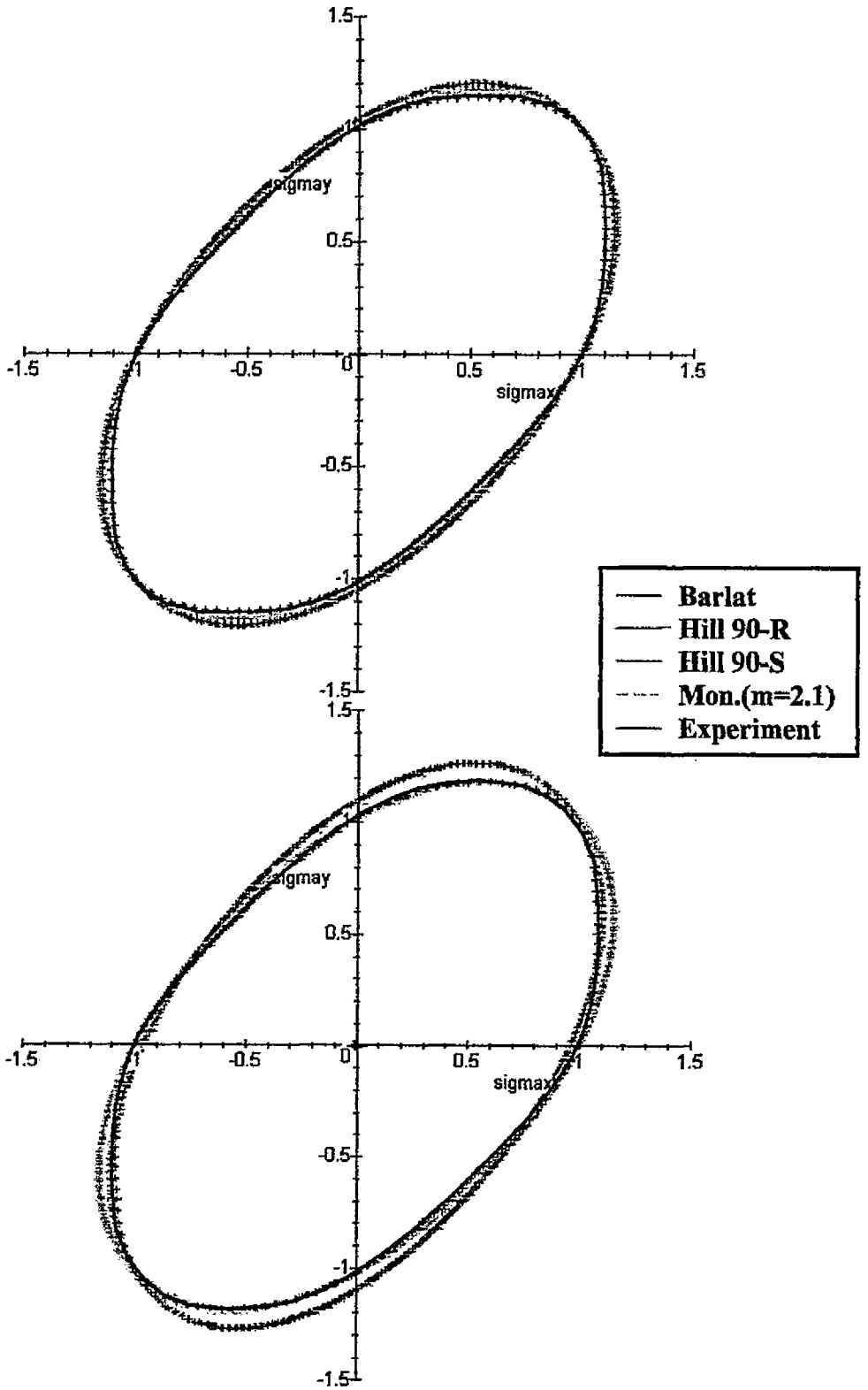

Stage 0

Stage 1

Figure 6.5 Comparison of the Normalized Yield Loci with a Shear Stress Term

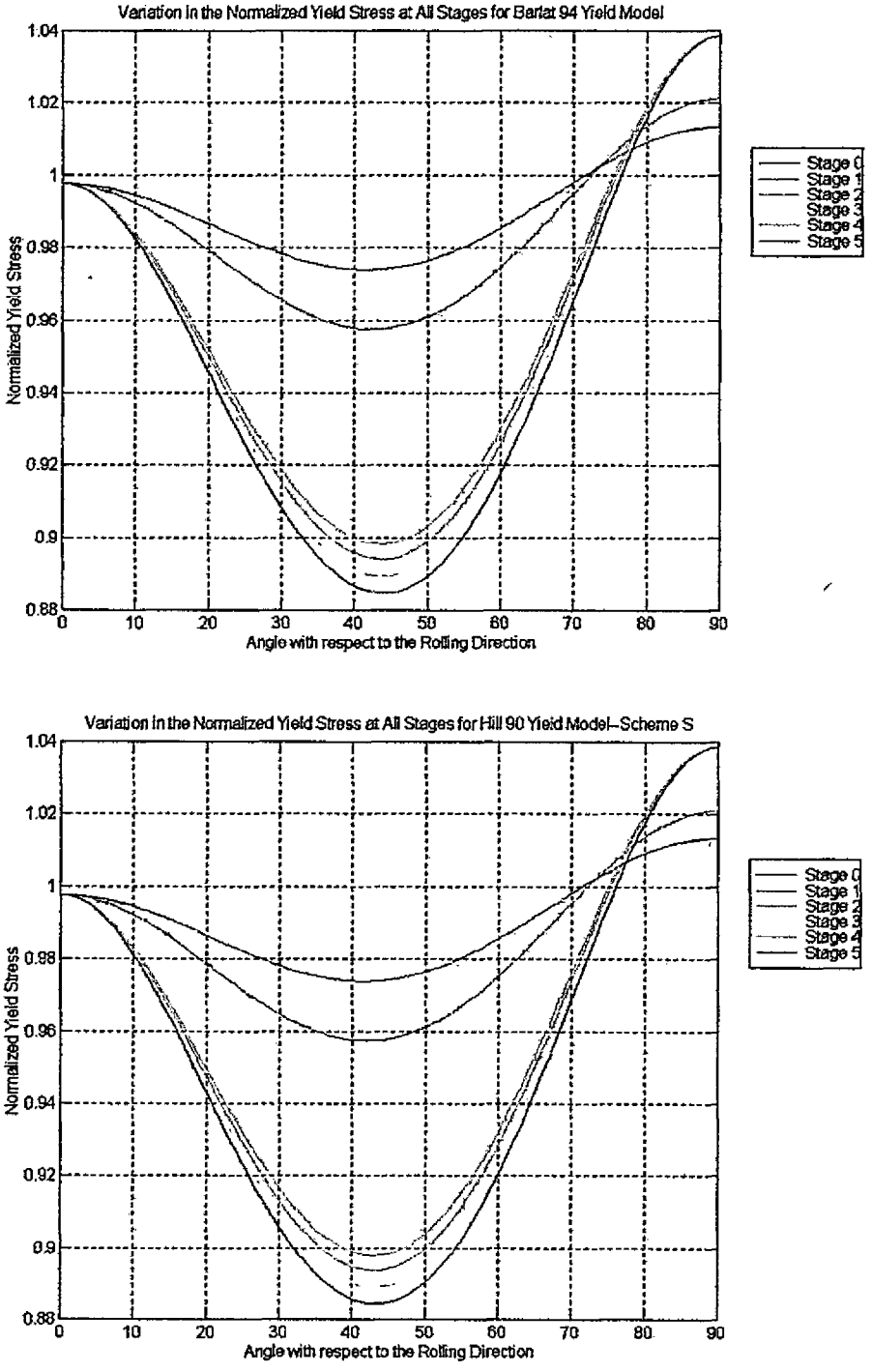

Figure 6.6 Variation in the Normalized Yield Stress with θ, for Different Yield Criteria

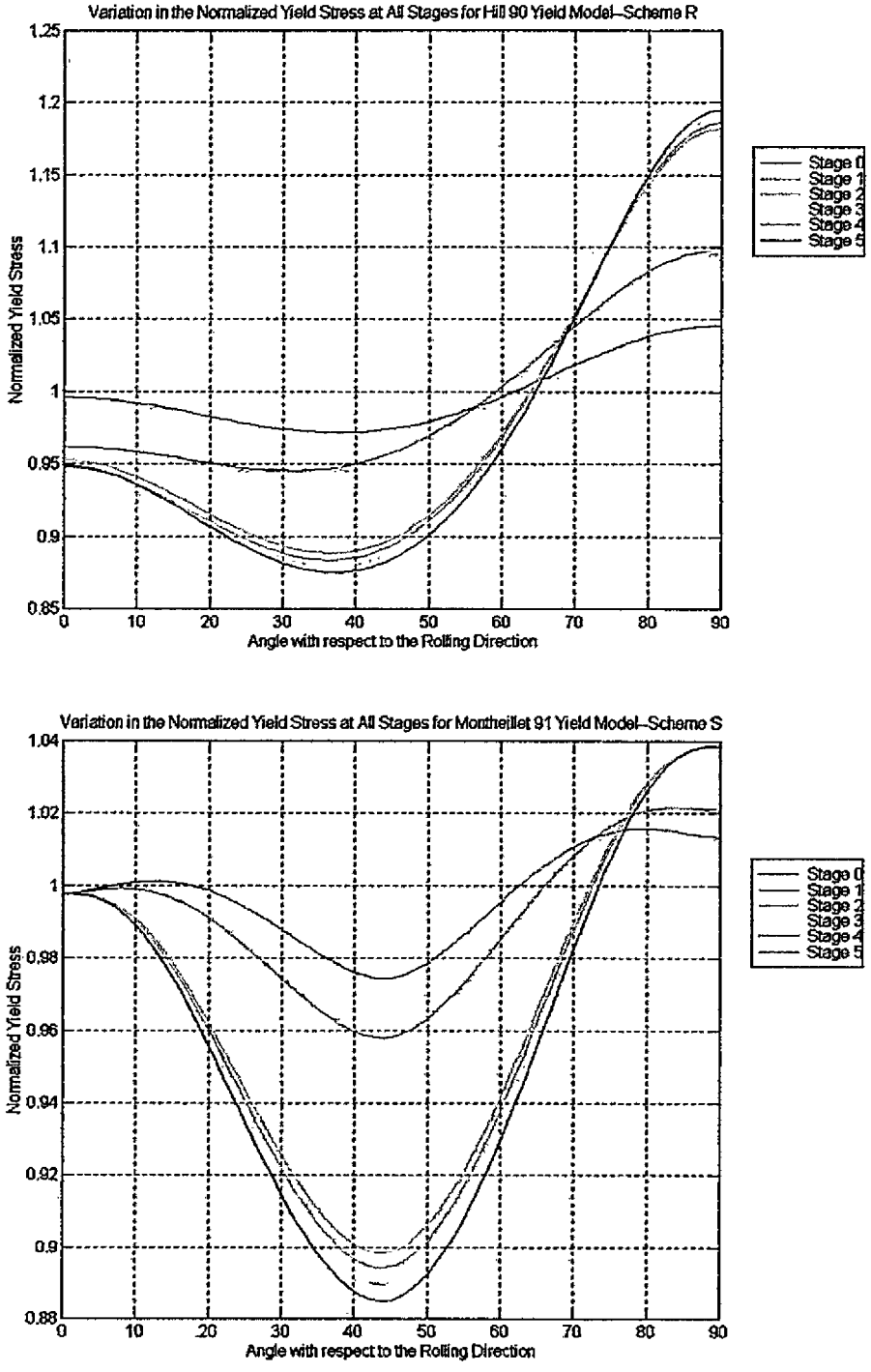

Figure 6.6 Variation in the Normalized Yield Stress with θ, for Different Yield Criteria (Continued)

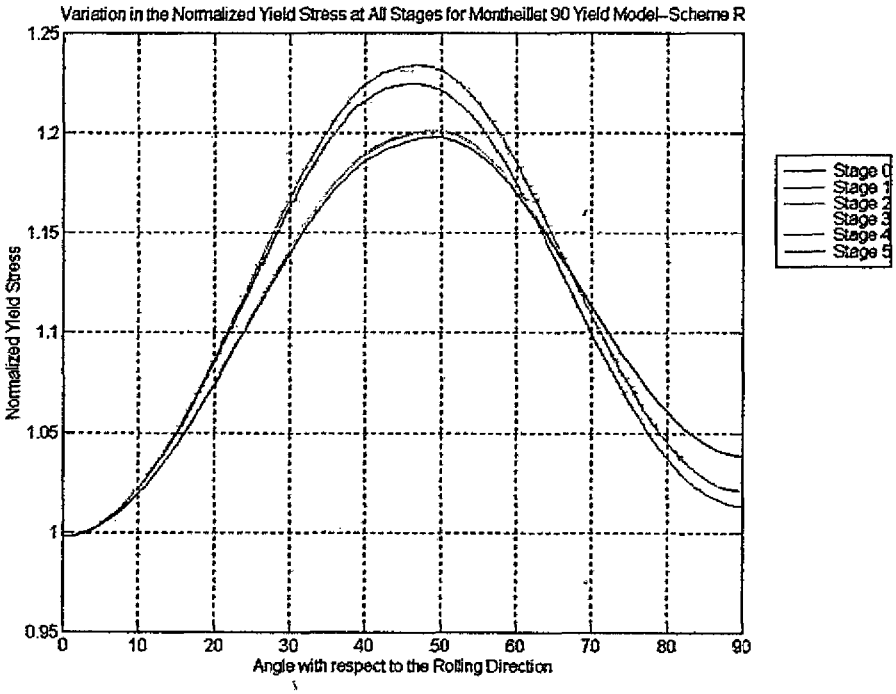

Figure 6.6 Variation in the Normalized Yield Stress with θ, for Different Yield Criteria (Continued)

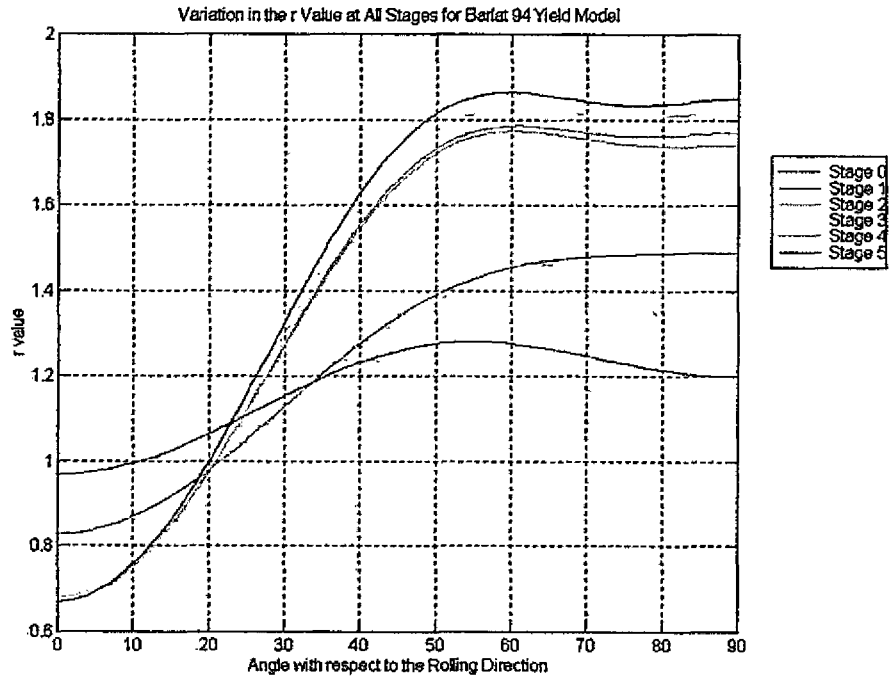

Figure 6.7 Variation in the r-value with θ, for Different Yield Criteria

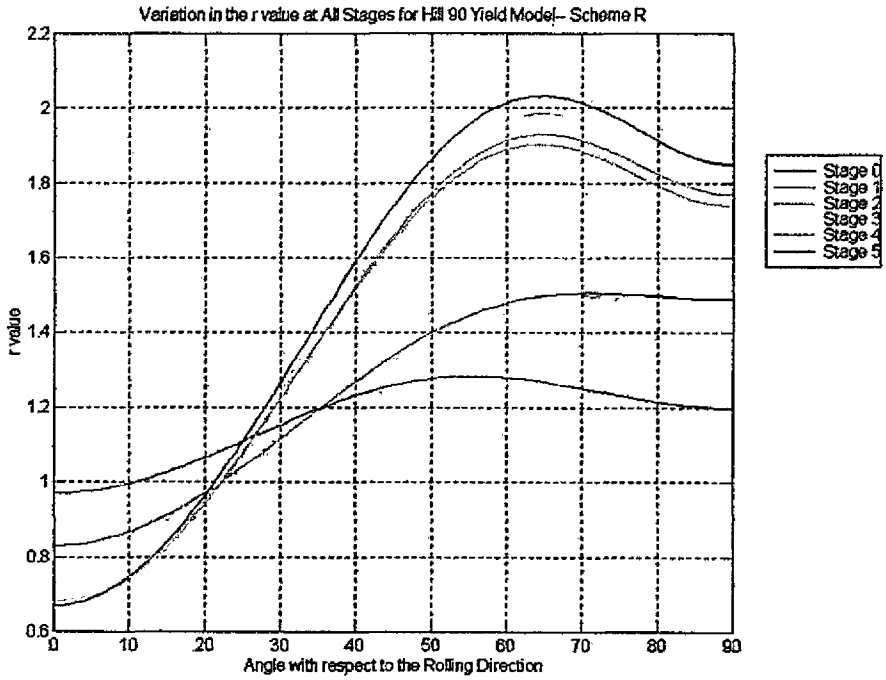

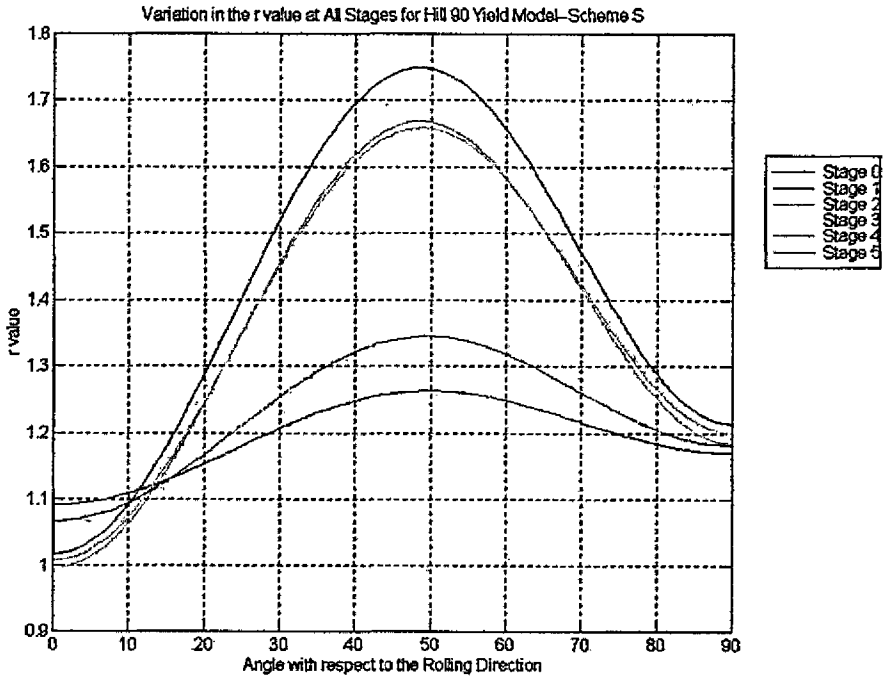

Figure 6.7 Variation in the r-value with θ, for Different Yield Criteria (Continued)

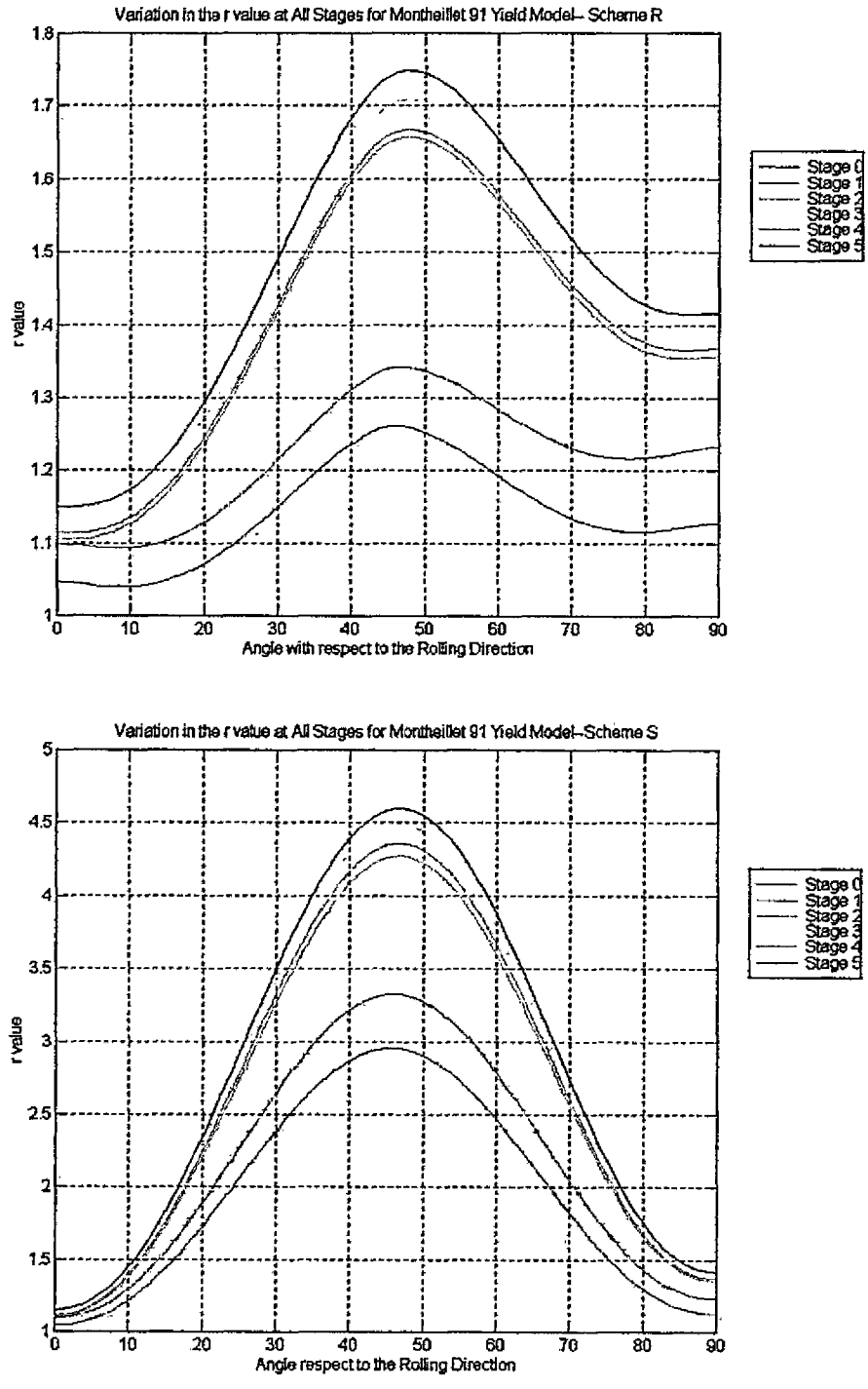

Figure 6.7 Variation in the r-value with θ, for Different Yield Criteria (Continued)

Table 6.7 Experimental and Theoretical Yield Stresses after each Deformation Stage

Stage 0	Normalized Yield Stress							
Angle (°)	Experiment	Barlat [38, 47-48]	Hill-r [63]	Hill-s [63]	Montheillet-r [61]	Montheillet-s [61]	Hill [65]	Hosford [50-52]
0.0	0.9978*	0.9978	0.9961	0.9978	0.9978	0.9978	0.9978	0.9858
22.5		0.9845	0.9805	0.9843	1.1038	0.9967		
45.0	0.9744**	0.9744	0.9744	0.9744	1.2243	0.9744		
67.5		0.9948	1.0132	0.9949	1.1190	1.0077		
90.0	1.0135*	1.0135	1.0459	1.0135	1.0135	1.0135	1.0135	1.0028

Stage 1	Normalized Yield Stress							
Angle (°)	Experiment	Barlat [38, 47-48]	Hill-r [63]	Hill-s [63]	Montheillet-r [61]	Montheillet-s [61]	Hill [65]	Hosford [50-52]
0.0	0.9978*	0.9978	0.9623	0.9978	0.9978	0.9978	0.9978	0.9734
22.5		0.9757	0.9489	0.9750	1.1061	0.9875		
45.0	0.9580**	0.9580	0.9580	0.9580	1.2334	0.9580		
67.5		0.9896	1.0348	0.9904	1.1289	1.0035		
90.0	1.0214*	1.0214	1.0983	1.0214	1.0214	1.0214	1.0214	1.0195

Stage 2	Normalized Yield Stress							
Angle (°)	Experiment	Barlat [38, 47-48]	Hill-r [63]	Hill-s [63]	Montheillet-r [61]	Montheillet-s [61]	Hill [65]	Hosford [50-52]
0.0	0.9978*	0.9978	0.9479	0.9978	0.9978	0.9978	0.9978	0.9685
22.5		0.9407	0.9042	0.9383	1.0918	0.9507		
45.0	0.8942**	0.8942	0.8942	0.8942	1.1992	0.8945		
67.5		0.9586	1.0311	0.9617	1.1297	0.9749		
90.0	1.0387*	1.0387	1.1861	1.0387	1.0387	1.0387	1.0387	1.0467

Stage 3	Normalized Yield Stress							
Angle (°)	Experiment	Barlat [38, 47-48]	Hill-r [63]	Hill-s [63]	Montheillet-r [61]	Montheillet-s [61]	Hill [65]	Hosford [50-52]
0.0	0.9978*	0.9978	0.9476	0.9978	0.9978	0.9978	0.9978	0.9673
22.5		0.9381	0.9014	0.9356	1.0916	0.9479		
45.0	0.8895**	0.8895	0.8895	0.8895	1.1985	0.8898		
67.5		0.9555	1.0292	0.9587	1.1294	0.9720		
90.0	1.0387*	1.0387	1.1908	1.0387	1.0387	1.0387	1.0387	1.0471

Stage 4	Normalized Yield Stress							
Angle (°)	Experiment	Barlat [38, 47-48]	Hill-r [63]	Hill-s [63]	Montheillet-r [61]	Montheillet-s [61]	Hill [65]	Hosford [50-52]
0.0	0.9978*	0.9978	0.9528	0.9978	0.9978	0.9978	0.9978	0.9690
22.5		0.9431	0.9092	0.9408	1.0915	0.9531		
45.0	0.8985**	0.8985	0.8985	0.8985	1.1984	0.8987		
67.5		0.9616	1.0323	0.9643	1.1293	0.9976		
90.0	1.0387*	1.0387	1.1827	1.0387	1.0387	1.0387	1.0387	1.0445

Stage 5	Normalized Yield Stress							
Angle (°)	Experiment	Barlat [38, 47-48]	Hill-r [63]	Hill-s [63]	Montheillet-r [61]	Montheillet-s [61]	Hill [65]	Hosford [50-52]
0.0	0.9978*	0.9978	0.9487	0.9978	0.9978	0.9978	0.9978	0.9967
22.5		0.9355	0.8994	0.9328	1.0905	0.9452		
45.0	0.8848**	0.8848	0.8848	0.8848	1.1952	0.8850		
67.5		0.9523	1.0269	0.9557	1.1282	0.9690		
90.0	1.0387*	1.0387	1.1949	1.0387	1.0387	1.0387	1.0387	1.0473

* Data are obtained from the Crystallographic Yield Loci provided by Queen's University.

** Data are taken from Barlat's [38, 47-48] Yield Criterion.

Table 6.8 Experimental and Theoretical r-values after each Deformation Stage

Stage 0	r-value							
Angle (°)	Experiment*	Barlat [38, 47-48]	Hill-r [63]	Hill-s [63]	Montheillet-r [61]	Montheillet-s [61]	Hill [65]	Hosford [50-52]
0.0	0.97	0.970	0.970	1.092	1.047	1.047	0.970	0.970
22.5		1.087	1.086	1.166	1.087	1.887		
45.0	1.26	1.260	1.260	1.260	1.260	2.958		
67.5		1.257	1.261	1.225	1.146	1.987		
90.0	1.20	1.200	1.200	1.171	1.128	1.128	1.200	1.200

Stage 1	r-value							
Angle (°)	Experiment*	Barlat [38, 47-48]	Hill-r [63]	Hill-s [63]	Montheillet-r [61]	Montheillet-s [61]	Hill [65]	Hosford [50-52]
0.0	0.83	0.830	0.830	1.066	1.099	1.099	0.830	0.830
22.5		1.015	1.004	1.188	1.145	2.069		
45.0	1.34	1.340	1.340	1.340	1.340	3.327		
67.5		1.477	1.505	1.278	1.242	2.241		
90.0	1.49	1.490	1.490	1.182	1.234	1.234	1.490	1.490

Stage 2	r-value							
Angle (°)	Experiment*	Barlat [38, 47-48]	Hill-r [63]	Hill-s [63]	Montheillet-r [61]	Montheillet-s [61]	Hill [65]	Hosford [50-52]
0.0	0.67	0.670	0.670	0.996	1.115	1.115	0.670	0.670
22.5		1.045	1.005	1.296	1.286	2.500		
45.0	1.66	1.660	1.660	1.660	1.660	4.349		
67.5		1.776	1.926	1.463	1.485	2.880		
90.0	1.77	1.770	1.770	1.185	1.369	1.369	1.770	1.770

Stage 3	r-value							
Angle (°)	Experiment*	Barlat [38, 47-48]	Hill-r [63]	Hill-s [63]	Montheillet-r [61]	Montheillet-s [61]	Hill [65]	Hosford [50-52]
0.0	0.67	0.670	0.670	1.007	1.137	1.137	0.670	0.670
22.5		1.061	1.018	1.321	1.315	2.569		
45.0	1.70	1.700	1.700	1.700	1.700	4.481		
67.5		1.816	1.983	1.492	1.520	2.965		
90.0	1.82	1.820	1.820	1.199	1.399	1.399	1.820	1.820

Stage 4	r-value							
Angle (°)	Experiment*	Barlat [38, 47-48]	Hill-r [63]	Hill-s [63]	Montheillet-r [61]	Montheillet-s [61]	Hill [65]	Hosford [50-52]
0.0	0.68	0.680	0.680	1.007	1.107	1.107	0.680	0.680
22.5		1.047	1.011	1.297	1.277	2.458		
45.0	1.65	1.650	1.650	1.650	1.650	4.264		
67.5		1.762	1.898	1.466	1.474	2.830		
90.0	1.74	1.740	1.740	1.201	1.357	1.357	1.740	1.740

Stage 5	r-value							
Angle (°)	Experiment*	Barlat [38, 47-48]	Hill-r [63]	Hill-s [63]	Montheillet-r [61]	Montheillet-s [61]	Hill [65]	Hosford [50-52]
0.0	0.67	0.670	0.670	1.017	1.150	1.150	0.670	0.670
22.5		1.078	1.032	1.345	1.339	2.624		
45.0	1.74	1.740	1.740	1.740	1.740	4.590		
67.5		1.849	2.028	1.521	1.550	3.031		
90.0	1.85	1.850	1.850	1.214	1.417	1.417	1.850	1.850

* Data are obtained from the Crystallographic Yield Loci provided by Queen's University.

increasing reduction, and it was possible to establish a work hardening curve for the material. In a similar manner the hardness of the material increases with reduction and an empirical relationship between the hardness number and the deformation strain could be established.

The texture measurements were performed by researchers at the Los Alamos National Laboratories, who also had the necessary software to predict the texture evolution by simulating the deformation mode of the steel sheet as it passed through the roll stands. However, to keep the experimental measurements and the theoretical predictions separate it was decided to let researchers at Queen's University deal with the analysis using a software package developed by van Houtte.

As described in the text the approach involved CODF analysis based on the following, a) measured pole figures for the as-received material b) an assumed deformation mode in each roll stand c) an assumed crystallographic slip system, and d) some measured mechanical properties. It turned out that the measured and predicted pole figures showed very good agreement, and therefore established the predictive capabilities of the computer software. In addition to predicting the texture evolution, CODF analysis permits the prediction of the corresponding plane stress crystallographic yield loci as well as the variation in the normalized yield stress and the r-value in the plane of the rolled sheet.

A great deal of effort was devoted to establishing a reliable anisotropic yield function, which could be used when modelling a variety of deformation processes. The work due to Barlat and his co-workers seemed very promising, although many of the

details that were required to develop the models were not given in the original publications. Consequently, the present author went through the steps originally performed by Barlat when deriving his yield function. The development of algorithms in order to obtain various coefficients in the yield functions, along with programs to facilitate the plotting of the crystallographic yield loci, the author regards as original contributions. Under normal circumstances the coefficients in the analytical yield functions would be determined from mechanical property data e.g. r_0, r_{45}, σ_0 and σ_{90} etc., as explained in the text. However, this information was not available, and theoretical values from the CODF analysis performed at Queen's University were used instead. These data are referred to in the text as pseudo-experimental.

It turned out that Barlat's yield model could reproduce with good accuracy the crystallographic yield loci produced by the researchers at Queen's University, and therefore some confidence can be placed in its predictive capabilities. In his original investigations Barlat worked primarily with aluminum alloys, as opposed to steel in the present study. As a further check on the accuracy of Barlat's model a number of other anisotropic yield functions were compared. As explained in the text, some of these plane stress yield functions could accommodate an applied shear stress while others could not. Barlat's model was the most effective in predicting not only the crystallographic yield loci, but also the variation in the normalized yield stress and the r-value in the plane of the rolled sheet.

In the present study, results from the metallographic examinations in the scanning electron microscope showed little evidence of macroscopic shear banding often seen in

heavily cold rolled metals. However, coarse slip bands did exist and their number increased with deformation.

7.2 Recommendations for Future Work

As mentioned above, only one rolling schedule was examined and ductility in a tensile test is exhausted after material passes through the first stand. Hence these limited some explorations of this study, i.e. no alternation of rolling schedules, and front and back tensions. Also more than one source of texture measurement and of predicted results (pole figures, yield loci and r-values) would have been desirable for comparative purposes. For those readers interested in the present topic, the following are recommended for future work. We could try different roll stand reductions, and front and back tensions to see what effect these would have on the resulting texture (however, the present author doubts the effect of front and back tensions on texture development [103-105]; their major influence would be to reduce the roll force at each stand without having a major effect on the macroscopic deformation mode). The selected operative slip systems in this work were 5 of 24 {110}<111> +{112}<111> slip systems; but the author did not know which five of them were chosen. We could check the algorithms that some of the commercially available software packages employ and see how they select the operative slip systems. Other things are to examine different materials (say aluminum alloys), measure their yield stresses and r-values from tensile tests, and calculate the yield loci using Barlat's the newest function [48]. We could also compare all these results with those measured or predicted results obtained from texture measurement or simulation.

Appendix A

Plotting a Plane Stress Yield Locus with and without the Presence of the Shear Stress σ_{xy}

The purpose of this appendix is to delineate the steps involved in plotting a normalized, plane-stress, yield locus with and without the presence of the shear stress σ_{xy}.

No σ_{xy} acting, see Section 3.2.1

Select m, set α_z=1 and calculate the α and c coefficients as described in Section 3.2.1.1. Define normalized stress components in accordance with Fig 3.2 and equation (3.13), i.e.

$$\left.\begin{aligned}\frac{\sigma_{xx}}{\overline{\sigma}} &= \sigma\cos\theta_1\\ \frac{\sigma_{yy}}{\overline{\sigma}} &= \sigma\sin\theta_1\end{aligned}\right\} \qquad (A.1)$$

From (3.4) calculate the components of the modified stress tensor with σ_{zz}=0

$$\left.\begin{aligned}s_{xx} &= [(c_3+c_2)\sigma_{xx} - c_3\sigma_{yy}]/3\\ s_{yy} &= [-c_3\sigma_{xx} + (c_3+c_1)\sigma_{yy}]/3\\ s_{zz} &= -[c_2\sigma_{xx} + c_1\sigma_{yy}]/3\end{aligned}\right\} \qquad (A.2)$$

Substitute (A.1) into the above to obtain

$$\left.\begin{aligned}s_{xx} &= \sigma\overline{\sigma}[(c_3+c_2)\cos\theta_1 - c_3\sin\theta_1]/3\\ &= \sigma\overline{\sigma}a\ (\text{say})\\ &\text{Likewise,}\\ s_{yy} &= \sigma\overline{\sigma}[-c_3\cos\theta_1 + (c_3+c_1)\sin\theta_1]/3 = \sigma\overline{\sigma}b\\ s_{zz} &= \sigma\overline{\sigma}[-c_2\cos\theta_1 - c_1\sin\theta_1]/3 = \sigma\overline{\sigma}c\end{aligned}\right\} \qquad (A.3)$$

σ_{xy} present, see Section 3.2.2

Select m, set α_z=1 and calculate the α and c coefficients as described in Sections 3.2.1.1 and 3.2.2. Define normalized stress components in accordance with Fig 3.3 and equation (3.26), i.e.

$$\left.\begin{aligned}\frac{\sigma_{xx}}{\overline{\sigma}} &= \sigma\cos\theta_1\cos\theta_2\\ \frac{\sigma_{yy}}{\overline{\sigma}} &= \sigma\sin\theta_1\cos\theta_2\\ \frac{\sigma_{xy}}{\overline{\sigma}} &= \sigma\sin\theta_2\end{aligned}\right\} \qquad (A.A.1)$$

From (3.18) calculate the components of the modified stress tensor with σ_{yz}=σ_{zx}=0

$$\left.\begin{aligned}s_{xx} &= [c_3(\sigma_{xx}-\sigma_{yy}) + c_2\sigma_{xx}]/3\\ s_{yy} &= [c_1\sigma_{yy} - c_3(\sigma_{xx}-\sigma_{yy})]/3\\ s_{zz} &= -[c_2\sigma_{xx} + c_1\sigma_{yy}]/3\\ s_{yz} &= 0\\ s_{zx} &= 0\\ s_{xy} &= c_6\sigma_{xy}\end{aligned}\right\} \qquad (A.A.2)$$

Substitute (A.A.1) into the above to obtain

Now substitute (A.3) into the yield function (3.1), i.e.

$$\phi = \alpha_x |\sigma\bar{\sigma}b - \sigma\bar{\sigma}c|^m + \alpha_y |\sigma\bar{\sigma}c - \sigma\bar{\sigma}a|^m + \alpha_z |\sigma\bar{\sigma}a - \sigma\bar{\sigma}b|^m = 2\bar{\sigma}^m \quad \text{(A.4)}$$

The above can be rearranged as follows

$$\phi/\bar{\sigma}^m = \sigma^m(\alpha_x|b-c|^m + \alpha_y|c-a|^m + \alpha_z|a-b|^m) = 2 \quad \text{(A.5)}$$

Hence

$$\sigma = [2/(\alpha_x|b-c|^m + \alpha_y|c-a|^m + \alpha_z|a-b|^m)]^{1/m} \quad \text{(A.6)}$$

The quantities $\alpha_x|b-c|^m$ etc depend only on the known α and c coefficients, and the components of the unit vector **u**, i.e. $\cos\theta_1$ and $\sin\theta_1$. For simplicity (A.6) can be written as

$$\sigma = \left(\frac{2}{f(\mathbf{u})}\right)^{\frac{1}{m}}, \quad \text{(A.7)}$$

where $f(\mathbf{u})$ is a function of $\cos\theta_1$ and $\sin\theta_1$, along with the fixed values of the α and c coefficients. From (A.1) and (A.7) it follows that

$$\left.\begin{aligned} \sigma_{xx}/\bar{\sigma} &= \left(\frac{2}{f(\mathbf{u})}\right)^{\frac{1}{m}} \cos\theta_1 \\ \sigma_{yy}/\bar{\sigma} &= \left(\frac{2}{f(\mathbf{u})}\right)^{\frac{1}{m}} \sin\theta_1 \end{aligned}\right\} \quad \text{(A.8)}$$

See (3.17).

$$\left.\begin{aligned} s_{xx} &= \sigma\bar{\sigma}\cos\theta_2[(c_3+c_2)\cos\theta_1 - c_3\sin\theta_1]/3 \\ &= \sigma\bar{\sigma}a(\text{say}) \\ &\text{Likewise,} \\ s_{yy} &= \sigma\bar{\sigma}\cos\theta_2[-c_3\cos\theta_1 + (c_3+c_1)\sin\theta_1]/3 = \sigma\bar{\sigma}b \\ s_{zz} &= \sigma\bar{\sigma}\cos\theta_2[-c_2\cos\theta_1 - c_1\sin\theta_1]/3 = \sigma\bar{\sigma}c \\ s_{yz} &= 0 \\ s_{zx} &= 0 \\ s_{xy} &= \sigma\bar{\sigma}c_6\sin\theta_2 = \sigma\bar{\sigma}d \end{aligned}\right\} \quad \text{(A.A.3)}$$

Now substitute (A.A.3) into the characteristic equation (3.19) i.e.

$$\begin{vmatrix} \sigma\bar{\sigma}a - s & \sigma\bar{\sigma}d & 0 \\ \sigma\bar{\sigma}d & \sigma\bar{\sigma}b - s & 0 \\ 0 & 0 & \sigma\bar{\sigma}c - s \end{vmatrix} = 0 \quad \text{(A.A.4)}$$

Compute the above to obtain the eigen values s_k

$$\left.\begin{aligned} s_1 &= \sigma\bar{\sigma}\{(a+b) + [(a-b)^2 + 4d^2]^{1/2}\}/2 \\ &= \sigma\bar{\sigma}\Lambda_1(\text{say}) \\ &\text{Similarly,} \\ s_2 &= \sigma\bar{\sigma}\{(a+b) - [(a-b)^2 + 4d^2]^{1/2}\}/2 \\ &= \sigma\bar{\sigma}\Lambda_2 \\ s_3 &= \sigma\bar{\sigma}c \\ &= \sigma\bar{\sigma}\Lambda_3 \end{aligned}\right\} \quad \text{(A.A.5)}$$

Define the eigen vectors $\mathbf{v_k}$ with (3.21) i.e.

$$(\mathbf{s} - s_k\mathbf{I})\,\mathbf{v_k} = \mathbf{0} \quad \text{(A.A.6)}$$

Substitute (A.A.5) into the above to obtain

$$(\sigma\bar{\sigma})^3 \begin{bmatrix} a-c & d & 0 \\ d & b-c & 0 \\ 0 & 0 & c-c \end{bmatrix} \begin{bmatrix} v_{x3} \\ v_{y3} \\ v_{z3} \end{bmatrix} = \begin{bmatrix} 0 \\ 0 \\ 0 \end{bmatrix} \quad \text{(A.A.7)}$$

Since $v_{z3} \neq 0$,

$$\left.\begin{aligned} \mathbf{v}_3 &= \begin{bmatrix} 0 & 0 & 1 \end{bmatrix}^T \\ &\text{Likewise,} \\ \mathbf{v}_2 &= \begin{bmatrix} \frac{\Lambda_2 - b}{d} & 1 & 0 \end{bmatrix}^T \\ \mathbf{v}_1 &= \begin{bmatrix} \frac{\Lambda_1 - b}{d} & 1 & 0 \end{bmatrix}^T \end{aligned}\right\} \qquad \text{(A.A.8)}$$

From the Gram-Schmidt process

$$\left.\begin{aligned} \mathbf{p}_3 &= \frac{\mathbf{v}_3}{\|\mathbf{v}_3\|} \\ \mathbf{p}_2 &= \frac{\mathbf{v}_2 - \frac{\langle \mathbf{v}_2, \mathbf{p}_3 \rangle}{\|\mathbf{p}_3\|^2} \mathbf{p}_3}{\left\| \mathbf{v}_2 - \frac{\langle \mathbf{v}_2, \mathbf{p}_3 \rangle}{\|\mathbf{p}_3\|^2} \mathbf{p}_3 \right\|} \\ \mathbf{p}_1 &= \frac{\mathbf{v}_1 - \frac{\langle \mathbf{v}_1, \mathbf{p}_3 \rangle}{\|\mathbf{p}_3\|^2} \mathbf{p}_3 - \frac{\langle \mathbf{v}_1, \mathbf{p}_2 \rangle}{\|\mathbf{p}_2\|^2} \mathbf{p}_2}{\left\| \mathbf{v}_1 - \frac{\langle \mathbf{v}_1, \mathbf{p}_3 \rangle}{\|\mathbf{p}_3\|^2} \mathbf{p}_3 - \frac{\langle \mathbf{v}_1, \mathbf{p}_2 \rangle}{\|\mathbf{p}_2\|^2} \mathbf{p}_2 \right\|} \end{aligned}\right\} \qquad \text{(A.A.9)}$$

compute the principal stress directions $\mathbf{p}_k$ using $\mathbf{v}_k$ from (A.A.8)

$$p_1 = \frac{\begin{bmatrix} \{\Lambda_1 - b + \frac{(a+b)(\Lambda_2 - b)}{2[(a-b)^2 + 4d^2]^{1/2}}\}/d \\ \frac{(a+b)}{2[(a-b)^2 + 4d^2]^{1/2}} + 1 \\ 0 \end{bmatrix}}{\sqrt{\{\{\Lambda_1 - b + \frac{(a+b)(\Lambda_2 - b)}{2[(a-b)^2 + 4d^2]^{1/2}}\}/d\}^2 + \{\frac{(a+b)}{2[(a-b)^2 + 4d^2]^{1/2}} + 1\}^2}}$$

$$p_2 = \begin{bmatrix} \frac{(\Lambda_2 - b)}{d} \\ 1 \\ 0 \end{bmatrix} \Bigg/ \sqrt{\left[\frac{(\Lambda_2 - b)}{d}\right]^2 + 1}$$

$$p_3 = \begin{bmatrix} 0 \\ 0 \\ 1 \end{bmatrix}$$

(A.A.10)

Substitute (A.A.10) into (3.23) to give

$$\left.\begin{aligned}
&\alpha_x\{\{\Lambda_1 - b + \frac{(a+b)(\Lambda_2 - b)}{2[(a-b)^2 + 4d^2]^{1/2}}\}/d\}^2 \\
&+ \alpha_y\{\frac{(a+b)}{2[(a-b)^2 + 4d^2]^{1/2}} + 1\}^2 \\
\alpha_1 = &\frac{}{\sqrt{\{\{\Lambda_1 - b + \frac{(a+b)(\Lambda_2 - b)}{2[(a-b)^2 + 4d^2]^{1/2}}\}/d\}^2 + \{\frac{(a+b)}{2[(a-b)^2 + 4d^2]^{1/2}} + 1\}^2}} \\
&\alpha_x\left[\frac{(\Lambda_2 - b)}{d}\right]^2 + \alpha_y \\
\alpha_2 = &\frac{}{\sqrt{\left[\frac{(\Lambda_2 - b)}{d}\right]^2 + 1}} \\
&\alpha_3 = \alpha_z
\end{aligned}\right\} \qquad \text{(A.A.11)}$$

Now substitute (A.A.3) into the yield function (3.22) i.e.

$$\Phi = \alpha_1|\sigma\bar{\sigma}\Lambda_2 - \sigma\bar{\sigma}\Lambda_3|^m + \alpha_2|\sigma\bar{\sigma}\Lambda_3 - \sigma\bar{\sigma}\Lambda_1|^m + \alpha_3|\sigma\bar{\sigma}\Lambda_1 - \sigma\bar{\sigma}\Lambda_2|^m = 2\bar{\sigma}^m \qquad \text{(A.A.12)}$$

The above can be rearranged as follows

$$\Phi/\bar{\sigma}^m = \sigma^m(\alpha_1|\Lambda_2 - \Lambda_3|^m + \alpha_2|\Lambda_3 - \Lambda_1|^m + \alpha_3|\Lambda_1 - \Lambda_2|^m) = 2 \qquad \text{(A.A13)}$$

Hence

$$\sigma = [2/(\alpha_1|\Lambda_2 - \Lambda_3|^m + \alpha_2|\Lambda_3 - \Lambda_1|^m + \alpha_3|\Lambda_1 - \Lambda_2|^m)]^{1/m} \qquad \text{(A.A.14)}$$

The quantities $\alpha_1|\Lambda_2-\Lambda_3|^m + \alpha_2|\Lambda_3-\Lambda_1|^m + \alpha_3|\Lambda_1-\Lambda_2|^m$

depend simply on the known α and c coefficients, and the components of the unit vector **u**, i.e. $\cos\theta_1\cos\theta_2$, $\sin\theta_1\cos\theta_2$ and $\sin\theta_2$. For simplicity equation (A.A.14) can be written as

$$\sigma = \left(\frac{2}{F(\mathbf{u})}\right)^{\frac{1}{m}} \qquad \text{(A.A.15)}$$

where $F(\mathbf{u})$ is a function of $\cos\theta_1$, $\cos\theta_2$, $\sin\theta_1$ and $\sin\theta_2$ along with the fixed values of the α_x, α_y, α_z, and c coefficients. Now substitute for σ from (A.A.1) to obtain

$$\left.\begin{aligned} \sigma_{xx}/\overline{\sigma} &= \left(\frac{2}{F(\mathbf{u})}\right)^{\frac{1}{m}} \cos\theta_1\cos\theta_2 \\ \sigma_{yy}/\overline{\sigma} &= \left(\frac{2}{F(\mathbf{u})}\right)^{\frac{1}{m}} \sin\theta_1\cos\theta_2 \\ \sigma_{xy}/\overline{\sigma} &= \left(\frac{2}{F(\mathbf{u})}\right)^{\frac{1}{m}} \sin\theta_2 \end{aligned}\right\} \qquad \text{(A.A.16)}$$

See (3.28).

Appendix B

Confirmation of the Value $(\sigma_{xy})_Y$

Perform a tensile test in a direction at 45° to the rolling direction and measure the yield stress, σ_{45}. The stress is then transformed to the x, y directions to yield the following components

$$\sigma_{xx} = \sigma_{yy} = \sigma_{xy} = \sigma_{45}/2 \tag{B.1}$$

Now substitute into (3.18) to obtain the components s_{xx}, s_{yy}, s_{zz} and s_{xy}. Obtain the eigen (principal stress) values s_{11} etc and the eigen vectors (principal directions) $\mathbf{p}_k$ as described by (3.19) through (3.21). Substitute s_{11} etc into (3.22) and use (3.23) to evaluate α_1, α_2 and α_3, where $\alpha_3=\alpha_z=1$. From (3.22) it is possible to express the ratio $\sigma_{45}/\bar{\sigma}$ as a function of the α and c coefficients and the exponent m.

From the flow rule the principal strain increments $d\varepsilon_{11}$ etc can be expressed as

$$\left.\begin{aligned} d\varepsilon_{11} &= \lambda \partial\Phi / \partial s_{11} \\ d\varepsilon_{22} &= \lambda \partial\Phi / \partial s_{22} \\ d\varepsilon_{33} &= \lambda \partial\Phi / \partial s_{33} \end{aligned}\right\} \tag{B.2}$$

Now transform these strains to the material reference frame (x, y, z) using the transformation tensor **p** in the following manner

$$de_{ij} = p_{i\alpha} p_{j\beta} d\varepsilon_{\alpha\beta} \qquad \left.\begin{aligned} i,j &= x,y,z \\ \alpha,\beta &= 1,2,3 \end{aligned}\right\} \tag{B.3}$$

For example,

$$\left.\begin{aligned} de_{xy} &= \lambda(p_{x1}p_{y1}d\varepsilon_{11} + p_{x2}p_{y2}d\varepsilon_{22} + p_{x3}p_{y3}d\varepsilon_{33}) \\ de_{xx} &= \lambda(p_{x1}{}^2 d\varepsilon_{11} + p_{x2}{}^2 d\varepsilon_{22} + p_{x3}{}^2 d\varepsilon_{33}) \end{aligned}\right\} \qquad (B.4)$$

with similar expressions for de_{yy} and de_{zz}. Once having the strain increment components in the x, y, z frame they need to be modified through the operator **L** in the same way as the stresses, see (3.2). The c components in **L** are unchanged from (3.3) but now $c_4=c_5=0$. It follows that

$$(\mathbf{dE}) = \mathbf{L}\,(\mathbf{de}) \qquad (B.5)$$

where **dE** represent the modified strain increments dE_{xx} etc. The strain increment components dE_{xx} can now be transformed to the 45° direction. Let d(A,A) be the strain component along the 45°direction, d(B,B) the transverse strain and d(C,C) the through thickness strain. Hence

$$\left.\begin{aligned} d(A,A) &= \cos^2 45 dE_{xx} + \sin^2 45 dE_{yy} + 2\sin 45\cos 45 dE_{xy} \\ d(B,B) &= \sin^2 45 dE_{xx} + \cos^2 45 dE_{yy} - 2\sin 45\cos 45 dE_{xy} \\ d(C,C) &= dE_{zz} \end{aligned}\right\} \qquad (B.6)$$

or

$$\left.\begin{aligned} d(A,A) &= dE_{xx}/2 + dE_{yy}/2 + dE_{xy} \\ d(B,B) &= dE_{xx} + dE_{yy}/2 - dE_{xy} \\ d(C,C) &= dE_{zz} \end{aligned}\right\} \qquad (B.7)$$

The r-value at 45° is given by

$$r_{45} = d(B,B)/dE_{zz} \qquad (B.8)$$

Everything cancels in the strain ratio other than the α and c coefficients and the exponent m. Hence the r_{45} value can be calculated and if it does not agree with the experimental

value then the value of $(\sigma_{xy})_y$ in (3.25) can be adjusted, and the theoretical r_{45} value recalculated with the new value of c_6.

Appendix C

A General Program Written in MATLAB for Evaluating

Barlat's 94 Yield Criterion

```
% Clear off all the data in memory.
clear all;


% Input data.
M=input('Please enter the exponent for six component yield locus 94: ');
X1=input('Please enter the yield stress in rolling direction: ');
X2=input('Please enter the yield stress in transverse direction: ');
X3=input('Please enter the yield stress in through-thickness direction: ');
Eff=input('Please enter the effective stress: ');
R0=input('Please enter the r-value in rolling direction: ');
R90=input('Please enter the r-value in transverse direction: ');


% Given each stress stage, the associated yield equations are obtained.
f1='alphax*abs(c2-c3)^m+alphay*abs(2*c2+c3)^m+alphaz*abs(c2+2*c3)^m-
2*(3*sigma/x1)^m';
f2='alphax*abs(c3+2*c1)^m+alphay*abs(c3-c1)^m+alphaz*abs(2*c3+c1)^m-
2*(3*sigma/x2)^m';
f3='alphax*abs(2*c1+c2)^m+alphay*abs(c1+2*c2)^m+alphaz*abs(c1-c2)^m-
2*(3*sigma/x3)^m';


% R value's calculation for r0 and r90 theoretically by using flow rule.
fr0='(alphax*(c2-c3)*abs(c2-c3)^(m-2)*(c3+2*c1)+alphay*(-c3-
2*c2)*abs(c3+2*c2)^(m-2)*(c3-c1)+alphaz*(2*c3+c2)*abs(2*c3+c2)^(m-2)*(-2*c3-
c1))/(alphax*(c2-c3)*abs(c2-c3)^(m-2)*(-2*c1-c2)+alphay*(-c3-
2*c2)*abs(c3+2*c2)^(m-2)*(c1+2*c2)+alphaz*(2*c3+c2)*abs(2*c3+c2)^(m-2)*(c1-
c2))-r0';
fr90='(alphax*(c3+2*c1)*abs(c3+2*c1)^(m-2)*(c2-c3)+alphay*(c3-c1)*abs(c3-c1)^(m-
2)*(-c3-2*c2)+alphaz*(-2*c3-c1)*abs(2*c3+c1)^(m-
2)*(2*c3+c2))/(alphax*(c3+2*c1)*abs(c3+2*c1)^(m-2)*(-2*c1-c2)+alphay*(c3-
c1)*abs(c3-c1)^(m-2)*(c1+2*c2)+alphaz*(-2*c3-c1)*abs(2*c3+c1)^(m-2)*(c1-c2))-r90';
```

```
% Wild guess the arbitrary alpha_z to start iteration.
AlphaZ=input('Please enter the alpha_z for iteration: ');
% Substitute numerical values into those symbolic equations above.
g1=subs(f1,M,'m');g1=subs(g1,X1,'x1');g1=subs(g1,Eff,'sigma');g1=subs(g1,AlphaZ,'alph
az');
g2=subs(f2,M,'m');g2=subs(g2,X2,'x2');g2=subs(g2,Eff,'sigma');g2=subs(g2,AlphaZ,'alph
az');
g3=subs(f3,M,'m');g3=subs(g3,X3,'x3');g3=subs(g3,Eff,'sigma');g3=subs(g3,AlphaZ,'alph
az');
g4=subs(fr0,M,'m');g4=subs(g4,R0,'r0');g4=subs(g4,AlphaZ,'alphaz');
g5=subs(fr90,M,'m');g5=subs(g5,R90,'r90');g5=subs(g5,AlphaZ,'alphaz');


% Set up two symbolic matrix, g and c, for jacobian matrix, z.
g=sym(5,1,g5);g=sym(g,1,1,g1);g=sym(g,2,1,g2);g=sym(g,3,1,g3);g=sym(g,4,1,g4);
c=sym('[c1,c2,c3,alphax,alphay]');
z=jacobian(g,c);


% Set arbitrary c's and alpha's for initialization the Newton-Raphson method.
C1=1.00001;C2=1.00002;C3=1.00003;AX=1.00004;AY=1.00005;


% Substitute the above coefficients into C matrix.
C=[C1,C2,C3,AX,AY]';


% Start-up value for reduction of errors.
delta=1;


% Newton-Raphson method
while delta>1e-12
   C=[C1,C2,C3,AX,AY]';


   % Substitute numerical values into the symbolic equation g.
Gs=subs(g,C1,'c1');Gs=subs(Gs,C2,'c2');Gs=subs(Gs,C3,'c3');Gs=subs(Gs,AX,'alphax');
Gs=subs(Gs,AY,'alphay');

    % Numerize G.
    G=numeric(Gs);
```

```
    % Substitute numerical values into the symbolic equations Zs'.
Zs1=subs(z(1,:),C1,'c1');Zs1=subs(Zs1,C2,'c2');Zs1=subs(Zs1,C3,'c3');Zs1=subs(Zs1,AX
,'alphax');Zs1=subs(Zs1,AY,'alphay');
Zs2=subs(z(2,:),C1,'c1');Zs2=subs(Zs2,C2,'c2');Zs2=subs(Zs2,C3,'c3');Zs2=subs(Zs2,AX
,'alphax');Zs2=subs(Zs2,AY,'alphay');

Zs3=subs(z(3,:),C1,'c1');Zs3=subs(Zs3,C2,'c2');Zs3=subs(Zs3,C3,'c3');Zs3=subs(Zs3,AX
,'alphax');Zs3=subs(Zs3,AY,'alphay');

Zs4=subs(z(4,:),C1,'c1');Zs4=subs(Zs4,C2,'c2');Zs4=subs(Zs4,C3,'c3');Zs4=subs(Zs4,AX
,'alphax');Zs4=subs(Zs4,AY,'alphay');

Zs5=subs(z(5,:),C1,'c1');Zs5=subs(Zs5,C2,'c2');Zs5=subs(Zs5,C3,'c3');Zs5=subs(Zs5,AX
,'alphax');Zs5=subs(Zs5,AY,'alphay');

    % Numerize J.
    Z1=numeric(Zs1);
    Z2=numeric(Zs2);
    Z3=numeric(Zs3);
    Z4=numeric(Zs4);
    Z5=numeric(Zs5);
    J=[Z1;Z2;Z3;Z4;Z5];


    % Find five anistropic coefficients and error.
    D=-1*inv(J)*G;
    E=C+D;
    C1=E(1,1);C2=E(2,1);C3=E(3,1);AX=E(4,1);AY=E(5,1);
    delta=norm(D);
    AlphaX=AX;
    AlphaY=AY;

end
clc;


% Set the start-up values, Xshear, Xs1 and Xs2, for c6.
XsA=X1/2;
XsB=0;
XsC=0;
```

```
% For plotting shear stress, calculate c6 from experimental normalised sigma_45 or r45.
disp('Do you want to plot shear stress contour?')
iterate45=input('If YES, enter 1. Else, enter 0: ');
clc;

while iterate45==1

    % Decide to use either from experimental sigma_45 or r45 to find c6.
    disp('Please decide which data is used to find c6.');
    decide=input('Use experimental sigma_45, enter 1. Use experimental r45, enter 2: ');

    if decide==1
      Sat45=input('Enter experimental yield stress at 45 degrees to the rolling direction: ');
    else
      Rat45=input('Enter experimental r value at 45 degrees to the rolling direction:');
    end

    while decide>0

        % Equation obtained after given shear stress and transformation matrix p.
        c6='(2/(alphax+alphay+alphaz*2^m))^(1/m)*(sigma/X4)';


        % Substitute input data
        C6=subs(c6,M,'m');C6=subs(C6,XsA,'X4');C6=subs(C6,Eff,'sigma');

C6=subs(C6,AlphaX,'alphax');C6=subs(C6,AlphaY,'alphay');C6=subs(C6,AlphaZ,'alphaz
');


        % Numerize the equation to find c6.
        C6=numeric(C6);


        % Eigenvectors obtained when the sigma45 is assumed given.
        v=sym('[0,((c2-c1)+((c2-c1)^2+36*c6^2)^0.5)/(6*c6),1;0,1,((c2-c1)-((c2-
c1)^2+36*c6^2)^0.5)/(6*c6);1,0,0]');


        % Substitute c1, c2 and c6 from results above.
        v=subs(v,C1,'c1');v=subs(v,C2,'c2');v=subs(v,C6,'c6');
```

```
% Numerize eigenvector matrix v.
v=numeric(v);
u1=v(:,1);u2=v(:,2);u3=v(:,3);


% Use the Gram-Schmidt process to find the orthonormal basis.
u11=u1;
u22=u2-dot(u2,u11)/norm(u11)^2*u11;
u33=u3-dot(u3,u11)/norm(u11)^2*u11-dot(u3,u22)/norm(u22)^2*u22;
U1=u11/norm(u11);U2=u22/norm(u22);U3=u33/norm(u33);


% Tensor Transformation matrix P from material to principal reference frame.
P=[U1,U2,U3];


% Find alpha 1, alpha 2 and alpha 3 after transformation.
a1=AlphaX*P(1,1).^2+AlphaY*P(2,1).^2+AlphaZ*P(3,1).^2;
a2=AlphaX*P(1,2).^2+AlphaY*P(2,2).^2+AlphaZ*P(3,2).^2;
a3=AlphaX*P(1,3).^2+AlphaY*P(2,3).^2+AlphaZ*P(3,3).^2;


% Find sigma_45 (s45) theoretically.
S45=(2/(a1*abs(((C1-C2)^2+36*C6^2)^0.5/6)^M+a2*abs((3*(C1+C2)-((C1-
C2)^2+36*C6^2)^0.5)/12)^M+a3*abs((3*(C1+C2)+((C1-
C2)^2+36*C6^2)^0.5)/12)^M))^(1/M)*Eff;


% phi=a1*abs(s2-s3)^m+a2+abs(s3-s1)^m+a3*abs(s1-s2)^m
% Differentiate phi with respect to s1, s2 and s3 to find the eigenvalues.
EE1=a2*M*S45*((3*(C1+C2)-((C1-
C2)^2+36*C6^2)^0.5)/12)*abs(S45*((3*(C1+C2)-((C1-C2)^2+36*C6^2)^0.5)/12))^(M-
2)*(-1)+a3*M*S45*(-1*(3*(C1+C2)+((C1-
C2)^2+36*C6^2)^0.5)/12)*abs(S45*((3*(C1+C2)+((C1-C2)^2+36*C6^2)^0.5)/12))^(M-
2);
EE2=a1*M*S45*(((C1-C2)^2+36*C6^2)^0.5/6)*abs(S45*(((C1-
C2)^2+36*C6^2)^0.5/6))^(M-2)+a3*M*S45*(-1*(3*(C1+C2)+((C1-
C2)^2+36*C6^2)^0.5)/12)*abs(S45*((3*(C1+C2)+((C1-C2)^2+36*C6^2)^0.5)/12))^(M-
2)*(-1);
EE3=a1*M*S45*(((C1-C2)^2+36*C6^2)^0.5/6)*abs(S45*(((C1-
C2)^2+36*C6^2)^0.5/6))^(M-2)*(-1)+a2*M*S45*((3*(C1+C2)-((C1-
C2)^2+36*C6^2)^0.5)/12)*abs(S45*((3*(C1+C2)-((C1-C2)^2+36*C6^2)^0.5)/12))^(M-
2);
```

```
% Store differentiated equations into a matrix of eigenvalues, EE.
EE=[EE1,0,0;0,EE2,0;0,0,EE3];

% Transform the matrix EE to the material frame to find the matrix EPS.
EPS=P*EE*P';

% Store the EPS into a one-column matrix EPSILON.
EPSILON=[EPS(1,1);EPS(2,2);EPS(3,3);EPS(1,2)];

% Transform back to the original space using the linear operator L.
L=[(C2+C3)/3,-C3/3,-C2/3,0;-C3/3,(C3+C1)/3,-C1/3,0;-C2/3,-
C1/3,(C1+C2)/3,0;0,0,0,C6];
STRAIN=L*EPSILON;

% Use the tensor transformation for finding the strain at 45 degrees to R.D..
NSTRAIN11=STRAIN(1,1)/2+STRAIN(2,1)/2+STRAIN(4,1);
NSTRAIN22=STRAIN(1,1)/2+STRAIN(2,1)/2-STRAIN(4,1);

% Find the r45
R_45=(-NSTRAIN22)/(NSTRAIN11+NSTRAIN22);


  % Use Bisection Method to find the theoretical yield shear stress.
  % If experimental data of sigma_45 is larger than those of theoretical one,
  % increase theoretical yield shear stress and vice versa.
  % If experimental data of r45 is larger than those of theoretical one,
  % decrease theoretical yield shear stress and vice versa.

if decide==1
   if (Sat45-S45)>5e-5
     XsB=XsA;
  XsA=XsA+abs(XsC-XsA)/2;
   elseif (Sat45-S45)<-5e-5
     XsC=XsA;
  XsA=XsA-abs(XsA-XsB)/2;
 else


  % Store the theoretical yield stress Xshear.
     Xshear=XsA;
     decide=0;
 end
```

```
        elseif decide==2
            if (Rat45-R_45)<-5e-5
              XsB=XsA;
           XsA=XsA+abs(XsC-XsA)/2;
          elseif (Rat45-R_45)>5e-5
              XsC=XsA;
           XsA=XsA-abs(XsA-XsB)/2;
          else


            % Store the theoretical yield stress Xshear.
              Xshear=XsA;
            decide=0;
          end
        end
    end


    % Stop calculation for c6 from experimental normalised sigma_45 and r45.
    iterate45=0;
end
clc;



% Store data to display.
Stress=[X1,X2,X3];
Coeff=[C1,C2,C3];
Alpha=[AlphaX,AlphaY,AlphaZ];


% Display the final of the results after simulation.
disp('Summary of the results of Barlat 94 Yield Locus:')
disp('--------------------------------------------------------------------------------' )
disp('The yield stresses at rolling, transverse and normal directions are: ')
disp(Stress);
disp('The effective stress is: ')
disp(Eff);
disp('The exponient of the six-component yield criterion 94 is: ')
disp(M);
disp('The coefficients of c1, c2 and c3 are: ');
disp(Coeff);
disp('The coefficients of alpha_x, alpha_y and alpha_z are: ')
disp(Alpha);
```

```
disp('The theoretical shear yield stress is: ')
disp(Xshear);
disp('The coefficient of c6 is: ')
disp(C6);
disp('The theoretical sigma_45 is: ')
disp(S45);
disp('The theoretical r45 is: ')
disp(R_45);

% Save some data into a file named data.txt for plotting contour.
Data=[M,AlphaX,AlphaY,AlphaZ,C1,C2,C3,C6,Xshear,Eff]';
save data.txt Data -ascii -double;

% The End of Programme
```

Appendix D

A Program Written in MATLAB for Plotting the Contours of the Yield Loci, with the Presence of a Shear Stress Term

```
% Clear off all the data in memory.
clear all;

% Input data.
load data.mat -ascii;fid=fopen('data.mat');[R]=fscanf(fid,'%f',[1,10]);

% The order of results R is M, AlphaX, AlphaY, AlphaZ, C1, C2, C3, C6, Xshear and
Eff.
% See the programme of barlat94.m for details.
M=R(1);AlphaX=R(2);AlphaY=R(3);AlphaZ=R(4);C1=R(5);C2=R(6);C3=R(7);C6=R(8
);Xshear=R(9);Eff=R(10);

% The following part of the programme is to increment the shear stress contour.
% Display the normalized shear stress.
disp('The Normalized Shear Stress is:')
disp(Xshear/Eff);

% Input a lower normalized shear stress for plotting its corresponding contour.
ns=input('Enter a lower normalized shear stress for plotting its corresponding contour: ');

% Symbolic shrcon matrix represents the parametrized deviatoric stress tensor.
shrcon=sym('[(cos(t2)*(c3*(cos(t1)-
sin(t1))+c2*cos(t1)))/3,c6*sin(t2),0;c6*sin(t2),(cos(t2)*(c1*sin(t1)-c3*(cos(t1)-
sin(t1))))/3,0;0,0,(cos(t2)*(c2*cos(t1)+c1*sin(t1)))/(-3)]');

% Substitute the numeric coefficients C1, C2, C3 and C6 into Shrcon matrix.
Shrcon=subs(shrcon,C1,'c1');Shrcon=subs(Shrcon,C2,'c2');Shrcon=subs(Shrcon,C3,'c3');
Shrcon=subs(Shrcon,C6,'c6');

% Set empty matrice ContourX and ContourY.
% ContourX is the corresponding normalized yield stresses at rolling direction.
% ContourY is the corresponding normalized yield stresses at transverse direction.
ContourX=[];
ContourY=[];
```

```
% Project the yield shear stress contour.
% T1 is the angle in radian measured from the normalized yield stress at rolling direction.
% T2 is the angle in radian projected from the direction of the requested normalized shear
stress.
t1=45;
T1=t1*pi/180;
T2=pi/2;
T2A=0;
T2B=0;
T2C=0;

% Substitute the numeric angles T1 and T2 into the Contour matrix and numerize it.
contour=subs(Shrcon,T1,'t1');
Contour=subs(contour,T2,'t2');
Contour=numeric(Contour);

% Calculate and sort the eigenvalue matrix e and the eigenvector matrix v.
e=[Contour(3,3);.5*(Contour(1,1)+Contour(2,2)+sqrt((Contour(1,1)-
Contour(2,2))^2+4*Contour(1,2)^2));.5*(Contour(1,1)+Contour(2,2)-sqrt((Contour(1,1)-
Contour(2,2))^2+4*Contour(1,2)^2))];
v1=[0;0;1];
v2=[e(2)-Contour(2,2);Contour(1,2);0];
v3=[Contour(1,2);e(3)-Contour(2,2);0];
V=[v1,v2,v3];
u1=V(:,1);u2=V(:,2);u3=V(:,3);

% Use the Gram-Schmidt process to find the orthonormal basis.
u11=u1;
u22=u2-dot(u2,u11)/norm(u11)^2*u11;
u33=u3-dot(u3,u11)/norm(u11)^2*u11-dot(u3,u22)/norm(u22)^2*u22;
U1=u11/norm(u11);U2=u22/norm(u22);U3=u33/norm(u33);

% Tensor Transformation matrix P from material to principal reference frame.
P=[U1,U2,U3];

% Find alpha 1, alpha 2 and alpha 3 after transformation.
a1=AlphaX*P(1,1).^2+AlphaY*P(2,1).^2+AlphaZ*P(3,1).^2;
a2=AlphaX*P(1,2).^2+AlphaY*P(2,2).^2+AlphaZ*P(3,2).^2;
a3=AlphaX*P(1,3).^2+AlphaY*P(2,3).^2+AlphaZ*P(3,3).^2;

% Guess is the calculated normalized shear stress when t1=45 and t2=90.
Eq=a1*abs(e(2,1)-e(3,1))^M+a2*abs(e(3,1)-e(1,1))^M+a3*abs(e(1,1)-e(2,1))^M;
Guess=(2/Eq)^(1/M)*sin(T2);
DiffC=Guess-ns;
```

```
% Find the normalized yield stresses at rolling and transverse directions when T1 is from
Pi/4 to 5Pi/4.
if abs(DiffC)<=1e-5

 % No normalized yield stresses at rolling and tranverse direction at T2=Pi/2.
 ContourX=0;
 ContourY=0;
 halt=0;

else

 % Set T2A=pi for incrementation.
 T2A=T2/2;

 % From the shear stress ns, find the corresponding normalized yield stresses from 45 to
225 degrees.
 for t1=45:2:225
   T1=t1*pi/180;
   T2B=0;
   T2C=0;

   % Use the same formulation to calculate Guess
   contour=subs(Shrcon,T1,'t1');
   Contour=subs(contour,T2A,'t2');
   Contour=numeric(Contour);
   e=[Contour(3,3);.5*(Contour(1,1)+Contour(2,2)+sqrt((Contour(1,1)-
Contour(2,2))^2+4*Contour(1,2)^2));.5*(Contour(1,1)+Contour(2,2)-sqrt((Contour(1,1)-
Contour(2,2))^2+4*Contour(1,2)^2))];
   v1=[0;0;1];
   v2=[e(2)-Contour(2,2);Contour(1,2);0];
   v3=[e(3)-Contour(2,2);Contour(1,2);0];
   V=[v1,v2,v3];
   u1=V(:,1);u2=V(:,2);u3=V(:,3);
   u11=u1;
   u22=u2-dot(u2,u11)/norm(u11)^2*u11;
   u33=u3-dot(u3,u11)/norm(u11)^2*u11-dot(u3,u22)/norm(u22)^2*u22;
   U1=u11/norm(u11);U2=u22/norm(u22);U3=u33/norm(u33);
   P=[U1,U2,U3];
   a1=AlphaX*P(1,1).^2+AlphaY*P(2,1).^2+AlphaZ*P(3,1).^2;
   a2=AlphaX*P(1,2).^2+AlphaY*P(2,2).^2+AlphaZ*P(3,2).^2;
   a3=AlphaX*P(1,3).^2+AlphaY*P(2,3).^2+AlphaZ*P(3,3).^2;
   Eq=a1*abs(e(2,1)-e(3,1))^M+a2*abs(e(3,1)-e(1,1))^M+a3*abs(e(1,1)-e(2,1))^M;
   Guess=(2/Eq)^(1/M)*sin(T2A);
```

```
    DiffC=Guess-ns;
    halt=1;
    while halt==1;
       if abs(DiffC)<=1e-5
        ContourX(:,(t1-45)/2+1)=(2/Eq)^(1/M)*cos(T1)*cos(T2A);
        ContourY(:,(t1-45)/2+1)=(2/Eq)^(1/M)*sin(T1)*cos(T2A);
        halt=0;
       elseif DiffC>1e-5
        T2C=T2A;
          T2A=T2A-abs(T2A-T2B)/2;

          % Use the same formulation to find Guess.
        Contour=subs(contour,T2A,'t2');
        Contour=numeric(Contour);
        e=[Contour(3,3);.5*(Contour(1,1)+Contour(2,2)+sqrt((Contour(1,1)-
Contour(2,2))^2+4*Contour(1,2)^2));.5*(Contour(1,1)+Contour(2,2)-sqrt((Contour(1,1)-
Contour(2,2))^2+4*Contour(1,2)^2))];
        v1=[0;0;1];
          v2=[e(2)-Contour(2,2);Contour(1,2);0];
          v3=[e(3)-Contour(2,2);Contour(1,2);0];
          V=[v1,v2,v3];
          u1=V(:,1);u2=V(:,2);u3=V(:,3);
          u11=u1;
          u22=u2-dot(u2,u11)/norm(u11)^2*u11;
        u33=u3-dot(u3,u11)/norm(u11)^2*u11-dot(u3,u22)/norm(u22)^2*u22;
        U1=u11/norm(u11);U2=u22/norm(u22);U3=u33/norm(u33);
          P=[U1,U2,U3];
          a1=AlphaX*P(1,1).^2+AlphaY*P(2,1).^2+AlphaZ*P(3,1).^2;
          a2=AlphaX*P(1,2).^2+AlphaY*P(2,2).^2+AlphaZ*P(3,2).^2;
          a3=AlphaX*P(1,3).^2+AlphaY*P(2,3).^2+AlphaZ*P(3,3).^2;
          Eq=a1*abs(e(2,1)-e(3,1))^M+a2*abs(e(3,1)-e(1,1))^M+a3*abs(e(1,1)-
e(2,1))^M;
        Guess=(2/Eq)^(1/M)*sin(T2A);
        DiffC=Guess-ns;
        halt=1;
       elseif DiffC<1e-5
        T2B=T2A;
        T2A=T2A+abs(T2C-T2A)/2;

          % Use the same formulation to find Guess.
        Contour=subs(contour,T2A,'t2');
        Contour=numeric(Contour);
```

```
        e=[Contour(3,3);.5*(Contour(1,1)+Contour(2,2)+sqrt((Contour(1,1)-
Contour(2,2))^2+4*Contour(1,2)^2));.5*(Contour(1,1)+Contour(2,2)-sqrt((Contour(1,1)-
Contour(2,2))^2+4*Contour(1,2)^2))];
        v1=[0;0;1];
           v2=[e(2)-Contour(2,2);Contour(1,2);0];
           v3=[e(3)-Contour(2,2);Contour(1,2);0];
           V=[v1,v2,v3];
           u1=V(:,1);u2=V(:,2);u3=V(:,3);
           u11=u1;
           u22=u2-dot(u2,u11)/norm(u11)^2*u11;
        u33=u3-dot(u3,u11)/norm(u11)^2*u11-dot(u3,u22)/norm(u22)^2*u22;
        U1=u11/norm(u11);U2=u22/norm(u22);U3=u33/norm(u33);
           P=[U1,U2,U3];
           a1=AlphaX*P(1,1).^2+AlphaY*P(2,1).^2+AlphaZ*P(3,1).^2;
           a2=AlphaX*P(1,2).^2+AlphaY*P(2,2).^2+AlphaZ*P(3,2).^2;
           a3=AlphaX*P(1,3).^2+AlphaY*P(2,3).^2+AlphaZ*P(3,3).^2;
           Eq=a1*abs(e(2,1)-e(3,1))^M+a2*abs(e(3,1)-e(1,1))^M+a3*abs(e(1,1)-
e(2,1))^M;
        Guess=(2/Eq)^(1/M)*sin(T2A);
        DiffC=Guess-ns;
        halt=1;
       end
    end
  end
end

% Restore the yield shear stresses in all directions.
XContour=-1*ContourX;
YContour=-1*ContourY;
ContourX=[ContourX,XContour];
ContourY=[ContourY,YContour];
ContourXY=[ContourX;ContourY]';
% Plot the yield shear stress contour.
plot(ContourX,ContourY);
grid;
title('Barlat 94 Yield Locus With Contour Plot');
xlabel('Normalized Yield Stresses at Rolling Direction');
ylabel('Normalized Yield Stresses at Transverse Direction');
axis equal;
print -dbitmap scontour;
save contour.txt ContourXY -ascii -double;

% The End of Programme.
```

Appendix E

A Program Written in MATLAB for Plotting the Contours of the Yield Loci, without the Presence of a Shear Stress Term

```
% Clear off all the data in memory.
clear all;

% Input data.
load data.mat -ascii;fid=fopen('data.mat');[R]=fscanf(fid,'%f',[1,10]);

% The order of results R is M, AlphaX, AlphaY, AlphaZ, C1, C2, C3, C6, Xshear and
Eff.
% See the programme of barnew94.m for details.
M=R(1);AlphaX=R(2);AlphaY=R(3);AlphaZ=R(4);C1=R(5);C2=R(6);C3=R(7);C6=R(8
);Xshear=R(9);Eff=R(10);

% Symbolic shrcon matrix represents the parametrized deviatoric stress tensor.
shrcon=sym('[(c3*(cos(t1)-sin(t1))+c2*cos(t1))/3,0,0;0,(c1*sin(t1)-c3*(cos(t1)-
sin(t1)))/3,0;0,0,(c2*cos(t1)+c1*sin(t1))/(-3)]');

% Substitute the numeric coefficients C1, C2, C3 and C6 into Shrcon matrix.
Shrcon=subs(shrcon,C1,'c1');Shrcon=subs(Shrcon,C2,'c2');Shrcon=subs(Shrcon,C3,'c3');

% Set empty matrice ContourX and ContourY.
% ContourX is the corresponding normalized yield stresses at rolling direction.
% ContourY is the corresponding normalized yield stresses at transverse direction.
ContourX=[];
ContourY=[];

% Find the normalized yield stresses from 45 to 225 degrees.
for t1=45:2:225

  % T1 is the angle in radian measured from the normalized yield stress at rolling
direction.
  T1=t1*pi/180;
  % Numerize Contour and find eigenvalues of matrix s.
  Contour=subs(Shrcon,T1,'t1');
  Contour=numeric(Contour);
```

```
  e=[Contour(1,1);Contour(2,2);Contour(3,3)];

  % Eq is the yield criterion.
  Eq=AlphaX*abs(e(2,1)-e(3,1))^M+AlphaY*abs(e(3,1)-e(1,1))^M+AlphaZ*abs(e(1,1)-
e(2,1))^M;
  ContourX(:,(t1-45)/2+1)=(2/Eq)^(1/M)*cos(T1);
  ContourY(:,(t1-45)/2+1)=(2/Eq)^(1/M)*sin(T1);

end

% Restore the yield shear stresses in all directions.
XContour=-1*ContourX;
YContour=-1*ContourY;
ContourX=[ContourX,XContour];
ContourY=[ContourY,YContour];
ContourXY=[ContourX;ContourY]';

% Plot the yield shear stress contour.
plot(ContourX,ContourY);
grid;
title('Barlat 94 Yield Locus With Contour Plot');
xlabel('Normalized Yield Stresses at Rolling Direction');
ylabel('Normalized Yield Stresses at Transverse Direction');
axis equal;
print -dbitmap con2d;
save con2d.txt ContourXY -ascii -double;

% The End of Programme.
```

Appendix F

A Program Written in MATLAB for Evaluating the Yield Stress and r-value at Any Orientation to the Rolling Direction

```
% Clear off all the data in memory.
clear all;

% Input data.
name=input('Enter the drive, the directory and the filename for data input: ','s');
fid=fopen(name,'r');[R]=fscanf(fid,'%f',[1,10]);

% The order of results R is M, AlphaX, AlphaY, AlphaZ, C1, C2, C3, C6, Xshear and
Eff.
% See the programme of barlat94.m for details.
M=R(1);AlphaX=R(2);AlphaY=R(3);AlphaZ=R(4);C1=R(5);C2=R(6);C3=R(7);C6=R(8
);Xshear=R(9);Eff=R(10);

% Request the angles with respect to rolling direction.
clc;
disp('To plot the normalized stresses and r values, enter the angle range to R. D.');
disp('The angle range should be within 0 to 90 degrees.');
initial=input('Enter the start-up angle in degrees: ');
final=input('Enter the last angle in degrees: ');

% Empty matrices ns and r for storing all normalized stresses and r values.
ns=[];
r=[];

% Find the normalized stresses and r values within the angle range.
for i=initial:final
  t=i*pi/180;
  st=sin(t);
  ct=cos(t);
  s2t=sin(2*t);
  c2t=cos(2*t);
  st2=sin(t)^2;
  ct2=cos(t)^2;
```

```
% Find eigenvectors of s, where s=L*sigma
s=sym('[(c2*ct2+c3*c2t)/3,c6*st*ct,0;c6*st*ct,(c1*st2-c3*c2t)/3,0;0,0,-
1*(c1*st2+c2*ct2)/3]');
s=subs(s,C1,'c1');
s=subs(s,C2,'c2');
s=subs(s,C3,'c3');
s=subs(s,C6,'c6');
s=subs(s,st,'st');
s=subs(s,ct,'ct');
s=subs(s,st2,'st2');
s=subs(s,ct2,'ct2');
s=subs(s,s2t,'s2t');
s=subs(s,c2t,'c2t');
s=numeric(s);
[evector,evalue]=eig(s);
v=evector;
u1=v(:,1);u2=v(:,2);u3=v(:,3);

% Use the Gram-Schmidt process to find the orthonormal basis.
u11=u1;
u22=u2-dot(u2,u11)/norm(u11)^2*u11;
u33=u3-dot(u3,u11)/norm(u11)^2*u11-dot(u3,u22)/norm(u22)^2*u22;
U1=u11/norm(u11);U2=u22/norm(u22);U3=u33/norm(u33);

% Tensor Transformation matrix P from material to principal reference frame.
P=[U1,U2,U3];

% Find alpha 1, alpha 2 and alpha 3 after transformation.
a1=AlphaX*P(1,1).^2+AlphaY*P(2,1).^2+AlphaZ*P(3,1).^2;
a2=AlphaX*P(1,2).^2+AlphaY*P(2,2).^2+AlphaZ*P(3,2).^2;
a3=AlphaX*P(1,3).^2+AlphaY*P(2,3).^2+AlphaZ*P(3,3).^2;

% Calculate (s2-s3)/s(theta),(s3-s1)/s(theta) as s23, s31 etc.
s23=evalue(2,2)-evalue(3,3);
s31=evalue(3,3)-evalue(1,1);
s12=evalue(1,1)-evalue(2,2);

% Find s(theta),S, and normalized s(theta),NS, theoretically.
S=(2/(a1*abs(s23)^M+a2*abs(s31)^M+a3*abs(s12)^M))^(1/M)*Eff;
NS=(2/(a1*abs(s23)^M+a2*abs(s31)^M+a3*abs(s12)^M))^(1/M);

% phi=a1*|s2-s3|^m+a2*|s3-s1|^m+a3*|s1-s2|^m
% Differentiate phi with respect to s1, s2 and s3 to find the eigenvalues.
EE1=-1*a2*M*S*s31*abs(S*s31)^(M-2)+a3*M*S*s12*abs(S*s12)^(M-2);
```

```
  EE2=a1*M*S*s23*abs(S*s23)^(M-2)-a3*M*S*s12*abs(S*s12)^(M-2);
  EE3=-1*a1*M*S*s23*abs(S*s23)^(M-2)+a2*M*S*s31*abs(S*s31)^(M-2);


  % Store differentiated equations into a matrix of eigenvalues, EE.
  EE=[EE1,0,0;0,EE2,0;0,0,EE3];

  % Transform the matrix EE to the material frame to find the matrix EPS.
  EPS=P*EE*P';

  % Store the EPS into a one-column matrix EPSILON.
  EPSILON=[EPS(1,1);EPS(2,2);EPS(3,3);EPS(1,2)];

  % Transform back to the original space using the linear operator L.
  L=[(C2+C3)/3,-C3/3,-C2/3,0;-C3/3,(C3+C1)/3,-C1/3,0;-C2/3,-
C1/3,(C1+C2)/3,0;0,0,0,C6];
  STRAIN=L*EPSILON;

  % Use the tensor transformation for finding the strain at 45 degrees to R.D..
  NSTRAIN11=ct2*STRAIN(1,1)+st2*STRAIN(2,1)+2*st*ct*STRAIN(4,1);
  NSTRAIN22=st2*STRAIN(1,1)+ct2*STRAIN(2,1)-2*st*ct*STRAIN(4,1);

  % Find the r(theta)
  R=(-NSTRAIN22)/(NSTRAIN11+NSTRAIN22);

  % Store nst and rt for graph plot.
  ns(i-initial+1,:)=NS;
  r(i-initial+1,:)=R;
  theta(i-initial+1,:)=i;

end

% Plot normalized s(theta) or r(theta) to plot
clc;
disp('Do you want to plot Normalized Yield Stresses or R Values? ');
choose=input('Enter 1 for plotting or save data, Else for EXIT: ');
clc;

while choose==1
  disp('Select Normalized Yield Stresses or R Values to plot. ');
  select=input('Enter 0 for Stresses or Enter 1 for R or Else for Data Saving: ');

  if select==0
```

```
% Plot normalized s(theta).
plot(theta,ns);
grid;
title('Normalized Yield Stresses for Barlat 94 Yield Locus');
xlabel('Angles with respect to the Rolling Direction');
ylabel('Normalized Yield Stresses');
disp(' ');
disp('The figure will be saved as a file named nstress.bmp. ');
print –dbitmap nstress
disp(' ');
disp('Do you want to plot Normalized Yield Stresses or R Values? ');
choose=imput('Enter 1 for plotting or data-saving, or Other key for EXIT: ');
clc;

elseif select==1

% Plot r(theta)
plot(theta,r);
grid;
title('R Values for Barlat 94 Yield Locus')
xlabel('Angles with respect to the Rolling Direction');
ylabel('R values');
disp(' ');
disp('The figure will be saved as a file named rvalue.bmp. ');
print –dbitmap rvalue
disp(' ');
disp('Do you want to plot Normalized Yield Stresses or R Values? ');
choose==input('Enter 1 for plotting or data-saving, or Other key for EXIT: ');
clc;

else
disp(' ');
disp('Nothing else will be plotted. ');
disp('SAVE the data of Normalized Yield Stresses and R Values. ');
disp('Data will be saved in the file named rnsdata.txt. ');
disp('Column 1 is ANGLE. Column 2 is Normalized Stress. Column 3 is R Value');
disp(' ');

% Store ns and r with their corresponding theta.
Data=[theta,ns,r];

% Save data into a file named rnsdata.txt for plotting.
save rnsdata.txt Data -ascii -double;
choose=0;
```

```
    end
end

% The End of Programme
```

References

1. C. S. Barrett and T. B. Massalski. ***Structure of Metals.*** McGraw-Hill, New York, 1966.

2. G. I. Taylor. ***Plastic Strain in Metals.*** J. Inst. Metals, Vol. 62, pp. 307-324, 1938.

3. G. I. Taylor. ***Analysis of Plastic Strain in a Cubic Crystal.*** In Timoshenko Aniv. Vol., pp. 218-224, Macmillan, New York, 1938.

4. J. F. W. Bishop and R. Hill. ***A Theory of Plastic Distortion of a Polycrystalline Aggregate under Combined Stresses.*** Philos. Mag., Vol. 42, pp. 414-427, 1951.

5. J. F. W. Bishop and R. Hill. ***A Theoretical Derivation of the Plastic Properties of a Polycrystalline Face-centered Metal.*** Philos. Mag., Vol. 42, pp. 1298-1307, 1951.

6. W. F. Hosford and W. A. Backofen. ***Strength and Plasticity of Textured Metals.*** In Fundamentals of Deformation Processing, p. 259, Syracuse Univ. Press, 1964.

7. H. R. Piehler and W. A. Backofen. ***The Prediction of Anisotropic Yield Surfaces for Textured Sheet.*** In Textures in Research and Practice, (edited by J. Grewen and G. Wasserman), Springer, Vienna, p. 436, 1969.

8. W. A. Backofen. ***Deformation Processing.*** Addison-Wesley, Reading, Mass., 1972.

9. W. B. Hutchinson. ***Measurement and Interpretation of Texture in Metals.*** Transactions of Indian Institute of Metals, Vol. 34, pp. 355-363, 1981.

10. M. Hatherly and W. B. Hutchinson. ***An Introduction to Texture in Metals.*** The Institution of Metallurgists, London, 1979.

11. H. J. Bunge. ***Preferred Orientation Analysis in Textured Materials.*** Advances in X-ray Analysis, Vol. 35, pp. 263-275, 1992.

12. H. J. Bunge, R. Groβterlinden, A. Hasse, R. Ortega, J. A. Szpunar and P. Van Houtte. ***Advanced Experimental Techniques in X-ray Texture Analysis.*** Materials Science Forum, Vol. 157-162, pp. 71-96, 1994.

13. L. G. Schulz. ***A Direct Method for Determining Preferred Orientation of A Flat Reflection Sample Using A Geiger Counter X-ray Spectrometer***. J. Appl. Phys., Vol. 20, pp. 1033-1036, 1949.

14. H. J. Bunge. ***Advantages of Neutron Diffraction in Texture Analysis***. Textures and Microstructures, Vol. 10, pp. 265-307, 1989.

15. H. -G. Brokmeier. ***Texture Analysis by Neutron Diffraction***. Materials Science Forum, Vol. 157-162, pp. 59-70, 1994.

16. R. A. Schwarzer and H. Weiland, ***Measurement of Local Textures by Electron Diffraction: Comparison with X-ray Texture Analysis***. Proceedings of Eight International Conference on Textures of Materials (ICOTOM 8) (edited by J. S. Kallend and G. Gottstein), The Metallurgical Society, pp. 203-208, 1988.

17. R. A. Schwarzer. ***The Determination of Local Texture by Electron Diffraction - A Tutorial Review***. Textures and Microstructures, Vol. 20, pp.7-27, 1993.

18. A. Segmuller and G. Wassermann. ***Walztexturen von Molybdan und Tantal***. Freiberger Forschungshefte, Vol. B38, pp. 38-44, 1953.

19. R. J. Roe. ***Description of Crystallite Orientation in Polycrystalline Materials III: General Solution to Pole Figure Inversion***. J. Appl. Phys. Vol. 36, pp. 2024-2031, 1965.

20. H. J. Bunge. ***Zur darstellung allgemeinen Texturon***. Zeit Metallk, Vol. 52, p. 872, 1965.

21. H. -R Wenk, H. J. Bunge, J. S. Kallend, K. Lucke, S. Matties, J. Pospiech, P. Van Houtte. ***Orientation Distributions: Representation and Determination***. Proceedings of Eighth International Conference on Textures of Materials (ICOTOM 8) (edited by J. S. Kallend and G. Gottstein), The Metallurgical Society, pp. 17-30, 1988.

22. C. Esling, E. Bechler-Ferry and H. J. Bunge. ***Three-dimensional Texture Analysis after Bunge and Roe: Correspondence between the Respective Mathematical Techniques***. Textures and Microstructures, Vol. 5, pp. 95-125, 1982.

23. F. C. Frank. Proceedings of Eighth International Conference on Textures of Materials (ICOTOM 8) (edited by J. S. Kallend and G. Gottstein), The Metallurgical Society, 1988.

24. U. F. Kocks and C. N. Tome and H. -R. Wenk. ***Texture and Anisotropy: Preferred Orientations in Polycrystals and their Effect on Materials Properties***. Cambridge University Press, Cambridge, 1998.

25. G. J. Davies, D. J. Goodwill and J. D. Kallend. ***Charts for Analyzing Crystallite Distribution Function Plots for Cubic Materials***. J. Appl. Cryst., Vol. 4, p. 67, 1971.

26. H. J. Bunge. ***Three-dimensional Texture Analysis***. Inter. Mater. Rev., Vol. 32, pp. 265-291, 1987.

27. H. J. Bunge. ***Texture Analysis in Materials Science***. (translated by P. R. Morris), Butterworths, London, 1982.

28. H. J. Bunge and W. T. Roberts. ***Orientation Distribution and Plastic Anisotropy in Stabilized Sheet Steel***. J. Appl. Crystallogr. Vol. 2, p. 116, 1969.

29. J. S. Kallend and G. J. Davies. ***The Prediction of Plastic Anisotropy in Annealed Sheets of Copper and α-brass***. J. Inst. Metals, Vol. 98, p. 242, 1970.

30. J. S. Kallend and G. J. Davies. ***The Elastic and Plastic Anisotropy of Cold Rolled Sheets of Copper, Gilding Metal and α-brass***. J. Inst. Metals, Vol. 99, p. 257, 1971.

31. G. J. Davies, D. J. Goodwill, J. S. Kallend and T. Ruberg. ***The Correlation of Structure and Texture with Formability***. J. Inst. Metals, Vol. 101, p. 270, 1973.

32. C. S. da C. Viana, J. S. Kallend and G. J. Davies. ***The Use of Texture Data to Predict the Yield Locus of Metal Sheets***. Int. J. Mech. Sci., Vol. 21, p. 355, 1979.

33. R. Sowerby, C. S. da C. Viana and G. J. Davies. ***The Influence of Texture on the Mechanical Response of Commercial Purity Copper Sheets in Some Simple Forming Processes***. Mats. Sci. Engng., Vol. 46, pp.23-51, 1980.

34. P. Penning. ***Minimization of Shears for Pencil Glide in Body-centered Cubic Metals***. Met. Trans., Vol. 7A, pp. 1021-1026, 1976.

35. P. Parniere and C. Sauzay. ***Determination of the Yield Loci of BCC Metals Deformation by Non Crystallographic Slip (Pencil Glide)***. Mat. Sci. Eng., Vol. 22, pp. 271-280, 1976.

36. S. L. Semiatin, P. R. Morris and H. R. Piehler. ***Microplasticity Predictions of r-Values and Yield Loci of Low Carbon Steel Sheets Deforming by <111> Pencil Glide. Texture of Crystalline Solids***, Vol. 3, pp. 191-214, 1979.

37. P. van Houtte. ***Calculation of the Yield Locus of Textured Polycrystals Using the Taylor and the Relaxed Taylor Theory***. Textures and Microstructures, Vol. 7, pp. 29-72, 1987.

38. F. Barlat, R. C. Becker, Y. Hayashida, Y. Maeda, M. Yanagawa, K. Chung, J. C. Brem, D. J. Lege, K. Matsui, S. J. Murtha and S. Hattori. ***Yielding Description for Solution Strengthened Aluminum Alloys***. Int. J. of Plasticity, Vol. 13.4, pp. 385-401, 1997.

39. J. S. Kallend and G. J. Davies. ***A Simulation of Texture Development in f.c.c. Metals***. Philos. Mag., Vol. 25, pp. 471-490, 1972.

40. P. van Houtte. ***Simulation of the Rolling and Shear Texture of Brass by the Taylor Theory Adapted for Mechanical Twinning***. Acta Metallurgica, Vol. 26, pp. 591-604, 1978.

41. S. Matties. ***On the Reproducibility of the Orientation Distribution Function of Texture Samples from Pole Figures (Ghost Phenomena)***. Phys. Status Solidi B, Vol. 92, pp.135-138

42. H. Schaeben and H. -R. Wenk. ***Vector Method***. In Preferred Orientation in Deformed Metals and Rocks: An Introduction to Modern Texture Analysis (edited by H. -R Wenk), pp. 123-137, Academic Press Inc., London, 1985.

43. J. Muller, C. Esling and H. J. Bunge. ***An Inversion Formula Expressing the Texture Function in terms of Angular Distribution Functions***. J. Phys., Vol. 42, pp. 161-165, 1981.

44. S. Matties and G. W. Vinel. ***On the Reproduction of the Orientation Distribution Function of Texturized Samples from Reduced Pole Figures Using the Conception of a Conditional Ghost Correction***. Phys. Status Solidi B, Vol. 112, pp. 111-120, 1982.

45. R. Hill. ***A Theory of Yielding and Plastic Flow of Anisotropic Metals***. Proc. Roy. Soc., Vol. 193A, pp. 281-297, 1948.

46. R. Hill. ***The Mathematical Theory of Plasticity***. New York, Oxford, 1950.

47. Frederic Barlat and Kwansoo Chung. ***Anisotropic Potentials for Plastically Deforming Metals***. Modelling Simulation in Mater. Sci. Eng., Vol. 1, pp. 403-416, 1993.

48. F. Barlat, Y. Maeda, K. Chung, M. Yanagawa, J. C. Brem, Y. Hayashida, D. J. Lege, K. Matsui, S. J. Murtha, S. Hattori, R. C. Becker, S. Makosey. ***Yield Function Development for Aluminum Alloy Sheets***. Aluminum Company of America, Alcoa Technical Center. Report 97-481-003, 1997.

49. A. P. Karafillis and M. C. Boyce. ***A General Anisotropic Yield Criterion Using Bounds and a Transformation Weighting Tensor***. J. Mech. Phys. Solids, Vol. 41, pp. 1859-1886, 1993.

50. W. F. Hosford. ***On Yield Loci of Anisotropic Cubic Metals***. 7th North Amer. Metalworking Conference. SME, Dearborn MI, pp. 191-197, 1979.

51. R. Logan and W. F. Hosford. ***Upper-bound Anisotropic Yield Locus Calculations Assuming <111>-Pencil Glide***. Int. J. Mech. Sci., Vol. 22, pp. 419-430, 1980.

52. Christian Vial, William F. Hosford and Robert M. Caddell. ***Yield Loci of Anisotropic Sheet Metals***. Int. J. Mech. Sci., Vol. 25, pp. 889-915, 1983.

53. Stephen W. Tsai and Edward M. Wu. ***A General Theory of Strength for Anisotropic Materials***. J. Composite Materials, Vol. 5, pp. 58-80, 1971.

54. S. E. Jones and P. P. Gillis. ***A Generalized Quadratic Flow Law for Steel Metals***. Metallurgical Transactions A, Vol. 15A, pp. 129-132, 1984.

55. M. Gotoh. ***A Theory of Plastic Anisotropy Based on Yield Function of Fourth Order (Plane Stress State) - I***. Int. J. Mech. Sci., Vol. 19, pp. 505-512, 1977.

56. M. Gotoh. ***A Theory of Plastic Anisotropy Based on Yield Function of Fourth Order (Plane Stress State) - II***. Int. J. Mech. Sci., Vol. 19, pp. 513-520, 1977.

57. F. Barlat and J. Lian. ***Plastic Behaviour and Stretchability of Sheet Metals. Part I: A Yield Function for Orthotropic Sheets under Plane Stress Conditions***. Int. J. of Plasticity, Vol. 5, pp. 512-566, 1989.

58. Frederic Barlat, Daniel J. Lege and John C. Brem. ***A Six-component Yield Function for Anisotropic Materials***. Int. J. of Plasticity, Vol.7, pp. 693-712, 1991.

59. Weixian Zhou. ***A New Non-quadratic Orthotropic Yield Criterion***. Int. J. Mech. Sci. Vol. 32, pp. 513-520, 1990.

60. Weixian Zhou. ***New Non-quadratic Orthotropic Yield Function for Triaxial Stress State***. Transactions of NFsoc., Vol. 2, pp. 62-67, 1992.

61. F. Montheillet, J. J. Jonas and M. Benferrah. ***Development of Anisotropy during the Cold Rolling of Aluminium Sheet***. Int. J. Mech. Sci., Vol. 33, pp. 197-209, 1991.

62. R. Hill. ***Theoretical Plasticity of Textured Aggregates***. Math. Proc. Camb. Phil. Soc., Vol. 85, pp. 179-191, 1979.

63. R. Hill. ***Constitutive Modelling of Orthotropic Plasticity in Sheet Metals***. Mech. Phys. Solids, Vol. 38, pp. 405-417, 1990.

64. S. B. Lin and J. L. Ding. ***A Modified Form of Hill's Orientation-dependence Yield Criterion for Orthotropic Sheet Metals***. J. Mech. Phys. Solids, Vol. 40, pp. 1739-1764, 1996.

65. R. Hill. ***A User-friendly Theory of Orthotropic Plasticity in Sheet Metals***. Int. J. Mech. Sci., Vol. 35, pp 19-25, 1993.

66. F. Barlat. ***Crystallographic Texture, Anisotropic Yield Surfaces and Forming Limits of Sheet Metals***. Mater. Sci. and Eng., Vol. 91, pp. 55-72, 1987.

67. W. F. Hosford. ***Limitations Non-quadratic Anisotropic Yield Criteria and Their Use in Analyses of Sheet Forming***. Proc. 15th IDDRG Congr. A.S.M, Dearborn, Michigan, U.S.A., pp. 163-170, 1988.

68. William F. Hosford. ***The Mechanics of Crystals and Textured Polycrystals***. Oxford, New York, 1993.

69. Robert H. Wagoner and Jean-Loup Chenot. ***Fundamentals of Metal Forming***. John Wiley and Sons, Inc., New York, 1997.

70. D. Green. ***Etude Expermentale et Numerique du Comportement Biaxial des Tôles Minces***. Ph.D. dissertation thesis, Universite de Sherbrooke, Canada, 1996.

71. John Woodthorpe and Roger Pearce. ***The Anomalous Behaviour of Aluminium Sheet under Balanced Biaxial Tension***. Int. J. Mech. Sci., Vol. 12, pp. 341-347, 1970.

72. A. Parmar and P. B. Mellor. ***Predictions of Limit Strains in Sheet Metal using A More General Yield Criterion***. Int. J. Mech. Sci., Vol. 20, pp. 385-391, 1978.

73. W. F. Hosford. ***Comments on Anisotropic Yield Criteria***. Int. J. Mech. Sci., Vol. 27, pp. 423-427, 1985.

74. K. Naruse, B. Dodd and Y. Motoki. ***Evaluation of Yield Criteria for Planar Anisotropy in Sheet Metals Using Experimental Results***. Advances in Engineering Plasticity and its Application, pp. 235-242, 1993.

75. J. Scordato. **The Student Edition of MATLAB: Version 4 User's Guide**. Prentice-Hall, New Jersey, 1995.

76. Melvin J, Maron. ***Numerical Analysis: A Practical Approach.*** Macmillan, New York, 1982.

77. Y. W. Chang and R. J. Asaro. ***An Experimental Study of Shear Localization in Aluminum-Copper Single Crystals***, Acta Metall., Vol.29, pp. 241-257, 1981.

78. J. Gil-Sevillano, P. van-Houtte and E. Aernoudt. Progress in Material Science, Vol. 25, pp. 69-412, 1980.

79. H. C. Rogers, Ann. Rev. Mat. Sci., Vol. 9, pp. 283-311, 1979.

80. S. P. Timothy, Acta Metall., Vol. 35, p. 301, 1987.

81. R. Dormeval. ***Adiabatic Shear Phenomena.*** Impact Loading and Dynamic Behaviour of Materials. DGM Informationsgesellschaft, Oberusel, Germany, pp. 43-56, 1988.

82. S. Matties, H. -R. Wenk and G. W. Vinel. ***Some Basic Concepts of Texture Analysis and Comparison of Three Methods to Calculate Orientation Distributions from Pole Figures.*** J. Appl. Cryst., Vol. 21, pp. 285-304. 1988.

83. R. Sowerby and W. Johnson. ***A Review of Texture and Anisotropy in Relation to Metal Forming***. Materials Science and Engineering, Vol. 20, pp. 101-111, 1975.

84. D. Rabbe. ***Computational Materials Science: the Simulation of Materials Microstructures and Properties***. Wiley-VCH, Weinheim, 1998.

85. H. J. Bunge. ***Fifty Years Textures in Research and Practice.*** Textures and Microstructures, Vol. 8 & 9, pp. 55-75, 1988.

86. H. –R Wenk, H. J. Bunge, J. S. Kallend, K. Lucke, S. Matties, J. Pospiech, P. Van Houtte. ***Orientation Distribution: Representation and Determination.*** Proceedings of Eighth International Conference on Textures of Materials (ICOTOM 8) (edited by J. S. Kallend and G. Gottstein), The Metallurgical Society, pp. 17-30, 1988.

87. M. Dahms and H. J. Bunge, ***The Iterative Series-Expansion Method for Quantitative Texture Analysis I: General Outline.*** J. Appl. Cryst., Vol. 22, pp. 437-447, 1989.

88. A. M. Maniatty, J. –S. Yu and T. Keane. ***Anisotropic Yield Criterion for Polycrystalline Metals Using Texture and Crystal Symmetries.*** International Journal of Solids and Structures, Vol. 36. pp. 5331-5355, 1999.

89. Y. T. Keum and K. B. Lee. ***Sectional Finite Element Analysis of Forming Processes for Aluminum-alloy Sheet Metals.*** International Journal of Mechanical Sciences, Vol. 42, pp. 1911-1933, 2000.

90. K. –C. Liao, P. A. Friedman, J. Pan and S. C. Tang. ***Texture Development and Plastic Anisotropy of B.C.C. Strain Hardening Sheet Metals.*** Int. J. Solids Structures, Vol. 35, pp.5205-5236, 1998.

91. Y. Maeda, M. Yanagawa, F. Barlat, K. Chung, Y. Hayashida, S. Hatton, K. Matsui, J. C. Brem, D. J. Lege, S. J. Murtha and T. Ishikawa. ***Experimental Analysis of Aluminum Yield Surface for Binary Al-Mg Alloy Sheet Samples.*** International Journal of Plasticity, Vol. 14, pp. 301-318, 1998.

92. K. Inal, P. D. Wu and K. W. Neale. ***Simulation of Earing in Textured Aluminum Sheets.*** International Journal of Plasticity, Vol. 16, pp. 635-648, 2000.

93. J. W. Yoon, D. Y. Yang, K. Chung and F. Barlat. ***A General Elasto-plastic Finite Element Formulation Based on Incremental Deformation Theory for Planar Anisotropy and Its Application to Sheet Metal Forming.*** International Journal of Plasticity, Vol. 15, pp. 35-67, 1999.

94. J. W. Yoon, F. Barlat, K. Chung, F. Pourboghrat and D. Y. Yang. ***Earing Predictions Based on Asymmetric Nonquadratic Yield Function.*** International of Journal of Plasticity, Vol. 16, pp. 1075-1104, 2000.

95. Jong-Bong Kim, Dong-Yol Yang, Jeong-Whan Yoon and F. Barlat. ***The Effect of Plastic Anisotropy on Compressive Instability in Sheet Metal Forming.*** International Journal of Plasticity, Vol. 16, pp. 649-676, 2000.

96. Shi-Hoon Choi, Jae-Hyung Cho, Kyu Hwan Oh, Kwansoo Chung and Frederic Barlat. ***Texture Evolution of FCC Sheet Metals During Deep Drawing Process.*** International Journal of Mechanical Sciences, Vol. 42, pp. 1571-1592, 2000.

97. P. Hu, Y. Q. Liu and J. C. Wang. ***Numerical Study of the Flange Earing of Deep Drawing Sheets with Stronger Anisotropy.*** International Journal of Mechanical Sciences, Vol. 43, pp. 279-296, 2001.

98. Siguang Xu and Klaus J. Weinmann. ***Prediction of Forming Limit Curves of Sheet Metals Using Hill's 1993 User-friendly Yield Criterion of Anisotropic Materials.*** Int. J. Mech. Sci. Vol. 40, pp. 913-925, 1998.

99. Jiao Cao, Hong Yao, Apostolos Karafillis and Mary C. Boyce. ***Prediction of Localized Thinning in Sheet Metal Using A General Anisotropic Yield Criterion.*** International Journal of Plasticity, Vol. 16, pp. 1105-1129, 2000.

100. Mitsutoshi Kuroda and Viggo Tverggard. ***Forming Limit Diagrams for Anisotropic Metal Sheets with Different Yield Criteria.*** International Journal of Solids and Structures, Vol. 37, pp. 5037-5059, 2000.

101. A. Graf and W. F. Hosford. ***The Influence of Strain Path Changes on Forming Limit Diagrams of Al 6111-T4.*** Int. J. Mech. Sci., Vol. 36, pp. 897-910, 1994.

102. H. J. Lau. ***A Numerical and Experimental Investigation of the Deep Drawing of Square Cups.*** Master Degree Dissertation Thesis, McMaster University, 1996.

103. W. A. Sisson. Metals and Alloys, Vol. 4, p. 193, 1933.

104. Ken Shaw. ***The Development of Texture at Intermediate Stages of Cold Rolling in Low Carbon BCC Steel.*** Master Degree Dissertation Thesis, McMaster University, 1999.

105. Hyung-Joon Shin, Joong-Kyu An and Dong Nyung Lee. ***The Influence of Tension on the Development of Rolling Textures.*** Mater. Sci. Re. Int., Vol. 6, pp. 161-166, 2000.